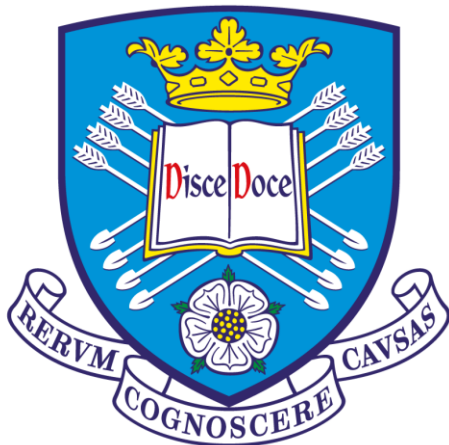


**Development of novel nanocomposite PVD
coatings to improve wear and corrosion
resistance of magnesium alloys**

by:

Lian Liu

*A dissertation submitted in fulfilment of the requirements for the
degree of*
Doctor of Philosophy



**The
University
Of
Sheffield.**

Department of Materials Science and Engineering

March 2017

Abstract

The main aim of this research was to develop novel nanocomposite PVD coatings for magnesium alloys, to improve their wear and corrosion resistance – and thereby explore the potential to extend the use of such alloys to moving parts for light-weighting of tribological components, where the potential for cumulative weight savings is immense if key parts can be made from magnesium, but the alloys cannot currently be used successfully due to their poor wear and corrosion behaviour under dynamic loading. The work comprises two main stages. The first stage was to produce a base layer for subsequent PVD ceramic nitride (or nitrogen-doped hard metallic) coating deposition. The second stage was to deposit a nanocomposite coating with improved tribological performance, by introducing sequentially nitrogen reactive gas, subsequent to the base layer preparation step.

In the first stage, sixteen AlCuMoMgZrB PVD coating layers were prepared by pulsed direct current closed-field unbalanced magnetron sputtering. Four deposition runs were carried out, with substrate negative bias voltages of 50 V, 60 V, 75 V and 100 V being applied. For each deposition run, four proprietary WE43 magnesium alloy substrates were placed at different positions (P1-P4) on the substrate holder, between AlMgB and ZrMoCu composite sputter targets mounted at 90° to each other. Investigations into composition, microstructure, mechanical and electrochemical properties were then carried out, to select the most suitable base layer. The P1-60 layer (*i.e.* deposited at P1 position, closest to the AlMgB composite target, with substrate negative bias of 60 V) was chosen as the most suitable candidate amongst the sixteen AlCuMoMgZrB coating

layers due to its superior mechanical properties, electrochemical properties, and amorphous microstructure.

In the second stage, four novel AlCuMoMgZrB(N) nanocomposite PVD coatings with different nitrogen reactive gas flow rates (*i.e.* 5 sccm, 10 sccm, 15 sccm and 20 sccm), introduced partway through the sputter deposition process, were produced sequentially, on top of the selected P1-60 base layer. Further detailed investigations into composition, microstructure, mechanical, tribological and electrochemical properties were performed to evaluate the improved wear and corrosion resistance.

For practical applications, P1-60-15sccm (46.27 at.% Al, 8.71 at.% Mg, 5.35 at.% Cu, 3.63 at.% Mo, 1.30 at.% Zr, 2.65 at.% B and 32.08 at.% N) seems a likely candidate to provide an optimal combination of wear and corrosion resistance – in terms of the best and the second-best performance in micro-abrasion and in corrosion tests, respectively.

Acknowledgements

Firstly, I would like to express my great gratitude to my supervisors, Dr. Adrian Leyland, Prof. Allan Matthews. They have provided me a great opportunity to undertake this research, and offered their guidance, support, encouragement, patience, immense knowledge and experience.

I would also like to express my great appreciation to Prof. Bradley Wynne and Dr Martin Jackson for their progress examine work. They have offered me generous and insightful advice.

My grateful thanks also go to the experimental officers from Sorby Centre. They are Dr. Peter Korgul, Dr. Le Ma, Dr, Peng Zeng, and Dr. Cheryl Shaw. Their sincere help have given me a strong support and made my research better.

Also, great thanks to my Friends (Xingguang Liu, Chang Liu, Yonghao Gao, Wei-Yu Chen, Ming Sun, Xiao Tao, Wing Kiu Yeung, Chen-Jui Liang, Josephine Lawal, Fahima Indeir, Husein D Meshreghi, Chanon Iamvasant, John Kavanagh, Zhe Cui, Junheng Gao, Dikai Guan, Xin Pan, Peng Gong *etc.*). We have had an unforgettable friendship in Sheffield.

Finally, special appreciation to my beloved parents (Wei Liu and Lixia Wang) and wife (Min Li). I would not have completed the PhD study without their grateful support.

Table of Contents

Abstract	i
Acknowledgements.....	iii
Table of Contents	iv
CHAPTER 1: INTRODUCTION.....	1
1.1. Background	1
1.2. Research purpose	3
CHAPTER 2: INTRODUCTION TO MAGNESIUM ALLOYS	4
2.1. Background	4
2.2. Advantages of Magnesium Alloys	6
2.3. Limitations of Magnesium Alloys.....	10
2.4. Protective Coatings for Magnesium Alloys	14
2.4.1. Conversion coatings	15
2.4.2. Anodising.....	16
2.4.3. Painting	17
2.4.4. Electrochemical plating	18
2.4.5. Vapour-phase deposition.....	19
CHAPTER 3: PVD COATINGS FOR MAGNESIUM ALLOYS	23
3.1. Advanced plasma assisted physical vapour deposition processes	23
3.1.1. Plasma Assisted Electron Beam Evaporative PVD.....	24
3.1.2. Electromagnetically Steered Cathodic Arc Evaporation.....	26
3.1.3. Closed-Field Unbalanced-Magnetron Sputtering	28
3.2. Selection of an appropriate PVD coating for magnesium alloys	32
3.3. Design concepts of nanocomposite PVD coatings	33
CHAPTER 4: EXPERIMENTAL PROCEDURE.....	37
4.1. Substrate Preparation	37
4.1.1. WE43 magnesium alloy selection.....	37
4.1.2. Grinding and polishing	38
4.2. Coating deposition	39
4.2.1. Sample Designation.....	40
4.2.2. Deposition equipment	42
4.2.3. Target combination.....	43

4.2.4.	Deposition configuration	44
4.2.5.	Deposition procedure	45
4.3.	Coating Analysis	47
4.3.1.	X-ray diffraction analysis.....	47
4.3.2.	Scanning electron microscopy observation.....	47
4.3.3.	Energy dispersive x-ray analysis	49
4.3.4.	Transmission electron microscopy analysis.....	50
4.3.5.	Nanoindentation	50
4.3.6.	Scratch-adhesion testing.....	51
4.3.7.	Micro-abrasion wear testing	52
4.3.7.1.	Two-body and three-body abrasions.....	52
4.3.7.2.	Test conditions of three-body abrasion	54
4.3.7.3.	Calculation of specific wear rates.....	55
4.3.8.	Electrochemical corrosion evaluation	56
CHAPTER 5: COMPOSITION AND MICROSTRUCTURE OF NOVEL NANOCRYSTALLINE/GLASSY ALCUMOMGZRB PVD COATINGS		58
5.1.	Elemental composition	60
5.1.1.	Effect of increasing substrate negative bias on elemental composition.....	62
5.1.2.	Discussion of influence of substrate negative bias on elemental composition .	64
5.1.2.1.	Resputtering effect	64
5.1.2.2.	Sputter yield	65
5.2.	Phase composition	67
5.2.1.	Discussion of the formation of nanocrystalline phases	68
5.2.1.1.	Intermetallic characteristic peaks	68
5.2.1.2.	Mg characteristic peak	69
5.2.2.	Discussion of the formation of amorphous phase.....	69
5.2.2.1.	Atomic collision cascade model	70
5.2.2.2.	Compositional difference	70
5.2.2.3.	Elemental selection.....	71
5.3.	Thickness and morphology	74
5.3.1.	Fracture cross-sections.....	74
5.3.2.	Layer thickness	77
5.3.3.	Surface morphology	79

5.3.4.	Discussion of the ion energy distribution during deposition.....	82
5.3.4.1.	L/ λ ratio	82
5.3.4.2.	Ionised argon gas.....	84
5.3.4.3.	Ionised metal species.....	85
5.3.4.4.	Limitations of the investigation of ion energy spectra.....	90
5.4.	Summary	91
CHAPTER 6: MECHANICAL AND ELECTROCHEMICAL PROPERTIES OF NOVEL NANOCRYSTALLINE/GLASSY ALCUMOMGZRB PVD COATINGS		93
6.1.	Mechanical properties	94
6.1.1.	Evaluation of H and E.....	94
6.1.2.	H/E ratio.....	97
6.2.	Adhesive strength.....	99
6.2.1.	Adhesive strengths of sixteen AlCuMoMgZrB layers	101
6.2.2.	Comparison of adhesion between P1-60 and P4-60 layers	103
6.3.	Electrochemical corrosion properties	107
6.3.1.	Open circuit potential evaluation and electrochemical impedance spectroscopy 107	
6.3.2.	Potentiodynamic polarisation.....	113
6.4.	Microstructural investigation of P1-60 base layer.....	116
6.5.	Summary	117
CHAPTER 7: INVESTIGATION OF NOVEL NITROGEN-CONTAINING ALCUMOMGZRB(N) PVD COATINGS		119
7.1.	Elemental composition	121
7.2.	Phase composition	124
7.2.1.	Formation of characteristic peaks.....	125
7.2.2.	Confirmation of nanocomposite microstructure	126
7.3.	Thickness and morphology	128
7.3.1.	Fracture cross-sections.....	128
7.3.2.	Surface morphology	130
7.4.	Mechanical properties	133
7.5.	Abrasive wear behaviour.....	135
7.6.	Electrochemical corrosion properties	138
7.6.1.	Open circuit potential evaluation and electrochemical impedance spectroscopy 138	

7.6.2.	Potentiodynamic polarisation scans	143
7.7.	Summary	145
CHAPTER 8: SUMMARY, CONCLUSION AND RECOMMENDATIONS FOR FUTURE WORK		148
8.1.	Summary and conclusion	148
	Stage 1: development of nanocrystalline/glassy base layer	149
	Stage 2: development of nanocomposite coating	152
8.2.	Recommendations for future work.....	155
CHAPTER 9: REFERENCES.....		161

CHAPTER 1: INTRODUCTION

1.1. Background

Magnesium is an attractive engineering metal, due primarily to its low density, relative abundance in the earth's crust and easy recyclability. With careful alloying and heat treatment, a moderately high strength-to-weight ratio can be achieved for magnesium alloys. Low-density magnesium components are promising to replace commonly-used materials (*e.g.* steels and aluminium alloys) in applications where the weight reduction is important. However, poor wear and corrosion resistance precludes the more widespread use of magnesium alloys, constraining their use remaining to technical challenges of mostly static, structural applications, rather than tribological components and assemblies, where the cumulative benefits of light-weighting could be more extensively realised.

Depositing a protective coating onto the surface of magnesium alloys is an obvious strategy to enhance their wear and corrosion performance. Among various surface treatments applied to magnesium alloys [1], is the plasma assisted physical vapour deposition (PAPVD) technique, which has been fairly extensively studied – and is now used widely in industry, to enhance the productivity and lifetime of many industrial tools and components [2]. The technique has progressively received attention as a flexible means of developing protective coatings for Magnesium alloys [3-9]. Many studies focus on using pure aluminium film as the interfacial layer (since its galvanic compatibility with magnesium, although not ideal, is better than for most other engineering metals). Moreover, a common theme running through such studies is the development of brittle Al-Mg intermetallic

compounds at the coating/substrate interface, either during, or after, coating – which tend to compromise the mechanical and load-bearing capacity (and may also have an adverse effect on corrosion behaviour. In this regard, multi-element PVD amorphous or ‘nanocomposite’ metal-based coatings may hold significant promise in avoiding such problems. Leyland and Matthews [10] have previously pointed out the relevance of using the ratio of hardness to elastic modulus (H/E) as an indicator of coating mechanical durability. and introduced the concept of metallic nanocomposite coatings [11]. Although the coatings with metallic nanocomposite structure do not exhibit extreme hardness, they may offer superior protection by providing enhanced resilience and/or ‘engineering toughness’ (*i.e.* an improved ability to accommodate both elastic and plastic strains under mechanical or tribological loading). Otherwise, a moderate proportion of ceramic constituents existing in the nanograined and/or glassy microstructure may also be acceptable (*i.e.* nanocrystalline-ceramic/amorphous-metal nanocomposite coating). This is because the ceramic phase constituents are beneficial in increasing hardness and – if sufficiently small and uniformly-distributed – may not significantly degrade the corrosion behaviour. If the glassy matrix can act to retain sufficiently low elastic modulus, the mechanical and tribological performance of this type of nanocomposite coating could be acceptable. In conclusion, developing novel PVD nanocomposite metal coatings for magnesium alloy substrates, to improve wear and corrosion resistance, is a worthwhile topic to investigate.

1.2. Research purpose

The aim of this research was to develop novel nanocomposite PVD coatings for zinc-free WE43 magnesium alloys, to improve their wear and corrosion resistance. The research comprises two stages. The first stage was to produce a base layer for ‘coupling’ of subsequent PVD hard ceramic nitride (or nitrogen-doped hard metallic) coatings to the (soft, elastically compliant) Mg-alloy substrate. The second stage was to deposit a hard, wear-resistant nanocomposite coating onto an ‘optimised’ base (coupling) layer, by introducing nitrogen reactive gas to the base layer deposition process. The two main objectives to achieve the aim described above were thus:

- i. Produce a moderately hard (and galvanically compatible), but compliant, base layer by PVD multi-element metallic coating deposition. This layer should possess good adhesive strength, mechanical and electrochemical corrosion properties, to support the subsequent tribological hard coating. Moreover, it is better to possess amorphous microstructure to readily achieve metallic (or ceramic) nanocomposite structure when the nitrogen gas is introduced in subsequent deposition.
- ii. To sequentially deposit a nanocomposite PVD coating onto the base layer *via* the introduction of nitrogen reactive gas to the magnetron sputter deposition process. This coating, with the desired mechanical property and microstructure, was expected to improve wear and corrosion resistance for the underlying magnesium alloy substrate.

CHAPTER 2: INTRODUCTION TO MAGNESIUM ALLOYS

2.1. Background

As the average temperature on earth continues to rise since 1880, global warming becomes one of the greatest challenges facing the world. The past year 2015 was recorded 0.9 °C above the 20th century average of 13.9 °C. This was the highest value in the 1880-2015 record, beating the previous record warmth of 2014 by 0.16 °C [12]. Global warming potentially leads to serious effects that include changing rainfall and snow patterns, increasing droughts and severe storms, reducing lake ice cover, melting glaciers, increasing sea levels, and changing plant and animal behaviour. Many attempts have been made to prevent dangerous anthropogenic interference with the climate system, in terms of reducing the emission of greenhouse gases. One of the most famous achievements was the establishment of the “Kyoto Protocol”, which was adopted in December 1997 by 55 nations at the United Nations Framework Convention on Climate Change (UNFCCC) and became legally binding on its 128 parties in February 2005 [13].

In order to abide by the legislative requirements from such global initiatives, many automotive manufacturing companies have concentrated on developing more environmentally friendly vehicles in an attempt to reduce exhaust emissions in which CO₂ is a major constituent that contributes to societal issues global warming and poor air quality [14]. As the amount of exhaust gases emitted is directly proportional to the fuel consumption, vehicle weight has become the most critical criterion in the

design of energy-saving mechanisms for transport [15]. A weight reduction of 100 kilograms represents a fuel saving of about 0.5 litres per 100km for a midsize vehicle (typically with a weight of 1600kg) [16]. Apart from the automotive industry, the efforts of achieving the energy-saving targets invariably promotes weight reduction in a myriad of other mobile equipment and products such as aeroplanes, space vehicles and various tools and fixtures that need to be transported from site to site.

Almost every attempt to reduce weight propels the extensive use of lighter materials, but without excessive sacrifice of mechanical properties (*i.e.* increased strength-to-weight ratio is key, from a mechanical design perspective). For instance, the design criteria of components in transportation industries normally concentrate on density, strength, stiffness and wear and corrosion resistance. Low density decreases fuel costs and allows larger payloads. High strength and stiffness ensure adequate performance and safety characteristics, while sufficient wear and corrosion resistance is beneficial to enhance the lifetime of engineering components. Among different lightweight materials, the use of magnesium alloys is developing rapidly due to a set of highly attractive properties [17].

2.2. Advantages of Magnesium Alloys

Although aluminium and its alloys are already being used as candidate materials to decrease product weight, significant additional reductions could be achieved by extending the use of low-density magnesium components in manufacturing industry. Magnesium is an attractive engineering metal; in particular, it possesses a very low density of only 1.74 g/cm^3 , which is significantly lighter than for aluminium (2.70 g/cm^3), and less than a quarter of the density of iron (7.86 g/cm^3) [18]. The physical properties of magnesium, aluminium and iron are shown and compared in **Table 2.1**.

Properties	Magnesium	Aluminium	Iron
Crystal Structure	HCP	FCC	BCC
Density at 20°C (g/cm^3)	1.74	2.70	7.86
Elastic Modulus (GPa)	44	67	208
Melting Point ($^\circ\text{C}$)	650	660	1538

Table 2.1 Physical Properties of Mg, Al, and Fe[19]

In addition to the properties displayed in **Table 2.1**, magnesium has high thermal conductivity, high dimensional stability, good electromagnetic shielding characteristics, good noise and vibration dampening characteristics, good machinability and castability [20, 21]. As the eighth most common element in the earth's crust, the sources of magnesium ore are abundant. Magnesium can be readily extracted from Mg-rich minerals, such as Dolomite ($\text{CaMg}(\text{CO}_3)_2$), Magnesite (MgCO_3) and Carnallite ($\text{KMgCl}_3 \cdot 6\text{H}_2\text{O}$) by calcination, metallothermic reduction or the electrolysis of molten magnesium chloride extracted from seawater. As magnesium is easily recyclable, instituting a corresponding recycling system will extend supplies and further save energy.

Alloying magnesium with aluminium, manganese, rare earths, thorium, zinc or zirconium to increase the strength, without significant sacrifice of light weight, makes them competitive materials for applications where weight reduction is important. Therefore, commonly used structural materials, not only steels, cast iron and copper based alloys, but even some aluminium alloys can potentially be replaced by magnesium-based alloys [22, 23].

The specific strength (also known as strength-to-weight ratio) which is an important indicator for design of weight-saving components of pure magnesium, aluminium, their common alloys and of stainless steels (for comparison) are summarised in **Figure 2.1**.

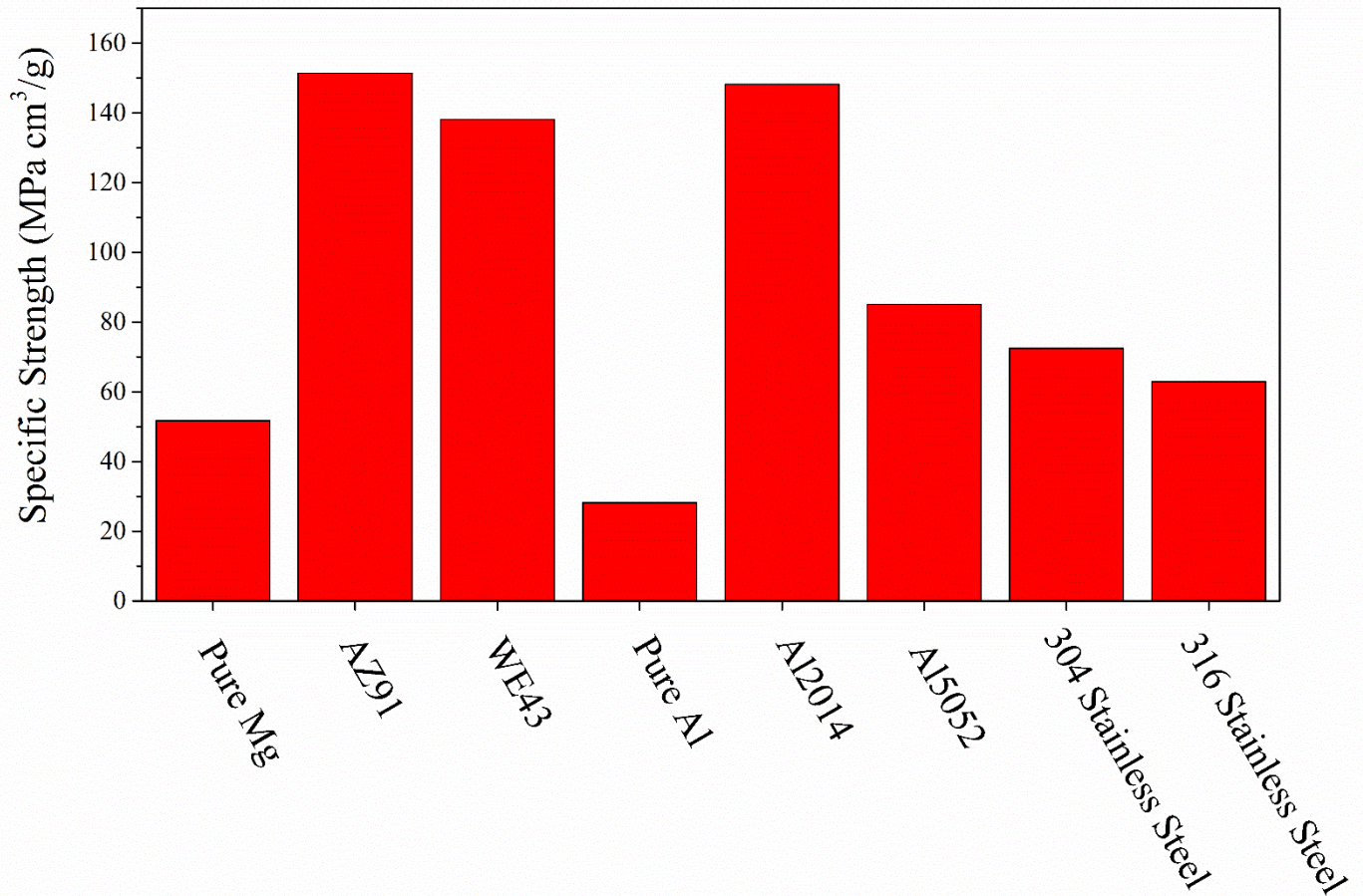


Figure 2.1 A summary of specific strengths of Mg, Al, their several alloys, and stainless steels [24, 25]

As shown in **Figure 2.1**, the specific strengths of magnesium alloys such as AZ91 and WE43 are significantly higher than those of 5052 aluminium alloy (containing 2.2-2.8 wt% Mg), of 304 and 316 stainless steels-and comparable to that of high-strength 2014 aluminium-copper alloy.

Magnesium also possesses a low specific heat capacity and latent heat of fusion-both of which make it desirable for all sorts of casting operations, giving rise to a considerable reduction in energy consumption in the manufacturing process (despite a similar melting temperature to aluminium for example). Furthermore, as it has a low chemical affinity to steel, moulds used to cast magnesium alloys, typically last three to four times longer than those used to cast aluminium [26]. Combining these advantages, magnesium alloys show the most promising potential in manufacturing industry to make lighter and more environmentally friendly metallic products.

2.3. Limitations of Magnesium Alloys

Despite the promising technical and commercial advantages of magnesium alloys detailed above, several undesirable properties preclude their more widespread use. Poor corrosion resistance in many environments severely restricts applications only to benign environments, such as ambient atmospheric exposure at low humidity. The standard electrode potential of magnesium is very low at -2.37V (even compared to aluminium which, at -1.66V, is already a highly electronegative element), indicating its high dissolution tendency by oxidation reactions in aqueous solution—particularly when in contact with other metals with which magnesium will tend to act galvanically as a corroding anode. The Pourbaix diagram of magnesium displayed in **Figure 2.2** demonstrates clearly its strong corrosion tendency, that is thermodynamically favourable at most typical electropotentials when it is exposed to aqueous solutions of $\text{pH} < 11.3$.

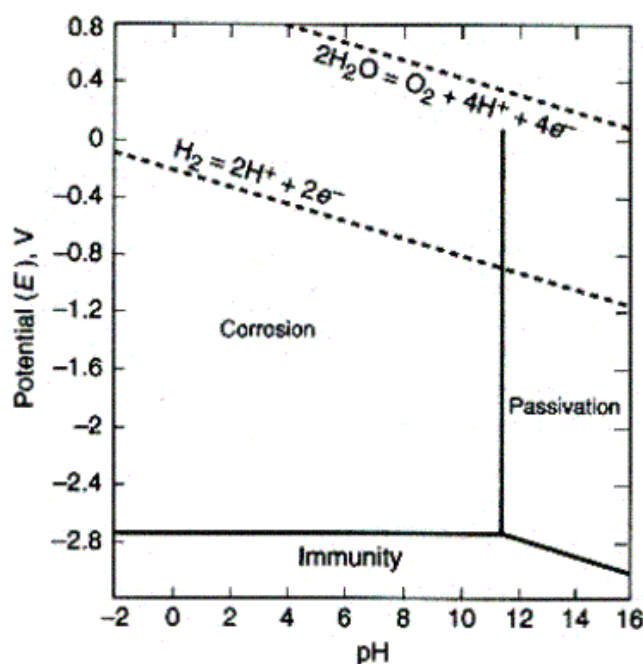


Figure 2.2 Pourbaix diagram of magnesium at 25 °C water [27]

In **Figure 2.2**, intersecting lines separate the regions of corrosion (with dissolved Mg^{2+} cations), immunity (as a cathode of unreacted Mg), and passivation (with stable and protective corrosion products). Unlike other highly reactive alloys (e.g. titanium alloys) which also have a high affinity to oxygen but form a stable, continuous and adherent surface protective film [28], the film formed on the surface of magnesium alloys consists mainly of magnesium hydroxide (i.e. $Mg(OH)_2$), which can only provide limited protection and is very prone to degrade in the presence of many typical aqueous species. Although relatively resistant to alkali attack, magnesium is very vulnerable in acidic environments as well as in aqueous chloride solution (e.g. seawater) in which $Mg(OH)_2$ will transform to $MgCl_2$ and cause pitting corrosion [29]. Moreover, if the concentration of a certain impurity exceeds a tolerance limit, the corrosion rate of magnesium alloys will be drastically accelerated due to the promoted microgalvanic cell action [30]. This phenomenon is particularly common for Fe, Ni and Cu alloying elements in Magnesium (see **Figure 2.3**).

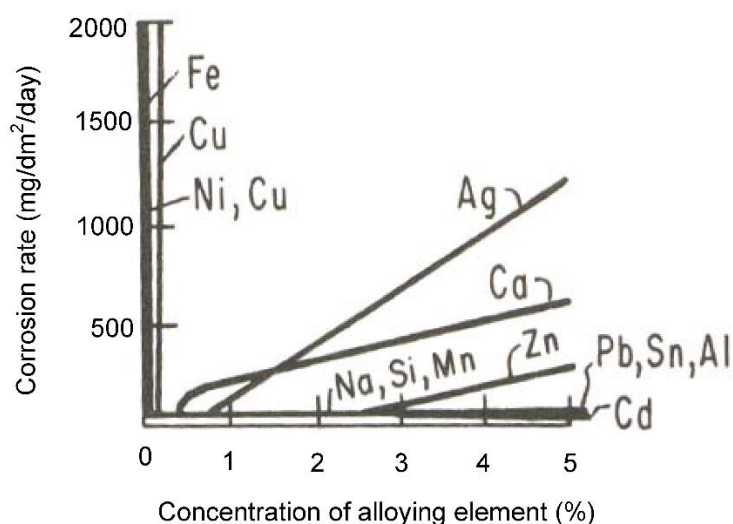


Figure 2.3 Effect of alloying elements on corrosion rate of magnesium in 3% NaCl solution at room temperature [31]

Furthermore, poor creep resistance and inadequate ability to work at elevated temperature are also technological barriers of magnesium alloys. Grain boundary sliding has been observed to be the main creep mechanism of magnesium alloys in the stress-temperature ranges [32]. At a high operating temperature, precipitation hardening effects are impaired due to the decomposition of those precipitates (whose thermal stability is generally poor). In Mg-Al alloys, for instance, if exposing to elevated temperature ($>150\text{ }^{\circ}\text{C}$) for long periods, the supersaturated Mg solid solution will transform to an Mg matrix containing coarse Al-based intermetallic precipitates, promoting grain boundary migration and creep deformation [33, 34]. Magnesium seems to creep even at low temperature ($<150\text{ }^{\circ}\text{C}$) by a stress-recovery mechanism in terms of basal slip within the grains (and sub-grain formation), while diffusion-dependent mechanisms dominate at high temperature [35].

Another shortcoming of magnesium alloys is their poor resistance to wear. Compared to the attention given to corrosion and creep resistance, the tribological properties of magnesium alloys are relatively rarely researched. Since the intrinsically formed magnesium oxide film on magnesium alloy surface has a Pilling-Bedworth ratio of only 0.81 (*i.e.* less than unity), this indicates that the oxide film on magnesium alloy tends to be too thin and any attempts to increase the thickness (to provide a corrosion and/or wear barriers) tend to cause it to crack. Thereby, alternative approaches commonly used for other 'reactive' metals (e.g. aluminium and titanium), such as anodising, cannot achieve satisfactory wear and corrosion protection for magnesium alloys. The lack of adequate wear resistance of magnesium alloys seriously constrains their use to static structural applications. For example, components in the automotive industry commonly made of magnesium alloys are mostly instrument panels,

support frames, seat frames, steering wheel core parts, *etc* [18, 23, 36-38]. In future, the use of magnesium alloys could, with appropriate surface engineering technology, potentially be extended to tribological components and assemblies, such as bearings, sliding seals or gears, where the cumulative benefits of light-weighting could be extensively realised. For these active, load-bearing components, both satisfactory wear and corrosion resistance are required, if the magnesium alloys are to be successfully substituted for existing materials.

2.4. Protective Coatings for Magnesium Alloys

From the perspective of metallurgy, two concepts have generally been proposed to impair corrosion damage of magnesium. The first strategy is to produce magnesium alloys with low concentrations of detrimental impurities (typically Fe, Ni and Cu). Secondly, rapid solidification (RS) enhances corrosion resistance of magnesium alloys, in terms of both increasing homogeneity and limiting of solid solubility. RS processing tends to homogenise the material and thus alleviate the effect of local cell action promoted by the accumulation of cathodic phases containing deleterious elements at grain boundary [39]. Limiting solid solubility also enables the formation of fine-scale distribution of new phases, which stabilise detrimental elements in a less harmful form [40].

Actually, depositing a protective coating onto the surface of magnesium alloys is potentially an effective way to enhance corrosion resistance as well as tribological performance. Coatings of sufficient thickness can protect the magnesium alloy substrates via providing a physical barrier between the metal and its environment, to inhibit the corrosive and wear damage. Moreover, by virtue of deliberate design of the composite system (i.e. coating plus substrate), appropriate surface treatments may be able to achieve a function (or performance) that cannot be provided by either the coating or the substrate alone. A number of technologies have been investigated for coating magnesium alloys, including chemical conversion treatment, anodising, painting, electrochemical plating, and, more recently, vapour-phase processes.

2.4.1. *Conversion coatings*

Conversion coatings are produced by converting the surface of a substrate metal to a coating (that could be an oxide, chromate, phosphate or some other compound) by a chemical (or electrochemical) process [41].

Conversion coatings, as the most common surface treatment for magnesium alloys, can provide moderate corrosion protection by acting as an insulating barrier of low solubility between the substrate and the environment and/or containing corrosion inhibiting compounds [42-44]. Chromate conversion coatings have been demonstrated to greatly improve the corrosion resistance on AZ31C, AZ63A and AZ91C magnesium alloys in salt spray tests [42]. A study by Simaranov et al [45] proposed that the protective properties of these chromate conversion coatings result from the presence of $\text{Cr}(\text{OH})_3$ in the film structure. Conversion treatments are also often used as surface preparation for subsequent coating deposition, such as for paints and organic coatings.

The protection given by stand-alone conversion coatings is however limited. Furthermore, a severe concern of conversion coatings is the toxicity of the processing solutions, especially for chromate treatment which involves use of the highly toxic carcinogen, hexavalent chromium, Cr^{6+} [43]. Another challenge of conversion treatment is the difficulty to obtain uniform properties for alloys with non-uniform surface composition.

2.4.2. *Anodising*

Anodising is an effective technique that is widely applied to offer protection to substrates such as aluminium, titanium and magnesium alloys [46]. During the process, the component being treated is immersed in a specially formulated anodising solution and is forced to grow the naturally-occurring oxide film by applying an electric current. For example, anodic coatings formed on ZM21 magnesium alloy were produced in a bath containing ammonium bifluoride, sodium dichromate and phosphoric acid [47].

The oxide film was found to be highly stable when subjected to high humidity, high temperature, thermal cycling tests and thermal vacuum tests. An anodising treatment developed by Dow Chemical Company (known as the “Dow 17 process”) [48] has proved capable for many types of magnesium alloy. The surface films produced by this technique on AZ91D magnesium alloy demonstrated good corrosion and abrasion resistance [49].

However, a major challenge for anodic coatings on magnesium alloys is electrochemical inhomogeneity because of the phase separation in the alloy. Moreover, flaws, porosity, and contamination from mechanical pretreatment can also lead to uneven deposition [50]. Porous surface morphology was both observed on the surfaces of pure magnesium and AZ91D magnesium alloy treated by the “Dow 17 process”. In addition, the uneven film formed on AZ91D magnesium alloy surface was most likely attributed to the presence of intermetallic Al-Mg particles accumulated at the grain boundaries and surface porosity [51].

Another disadvantage is that a ceramic oxide based coating may not have

satisfactory mechanical properties for load-bearing applications, because many soft and compliant substrate materials (such as magnesium alloys, with an elastic modulus of typically only 44 GPa) tend to deform to a larger extent than the (relatively stiff and brittle) surface ceramic coating under mechanical loading (i.e. easy to spall). As previously noted, the Pilling-Bedworth ratio of magnesium oxide film on magnesium is only 0.81, which indicates that the thicker films tend to crack in tension and unable to provide effective protection. Additionally, anodising techniques are risk damaging the fatigue strength of the substrate metal due to localised heating at the surface during the treatment [50]. This not only leads to the inhomogeneous surface properties but impairs mechanical performance of the anodised magnesium alloys.

2.4.3. *Painting*

Painting is another common surface treatment for magnesium alloys. Paint finishing of die cast AZ91D magnesium alloys has been demonstrated to achieve satisfactory corrosion resistance in terms of no sign of blister or corrosion after 4000 h salt spray test and a 3-year atmospheric exposure test [52].

However, a pretreatment is necessary to obtain good paint-base properties and adhesion, which requires either a conversion coating or an anodising process. An appropriate primer is also important, that should be alkali-resistant and based on organic resins [53]. Significant environmental concerns then arise with the coating system, due to the use of harmful materials, such as chromate and volatile organic compounds. Other disadvantages of painted coatings include non-uniform local pigment

volume concentration, non-uniform crosslink density in the organic matrix, and a risk of swelling or degradation after exposure to harsh environments [54].

2.4.4. *Electrochemical plating*

Electrochemical plating is a simple and cost-effective technique by which an electric current is applied to reduce dissolved metal cations in solution to their metallic form on the surface of the workpiece (i.e. electrode, usually the cathode), providing a barrier between the substrate and the environment [55]. The plating process can be divided into two types according to the source of electrons for reduction: if the electrons are supplied from an external polarisation, it is called electroplating; if the electrons are supplied from a chemical reducing agent in solution or by the substrate itself (as in the case of ‘autocatalytic’ deposition of metals such as copper, nickel and palladium- whose aqueous salts can lead themselves to such methods), it is called electroless plating.

To date only zinc and nickel have been successfully plated directly onto magnesium, serving as base layers for subsequent metal deposition (e.g. copper, chromium and gold). Gold plating (with direct nickel plating underneath) is successfully used in space application mostly due to its outstanding stability in vacuum operating environments, while other metal plating coatings have found little commercial application [56-58]. This is attributed to several challenges of electrochemical plating.

Firstly, the coatings produced from an electroplating process normally are not uniform because of different current density distribution across the substrates, that are caused by a non-uniform distribution of intermetallic

phases formed on the substrate surface. Secondly, the extreme reactivity of magnesium leads to rapid formation of an oxide layer on the surface, which is difficult to completely eliminate prior to plating. Thus, an appropriate pretreatment process is required. Finally, the pretreatment process is not only time-consuming but again involves toxic chemicals, which gives rise to environmental issues and adds cost.

2.4.5. *Vapour-phase deposition*

Protective coatings for magnesium alloys can also be produced by condensation of vaporised materials. Vapour deposition typically involves a process within a vacuum or low-pressure-gaseous environment which effectively avoids unnecessary collisions between depositing materials and impurities in the air.

Two typical categories of vapour deposition are chemical vapour deposition (CVD) and physical vapour deposition (PVD) [59]. Compared with conventional CVD techniques (*i.e.* not involved with plasma), conventional PVD treatments enables the synthesis of functional gradient coatings at lower deposition temperatures. This is important for the surface treatment of magnesium alloys, due to their susceptibility to property degradation at high temperature [60].

According to the type of vapour sources which provides the depositing species, PVD can be categorised as vacuum evaporation, electron-beam PVD (EB-PVD), cathodic arc evaporation and sputter deposition [61]. Vacuum evaporation describes the process whereby gaseous material, which is thermally vaporised from a solid by passing an electric current through the vapour source to heat it, is transported to a substrate in vacuum

environment to form a coating [62]. EB-PVD refers to the process in which a focused high energy electron beam is operated to evaporate target material. The vaporised material from the target is then deposited onto the substrate surface [63]. EB-PVD overcomes melting temperature limitation within conventional vacuum evaporation by the introduction of an electron gun to heat the evaporation source and, in turn, leads to vaporisation and ionisation (in case of plasma-assisted processes) of target atoms [64]. Cathodic arc deposition utilises high current, low-voltage electric arcs in a low-pressure vacuum atmosphere; the arcs are electromagnetically steered over a solid target material to initiate the local heating and thus vaporisation is a particular type of thermal evaporation by local, instantaneous micro-melting [65]. Sputter deposition refers to a process where vaporised material is converted atomistically from solid to (partially-ionised) gas by energetic particle bombardment from a target material and transported to deposit on the substrate [66].

An amorphous/nanocrystalline Al-Cr-Fe film design has been previously demonstrated to enhance the corrosion resistance of AZ31 magnesium alloy, using the magnetron sputtering PVD technique [67]. The performance of an amorphous layer located at the outmost surface and an inner lamellar nanocrystalline layer (with a grain size of less than 10 nm) was compared with untreated AZ31 magnesium alloy; it was found that the Al-Cr-Fe amorphous/nanocrystalline film revealed more positive corrosion potentials and lower corrosion current densities. X-ray photoelectron spectroscopy (XPS) tests indicated that the composition of Al-Cr-Fe passive film was enriched with Cr_2O_3 , Fe_2O_3 and Al_2O_3 at the outer surface and Cr_2O_3 , FeO and Al_2O_3 at the inner layer.

A multi-magnetron sputtering PVD technique has been used to prepare ceramic/metal duplex coatings on AZ31 magnesium alloy to improve the

mechanical and corrosion performance. Two different protective coating structures (i.e. Al₂O₃/Al and Al₂O₃/Ti) were produced and compared [4]. Both coatings exhibited very uniform and compact morphology, as observed by optical microscopy. Although the thicknesses of these two coating systems are almost the same (i.e. 1.2 μm), a superior mechanical property of Al₂O₃/Ti coating compared to Al₂O₃/Al was claimed, being primarily attributed to stronger adhesion and higher microhardness of the Ti interlayer. However, in corrosion tests, the Al₂O₃/Al coating protected the substrate more effectively in 3.5 wt. % NaCl solution. The accelerating galvanic corrosion rate of Al₂O₃/Ti coating was said to be mainly due to the existence of pores and cracks in the coating.

Recently, a coating concept based on a TiMgN ceramic nitride coating has been developed using magnetron sputtering PVD technique [68]. A study by Hoche *et al* [69] has demonstrated the prospective potential of depositing a TiMgAlN alloy-nitride coating (developed from a previously-reported TiMgN coating), onto magnesium alloys against wear and corrosion, in which the increasing Mg content not only densified the coating microstructure, but also improved the mechanical and electrochemical properties [70]. Further enhancement of corrosion resistance was achieved by applying high power impulse magnetron sputtering (HiPIMS) sputtering mode and alloying with the Gd rare-earth element. The TiMgGdN-HiPIMS coating exhibited superior corrosion resistance in terms of being subjected to salt spray testing for as long as 360 hours [69].

As a successful technique to enhance the lifetime of many industrial tools and components [2], PVD offers an environmentally friendly coating process for magnesium alloys. Moreover, PVD overcomes the limitations of phase separation in the alloy and formation of surface oxides (by an ion-

sputter cleaning process prior to deposition) to provide uniform and adherent protective coatings. Overall, PVD is a promising surface treatment to extend the applications of magnesium alloys by improving the corrosion and wear resistance.

CHAPTER 3: PVD COATINGS FOR MAGNESIUM ALLOYS

Physical Vapour Deposition (PVD) is a surface modification technique in which vaporised atoms or molecules from a solid or liquid source are transferred and condensed onto a substrate surface in a vacuum or low-pressure gaseous environment [59]. PVD possesses the advantages of achieving controlled coating structure, strong adhesion, compound layers with functional gradient properties and low deposition temperatures [60].

3.1. Advanced plasma assisted physical vapour deposition processes

The concept of plasma assisted physical vapour deposition (PAPVD) was first patented by Berghaus in 1938 [71], but it was not until 1964 that Mattox introduced the term “ion plating” which led to research being conducted into the formation of metallic films by ion vapour deposition (IVD) [72]. Bunshah and Matthews thereafter developed enhanced plasma systems to increase ionisation and obtain dense ceramic hard coatings with dramatically improved mechanical and tribological properties [73-76]. In low energy deposition, neutral depositing atoms arrive at the substrate surface with little energy for adatom mobility [77], resulting in low film density and poor adhesion. However, in plasma assisted processes, the plasma (consisting of energetic neutral and ionised species) provides essential activation energy by exciting the depositing atoms to a high energy level, thereby improving kinetic adhesion, and the rate and ease of deposition of films with the desired properties. This therefore enables more types of coating to be synthesised at lower deposition temperatures. The

plasma plays a significant role in activating the reactions during the deposition process. This assists in forming compound films such as ceramic transition-metal nitrides, and modifies the growth kinetics and structure morphology of the deposited film. Thus, the physical properties can be altered [78]. PAPVD allows the deposition of various metals, alloys, ceramic and polymer coatings on a wide range of substrate materials [79]. Three main commercial PAPVD types are widely used: plasma assisted electron beam physical vapour deposition (EB-PVD), electromagnetically steered cathodic arc evaporation (CAE) and closed-field unbalanced-magnetron sputtering (CFUBMS).

3.1.1. Plasma Assisted Electron Beam Evaporative PVD

Electron beam physical vapour deposition (EB-PVD) refers to the process in which a focused high energy electron beam is operated to evaporate target material to form a coating vapour flux. The vaporised material from the target is then deposited onto the substrate surface [63]. Flexibility of EB-PVD process can be achieved by combining several electron beam guns with an ingot feeding system that can provide multiple coating sources. [80].

In practice, EB-PVD has widespread applications in the production of thermal barrier coatings (TBCs) which protect the underlying substrate components from overheating damage and creep, in high temperature loading-bearing applications. The plasma thermal spray technique was the main surface treatment used to produce TBCs previously. Compared with plasma-sprayed coatings, EB-PVD coatings possess the following superior properties: (i) a columnar microstructure with increased strain tolerance under thermal cycling [81]; (ii) better oxidation resistance [82]; (iii) greater

erosion resistance [83]; (iv) improved adhesion [84]; (v) a smoother surface morphology; (vi) ease of operation compared to plasma-spraying.

However, as basic EB-PVD in a vacuum environment is a line-of-sight process, a careful rotating operation is required to achieve good uniformity in a deposited coating. This leads to the introduction of a plasma assisted coating process. The use of plasma improves the uniformity of the coating produced by EB-PVD significantly as the plasma covers the substrate surface homogeneously. Furthermore, plasma assisted EB-PVD enhances ionisation. The high ionisation achieved for the depositing materials enables the densification of coatings without increasing deposition temperature [85].

To further improve the ionisation, an ion source can be introduced to assist the deposition process. The introduced gas (argon is commonly used) can be ionised by energetic electrons emitted from a negatively biased filament. A magnetic field is used to facilitate the ionisation process, by both exciting the electrons and also to constrain the resultant plasma within the discharge chamber [86]. Another alternative method to improve the ionisation efficiency is to employ a series of grids which serve to hinder the electrons from being attracted into the output ion beams [87].

3.1.2. *Electromagnetically Steered Cathodic Arc Evaporation*

Cathodic arc evaporation (CAE) is a technique which creates a high-current and low-voltage arc discharge over the surface of a conductive cathode (*i.e.* the target) in a vacuum environment. The cathode material is then evaporated as a fully ionised plasma and is in turn deposited onto the substrate [88, 89]. The main advantages of the CAE process are the capability of achieving a high degree of ionisation and high ion energies. The non-stationary position where the arc discharge occurs at high current density is called the cathode spot [90, 91]. The performance of CAE can be improved by making use of a steering variable magnetic field, where an electromagnetic coil is applied to steer the arc spot motion. For this process, the manipulation procedure avoids overheating of the cathode spot, ensures uniform erosion and reduces the size/number of metal droplets incorporated into vapour flux [92, 93].

These so-called “macrodroplets” are commonly found with a size range of 0.1-10 μm [94, 95]. If the emitted macrodroplets adhere to the growing film, it will lead to surface roughening, degradation of compositional uniformity and may consequently lead to exfoliation of the film [2]. Various measures have been developed to prevent the droplets from reaching the substrate. Generally, two main methods are available. The simpler one is to put a superconductor shield in front of the substrate which physically blocks the incident neutral macrodroplets. The depositing ions within the plasma are transported behind the shield, directed by a magnetic field [96, 97]. Another more effective method is by using a magnetically filtered cathodic arc evaporation. As shown in **Figure 3.1**, the trajectory between the cathode and substrate in the configuration of the magnetically

filtered cathodic arc evaporation is curved. The electromagnetic field bends the electron paths, and depositing ions follow the electrons, to maintain volumetric charge neutrality in the plasma. Furthermore, a series of baffles on the inner wall of duct act to trap the generated macrodroplets by causing them to deposit on the wall, rather than on the substrate.

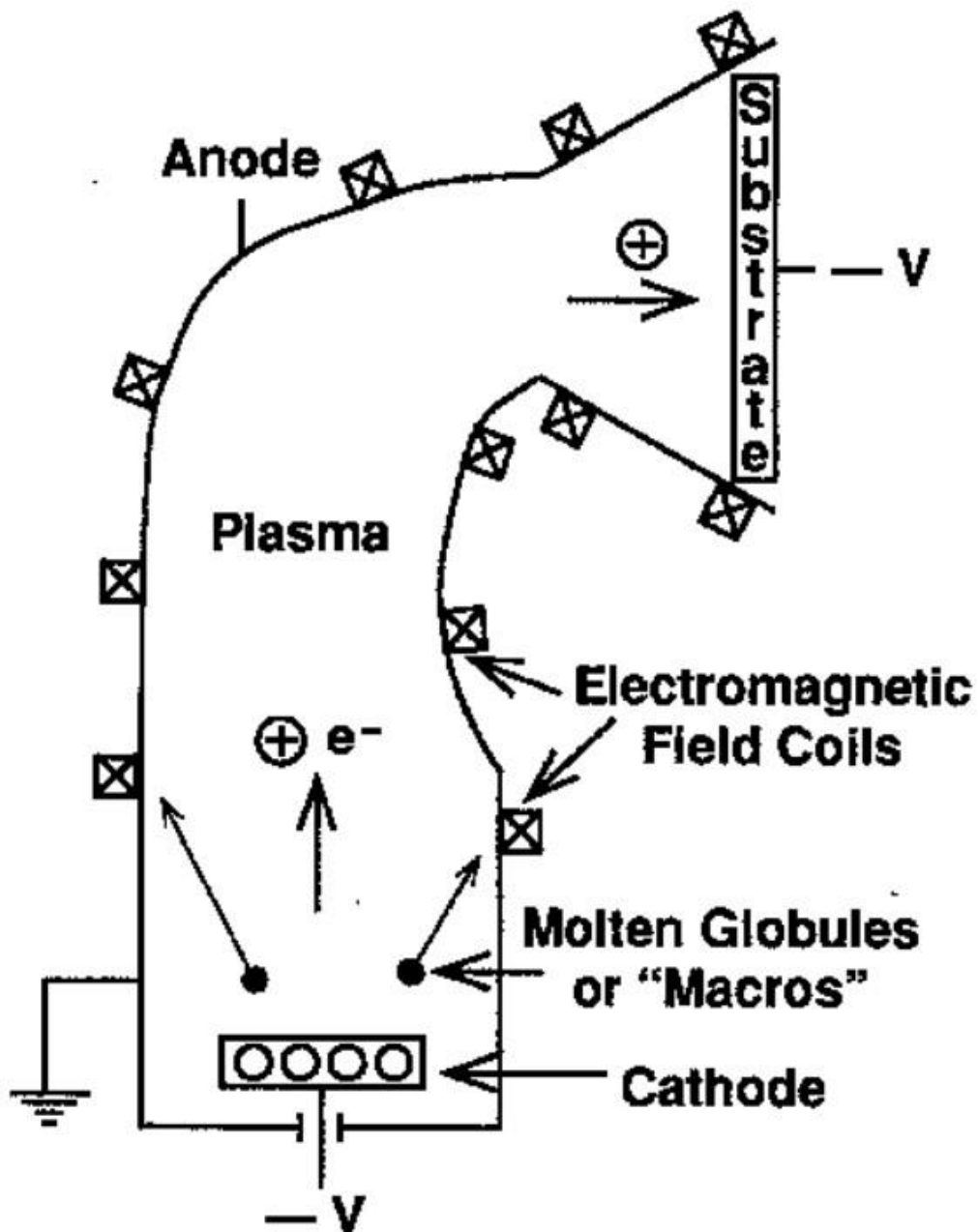


Figure 3.1 The Curved Configuration of Magnetically Filtered Cathodic Arc Evaporation System [61]

Depending on their configurations, magnetic macrodroplet filters can be categorised as either closed-architecture filters or open-architecture filters. The closed-architecture filters are characterised by an enclosure and duct which is surrounded by magnetic field coils – such as the classic 90° duct filter [98], the 45° Knee filter [99], and the rectilinear filter [100]. The macrodroplets are expected to adhere to the duct wall or to be caught by the baffles. However, some types of macrodroplets are more difficult to catch. Carbon, for instance, reflects elastically from the filter surfaces. This “bouncing” issue leads to the design of open architecture filters. In an open-architecture filter system, there are no duct but instead “free-standing” magnetic field coils are used to eliminate the macrodroplets from the region of plasma transport between each pulsed solenoid’s turn [101-103].

3.1.3. *Closed-Field Unbalanced-Magnetron Sputtering*

In the basic sputtering process, during bombardment secondary electrons (along with sputtered target atoms) are also emitted from the target surface. This causes ion bombardment to play an important role in maintaining the plasma density. Although the basic sputtering process has been successfully applied for many materials [104], it is restricted by a low ionisation efficiency, low deposition rates, and excessive heat generation at the substrate through electron heating. These limitations have been overcome by the use of a magnetron configuration, which effectively improves the control of the secondary electrons. Consequently, more collisions can be triggered to enhance ionisation, which gives rise to densification of the plasma. As a result of this, the dense plasma increases ion bombardment to the target and, in turn, leads to higher sputter yields and thus coating deposition rates [105].

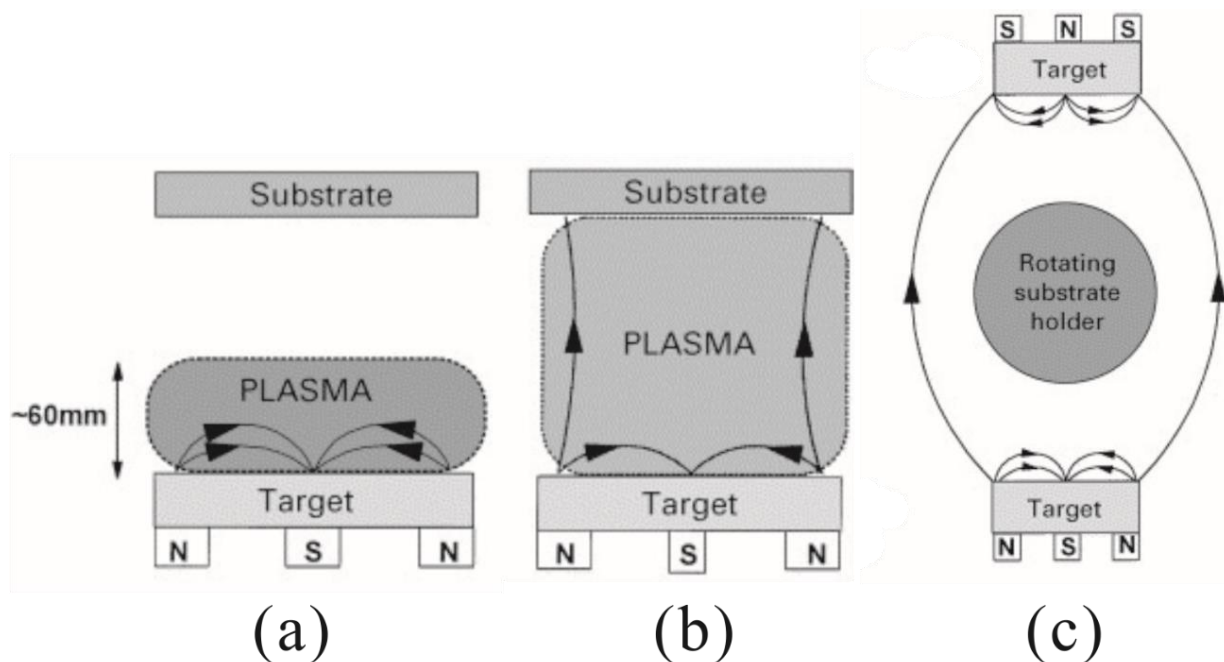


Figure 3.2 Different configurations of magnetron sputtering (a) Balanced magnetron; (b) Unbalanced magnetron (c) Closed-field configuration [106]:

Conventional magnetron sputtering (*i.e.* balanced magnetron sputtering, see **Figure 3.2(a)**) possesses only has a small region containing dense plasma, approximately 60 mm from the target surface. If the substrate is installed within the region, concurrent electron bombardment will severely influence the microstructure and properties of the growing film. Outside of this region, ion density will, on the other hand, be insufficient (normally $< 1\text{mA/cm}^2$) during film growth. As a result, it is difficult to create fully dense and uniform films on large complex shaped components due to the limitation of plasma control [107].

In an unbalanced magnetron system (see **Figure 3.2(b)**), as a result of strengthening the outer ring of magnets relative to the central pole, the magnetic field lines are no longer strongly confined to the region close to target. Some field lines are directed towards substrate which results in a higher ion current flowing to substrate. Consequently, a denser and more

uniform film can be formed by the directed magnetic field [108].

To further develop a uniform coating on a complex component with satisfactory deposition rate, multiple magnetron systems have been introduced. In a multiple magnetron system, the magnetic arrays in adjacent magnetrons can be configured with opposing magnetic polarities to ensure the field lines between the magnetrons are linked. Consequently, a “closed field” is formed which covers the substrate in a high-density plasma region (see **Figure 3.2(c)**). Early research at Salford University [109] indicated that closed-field unbalanced-magnetron sputtering (CFUBMS) systems outperform a single unbalanced magnetron configuration in terms of a substantially improved ion-to-atom ratio. Furthermore, the use of advanced magnetron designs and strong magnets containing rare earth elements can impart a remarkable improvement in ion current towards the substrate [110]. The CFUBMS system is perfectly suitable for the deposition of multicomponent coatings or alloy nitrides because each individual magnetron target can be a different material. By carefully controlling sputtering rate and flow of reactive gas, the desired alloying composition of coatings (including functionally gradient layers) can be obtained [111].

With the CFUBMS technique, several supplementary devices are used, such as target pulse bias and magnetrons with variable field strength. Traditional reactive magnetron sputtering faces a problem when reactively sputtering insulating coating materials. The target surfaces are gradually covered by an insulating layer which steadily accumulates and charges up, and finally brings about breakdown in the form of an arc. Arcing events can give rise to the ejection of droplets from the target. The ejected droplets of the target material produce defects on the substrate surface which lead to detrimental impact on composition and microstructure of the growing

film. The pulsing of magnetron discharges in the medium frequency range (10-200 kHz) during deposition markedly suppresses arc formation and, as a result, decreases the number of defects in the resulting film [112-115]. When CFUBMS is operated using magnetrons in fixed magnetic configuration, the range of ion-to-atom ratios is limited [116], restricting the operational controllability during the process. For instance, a high ion flux is essential in the early stages of deposition to achieve adequate adhesion. However, a continuous intensive ion flux may result in the formation of residual stress and defects in the coating. In order to overcome this limitation, a new magnetron design has been developed to adjust the degree of unbalance *in situ*. Thereby, this system is capable of operating in all modes involving balanced and unbalanced states. Consequently, ion-to-atom ratios at the substrate can be adjusted by means of fine tuning in respect to the fluxes of incident atoms and ions at any stage of the deposition process. Moreover, in the case of depositing graded or multi-layer coatings, variable magnetrons improve the optimisation of component properties in the coating [106].

3.2. Selection of an appropriate PVD coating for magnesium alloys

The PVD technique has been applied in a wide range of industries (*e.g.* tribology and wear/friction control, corrosion, optical and optoelectronic coatings, *etc.*; energy industry and power generation) and a large number of PVD coatings have been developed for different purpose. In general, conventional PVD coatings used for improving wear and corrosion resistances are mostly monolithic coatings of transition metal carbides, nitrides, oxides and borides (*e.g.* WC, TiN, Al₂O₃, ZrB₂ *etc.*) [117, 118] and Diamond-Like Carbon (DLC) coatings [119].

For many years, the imperative for many coating tribologists has been to produce ever harder coatings. However, high hardness is often associated with high elastic modulus, which is likely to cause incoherent strain behaviours of coating and low-strength, low-modulus substrate (*e.g.* magnesium alloys in this research) under load. The much smaller elastic deflection of the hard coating in comparison to the underlying substrate means that it will be easily placed in excessive tension which will thus reduce the coating lifetime in wear applications.

With regards to this, a novel PVD coating with so-called “nanocomposite” microstructure holds a significant promise to avoid such problems. Leyland and Matthews [10] pointed out the relevance of using the ratio of hardness to elastic modulus (H/E) as an indicator of coating mechanical durability and introduced the concept of metallic nanocomposite coatings [11] which, although not necessarily exhibiting extreme hardness, may offer superior protection by providing enhanced resilience and/or ‘engineering toughness’ (*i.e.* a significantly improved ability to accommodate both elastic and plastic strains under mechanical or tribological loading).

Metallic nanocomposite coatings with moderately high hardness and low elastic modulus tend to exhibit a long elastic strain-to-failure and demonstrate an ability to accommodate plastic strains either in themselves or by the substrate. Moreover, glassy nanocomposite (*i.e.* amorphous, but with embedded nanocrystallites) coatings are expected to have good corrosion resistance with more uniform sacrificial behaviour and reduced pitting due to largely absence of grain boundaries [120]. Such properties are clearly suitable for magnesium alloys [11].

3.3. Design concepts of nanocomposite PVD coatings

The potential benefits of producing bulk amorphous magnesium alloys have been recognised in terms of improved corrosion resistance [40] and many unique mechanical properties, which make them excellent candidates for some specific engineering applications [121]. In general, three empirical rules have been suggested to produce bulk amorphous alloys with high glass forming ability [122]:

- 1) Multicomponent systems containing more than three elements
- 2) Significant difference in atomic size ratios above about 12% among the three main constituent elements
- 3) Negative heats of mixing among the three main constituent elements

Similarly, deliberate selection of several elements with low-miscibility in the solid state allows for the creation of glassy-metal or partially amorphous nanocomposites with elastic properties similar to a magnesium

alloy substrate [123].

In addition to the three empirical rules introduced above, for a suitable coating for low modulus magnesium alloy substrates, the candidate elements should ideally have the following properties:

- 1) Low elastic moduli (to match that of the magnesium substrate)
- 2) Different crystallographic structures (to disrupt the crystallisation process on deposition)
- 3) Consisting of strong nitride-forming elements and weaker or non-nitride-forming elements (to develop hard, nitrogen-rich nanograins embedded within a compliant amorphous matrix, for example)

When these properties are combined with the previously stated empirical rules, the design and production of glassy/nanostructured coatings which have mechanical properties close to the underlying magnesium alloy substrate may be possible. Moreover, with moderate introduction of nitrogen, a nitrogen-doped metallic phase (*i.e.* metal-metal nanocomposite) may be formed to give solid solution hardening effect. Alternatively, further addition of nitrogen could lead to the formation of a hard nitride nanocrystalline phase (*i.e.* ceramic-metal nanocomposite). These types of nanocomposite coating appear promising in their ability to provide outstanding protection to magnesium alloys and are thus the focus of the studies in this thesis; since there is no work in the literature currently introducing multi-element amorphous metallic layers to protect (and provide ceramic coating load support for) magnesium alloys.

A desired model of nanocomposite coating is to have nano-scale crystalline grains embedded in an amorphous matrix which separate the grains [124].

In this microstructure, the high volume of grain boundaries between the crystalline and amorphous phases act as a role to restrict the initial crack size and its propagation.

In this project, Al, Mg, B, Zr, Mo and Cu six elements in total (five substitutional metallic elements and one interstitial metalloid) were chosen. The six elements showed large difference in atomic size and different preferred crystallographic structures (see in **Table 3.2**). The addition of these incompatible elements is expected to frustrate the formation of a regular crystalline lattice; thus, the creation of amorphous phases (and/or nanocomposite structures) is thermodynamically favourable [122, 125].

Element	Crystallographic structure	Atomic radius (pm)	Elastic modulus (GPa)
<i><u>Strong nitride-forming element</u></i>			
<i>Al</i>	fcc	125	70
<i>Zr</i>	hcp	160	68
<i>Mo</i>	bcc	145	330
<i><u>Weaker or non-nitride-forming element</u></i>			
<i>Cu</i>	fcc	135	124
<i>Mg</i>	hcp	150	44

Table 3.2 Crystallographic structures, atomic radii and elastic moduli of selected elements

The group of “strong nitride-forming elements” (*i.e.* Al, Zr and Mo) are expected to yield hard metallic phases (by interstitial boron solid solution strengthening) or possibly ceramic boride phases in the film. Cu and Mg

are selected as “weaker or non-nitride-forming elements” and are expected to assist in creating an amorphous matrix that will reduce the overall elastic modulus of the coating system. Adding Al and Mg should also increase the adhesion of the interfacial layer, since both are galvanically and elastically compatible with the magnesium alloy substrate. Furthermore, in the previous research [126] partially amorphous structures were found to form in nitrogen-free binary-alloy Zr-Cu coatings. As outlined above, the introduction of boron not only improves solid solution strengthening by increasing lattice friction, but can also lead to the formation of hard and refractory borides with elements such as Al and Zr (or Mo) [127].

CHAPTER 4: EXPERIMENTAL PROCEDURE

4.1. Substrate Preparation

4.1.1. WE43 magnesium alloy selection

Due to concerns about possible zinc element contamination (*i.e.* a risk of floating around the chamber when voltage is applied), any zinc-containing magnesium alloy, such as AZ and ZK series, was avoided. As a result, WE43 magnesium alloy was selected as the substrate material for the project. Some basic properties of WE43 magnesium alloy are listed in **Table 4.1**.

Elektron WE43

<i>Composition (wt%)</i>	Yt: 4.2 wt.%; Nd: 2.3 wt.%; Zr: 0.7 wt.%, other heavy rare earth elements: 0.8 wt.% ; Mg: balance
<i>Heat Treatment</i>	T6: Solution (at 525 °C for 8 hours) plus artificial ageing (at 250 °C for 16 hours)
<i>Tensile Strength</i>	220 MPa
<i>0.2% Proof Stress</i>	172 MPa
<i>Modulus of Elasticity</i>	44 GPa
<i>Vickers Hardness</i>	85-105
<i>Creep Property</i>	Stable at 250 °C and use up to 300 °C

Table 4.1 Basic properties of WE43 magnesium alloy

As **Table 4.1** shows, the Elektron-proprietary WE43 magnesium alloy is heat-treated by annealing it at 525 °C for 8 hours and hot water quenched, followed by artificially ageing for 16 hours at 250 °C [128-130]. This leads

to a high strength that can provide essential support in wear testing.

In addition, compared with other Zinc-free magnesium alloy, WE43 is able to maintain good mechanical properties at elevated temperature (up to 250 °C) for long term exposure. The overall temperature of substrate during deposition was measured as 180-200 °C in the Nordiko unbalanced magnetron sputtering rig (for further details see section 4.2.2). Excessive local heating caused by ion bombardment may however arise on certain area of the substrate surface [131]. Good thermal stability of the WE43 magnesium alloy ensures reliable properties of as-deposited samples.

4.1.2. Grinding and polishing

The raw WE43-T6 magnesium alloy was machined as circular pieces with a diameter of 50 mm and a thickness of around 3 mm. The circular substrates were prepared through grinding with SiC abrasive paper P1200, P2500, and P4000. Then they were polished using a mixture of 1 µm diamond paste and suspension, with some addition of soapy water.

The prepared surfaces had a mean surface roughness (Ra) of $0.02 \pm 0.006 \mu\text{m}$. Prior to deposition, the polished substrates were ultrasonically cleaned in acetone and isopropanol solutions, which was then immediately dried with a flow of cool air.

4.2. Coating deposition

Since this project aimed to explore a novel series of PVD nanocomposite coatings for magnesium alloys, there is no related literature to guide coating deposition work.

The overall plan was to produce a metallic glass or a partially amorphous, nanostructured base layer, and then, by adding nitrogen gas, promote the formation of a metal-metal nanocomposite coating structure (with nitrogen-doped metallic phase in an amorphous matrix) or a ceramic-metal nanocomposite coating structure (with nitride ceramic phase in an amorphous matrix). Base layers were first produced with a wide range of compositions by varying both the depositing positions (*i.e.* four positions in each run) and substrate negative bias (*i.e.* 50 V, 60 V, 75 V and 100 V).

Analysis of the results would allow for the best candidate to be selected for the next stage of the design process. Here, four nanocomposite coatings of the selected composition could be produced by adding nitrogen gas with different flow rates (*i.e.* 5 sccm, 10 sccm, 15 sccm and 20 sccm). The coatings were then characterised *via* wear and corrosion tests, to obtain information on the performance.

4.2.1. Sample Designation

As mentioned above, four deposition runs were carried out to produce base layers in terms of different applied substrates negative bias (*i.e.* 50 V, 60 V, 75 V and 100 V). In each run, four as-polished WE43 substrates were placed at intervals along the middle row on a sample holder with dimensions of 300 mm x 130 mm. The distance between P2 and P3 was considerably large as a hole was present on the sample holder. The four substrates were labelled P1, P2, P3, and P4 from left to right (see **Figure 4.1**)

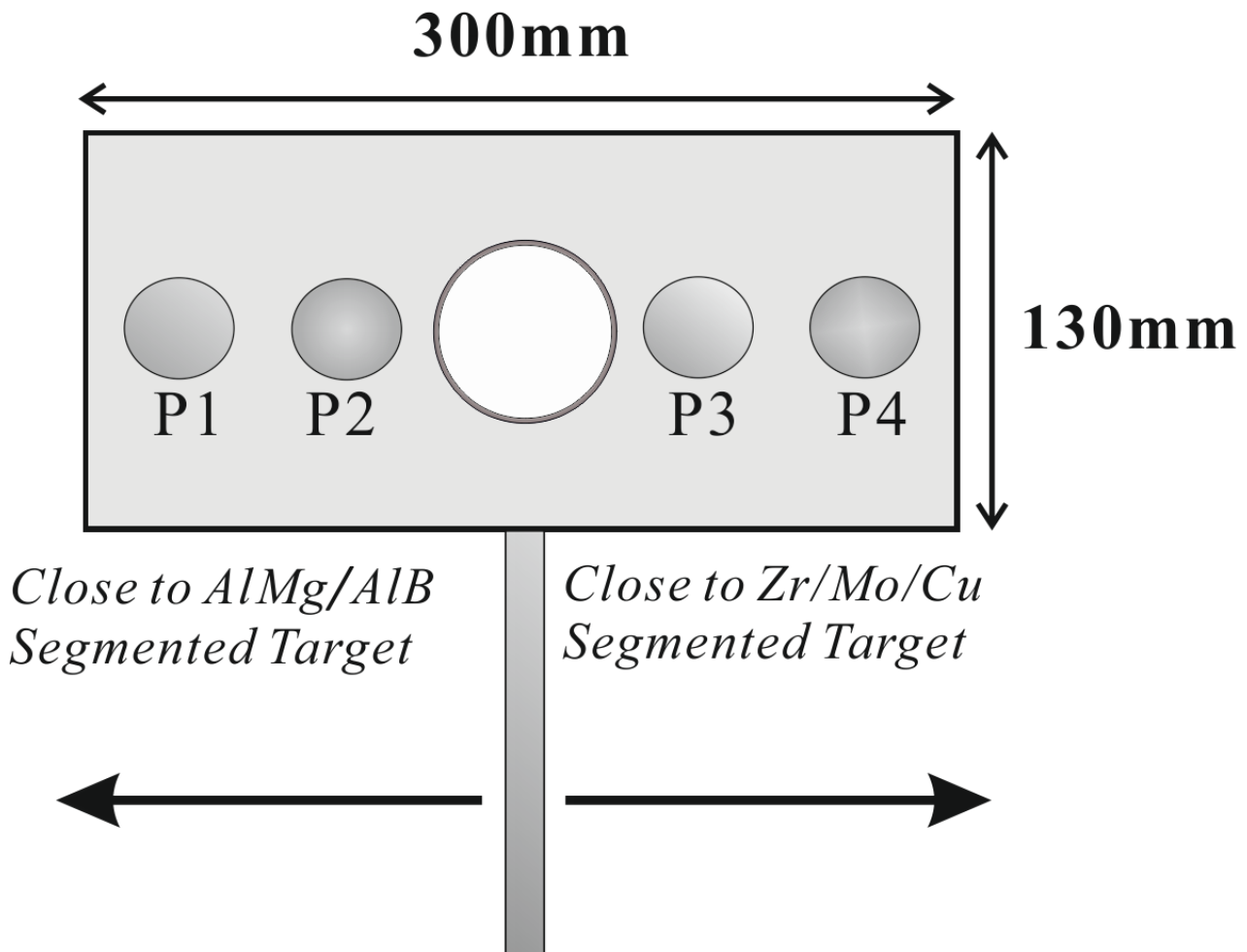


Figure 4.1 Plan-view of substrate holder prior to deposition

The total of sixteen as-deposited base layers were given individual designations as a combination of their positions in the chamber (*i.e.* P1 to P4) with their applied substrate negative bias voltages (*i.e.* 50 V, 60 V, 75 V and 100 V) as shown also in **Table 4.2**

Substrate Negative Bias (V)	Designation	Current (A)
50	P1-50, P2-50, P3-50 and P4-50	0.07
60	P1-60, P2-60, P3-60 and P4-60	0.08
75	P1-75, P2-75, P3-75 and P4-75	0.08
100	P1-100, P2-100, P3-100 and P4-100	0.10

Table 4.2 Classification of AlCuMoMgZrB base layer groups

Similarly, the sample produced from coating deposition process was labelled by adding the corresponding nitrogen content at last (*e.g.* P1-100-20sccm).

4.2.2. Deposition equipment

In this project, all coatings were produced using a Nordiko unbalanced magnetron sputtering machine. As shown in **Figure 4.2**, this rig is equipped with three power supply units (plasma generators): one ENI DCG-100DC plasma generator and two ENI RPG-100 Pulsed DC plasma generators. The Nordiko rig is also fitted with two targets, each placed at an angle of 90°.

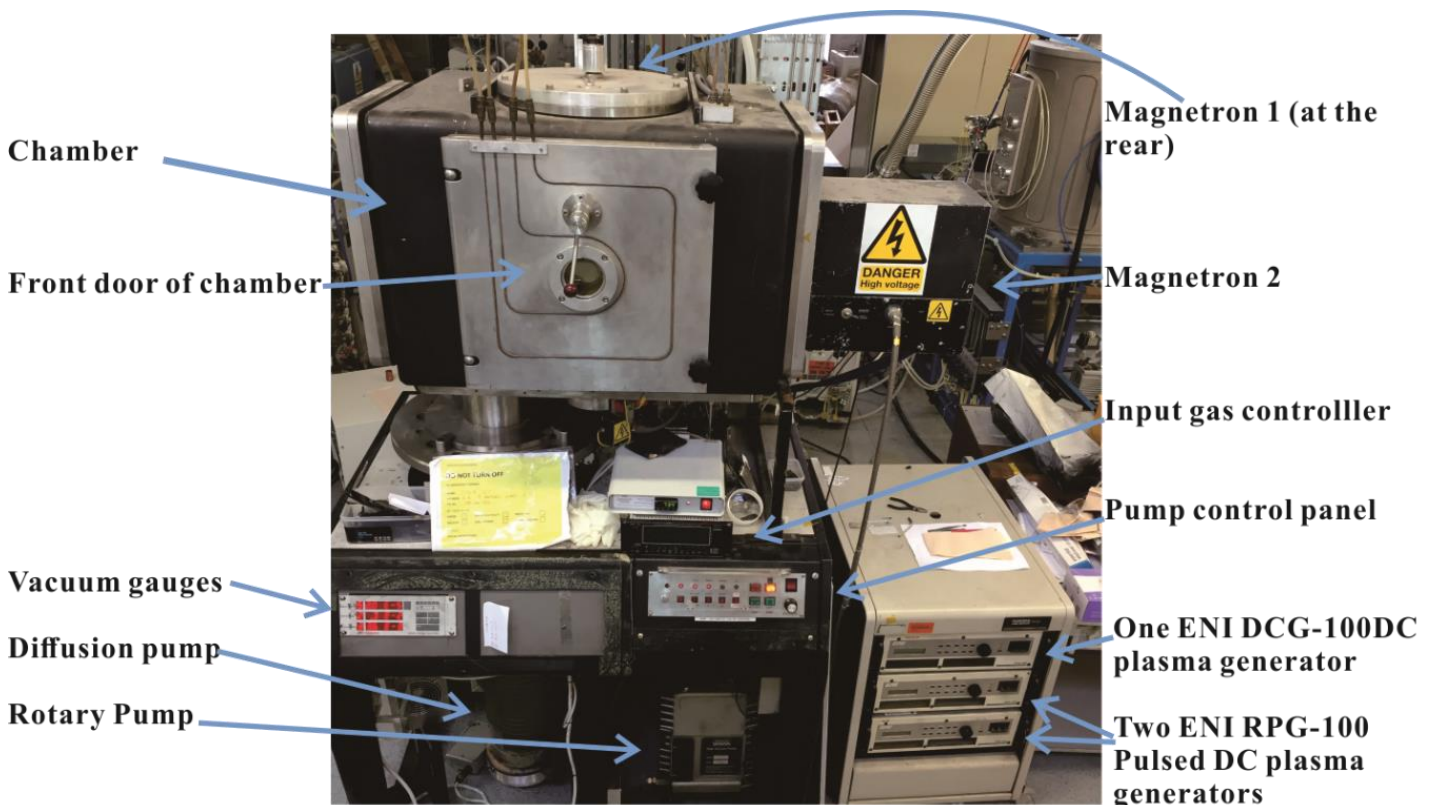


Figure 4.2 The Nordiko unbalanced magnetron sputtering

4.2.3. Target combination

The Nordiko rig has a twin-target configuration (see **Figure 4.2**), each with dimensions of 380 mm x 100 mm x 6.5 mm. As shown in **Figure 4.3**, a two-piece composite combination (*i.e.* AlMg and AlB segments) and a three-piece composite combination (*i.e.* Zr, Mo and Cu segments) were introduced.

These target segments were bonded on to Cu-backing plates with corresponding clamping pieces as **Figure 4.3** shows. Between the target segments and Cu-backing plates, a thin carbon foil was inserted to increase the heat transfer rate of the target configuration.

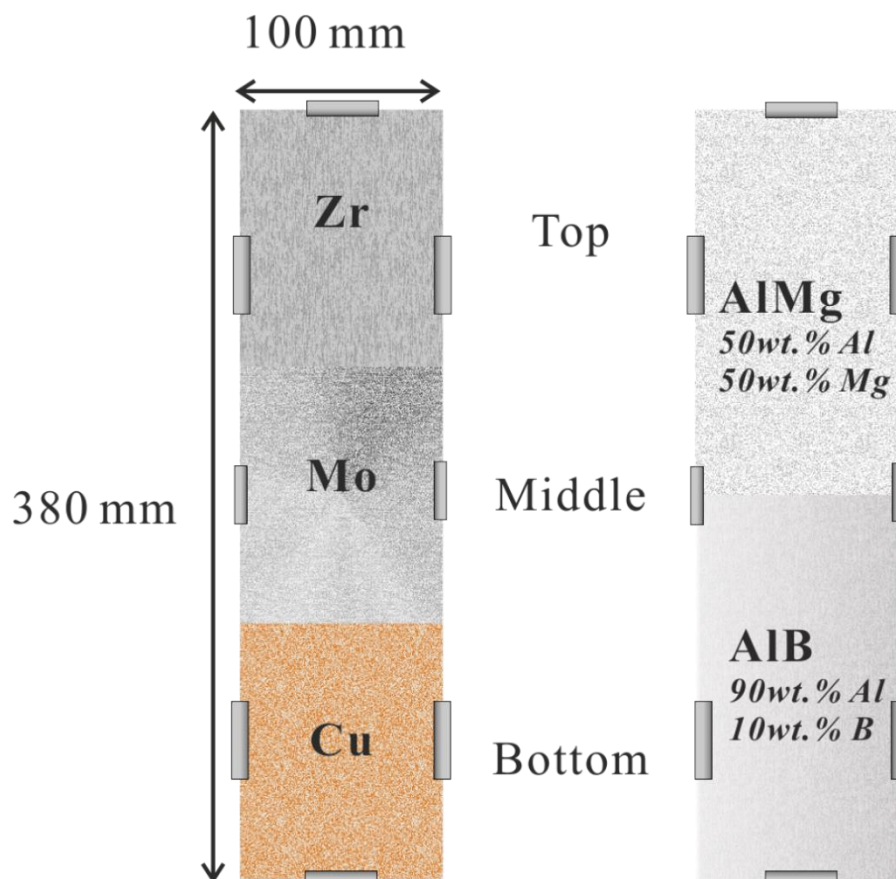


Figure 4.3 Schematic drawing of segmented targets

4.2.4. Deposition configuration

The mounted substrates were then placed into the chamber at an angle of 60° to the AlMg/AlB segmented target (see **Figure 4.4**). The substrates were placed closer to the target to produce Al-rich coatings and to minimise coating thickness variations from sample position to sample position (although uniform coating thickness was not the primary aim of this work). In each run, P1 was the sample closest to the AlMg/AlB segmented target, where else while P4 was the sample closest to Zr/Mo/Cu segmented target (see **Figure 4.1**).

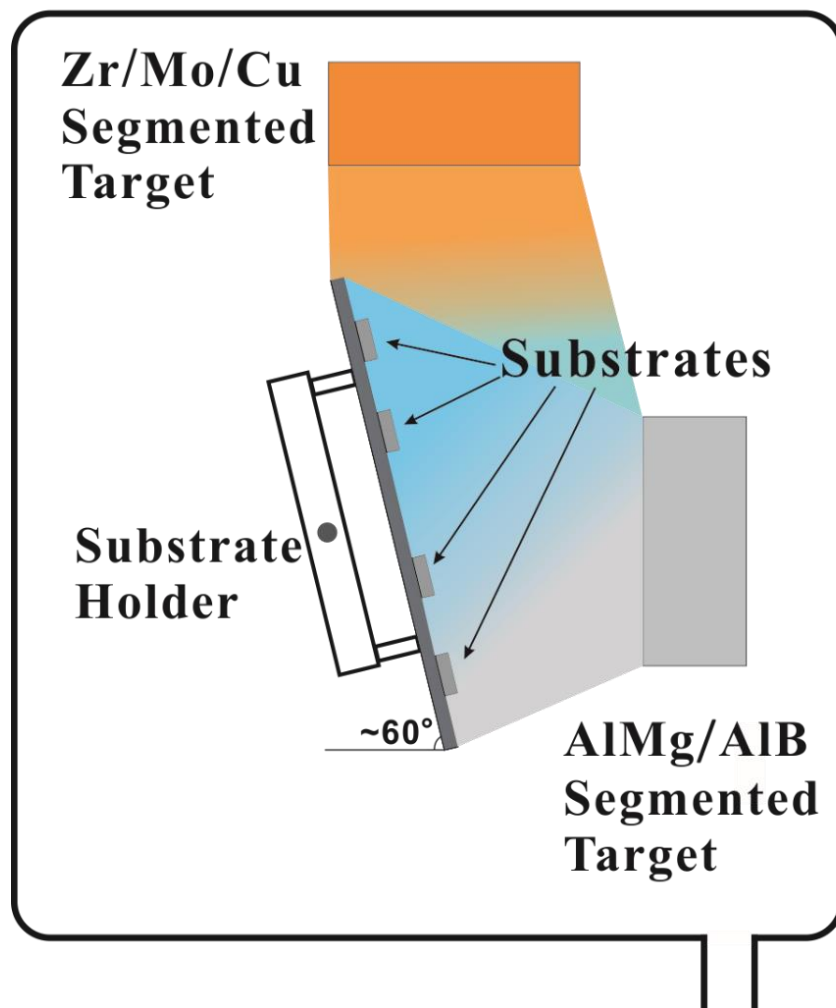


Figure 4.4 Schematic diagram of deposition process

4.2.5. Deposition procedure

The basic deposition parameters used are listed in **Table 4.3** below.

Parameters

<i>Base pressure</i>	0.02 mTorr ($\sim 2.7 \times 10^{-3}$ Pa)
<i>Substrate sputter-cleaning</i>	at 25 mTorr pressure (~ 3.3 Pa; with 28 sccm Ar flow rate) and applying a substrate negative bias of 500 V for 30 minutes
<i>Targets sputter-cleaning</i>	at 2.0mTorr pressure (~ 0.27 Pa; with 9 sccm Ar flow rate) and applying powers of 600 W (~ 330 V) and 400 W (~ 290 V) to AlMg/AlB and Zr/Mo/Cu segmented targets respectively for 30 minutes
<i>Base layer deposition</i>	Keeping the same pressure and powers as “target sputter-cleaning” process; applying a substrate negative bias of 50 V, 60 V, 75 V, and 100 V respectively for 1hour
<i>Nanocomposite coating deposition</i>	Keeping the same depositing parameters as best candidate base layer for the first 1 hour; then adding N ₂ gas with 5 sccm, 10 sccm, 15 sccm and 20 sccm respectively for the next 1 hour.

Table 4.3 Basic deposition parameters of base layers and nanocomposite coatings

Due to the brittle nature of the AlMg segment, the ramping period of AlMg/AlB segmented target (5 minutes) was longer than that of the Zr/Cu/Mo segmented target (1 minutes). In both substrate and targets sputter-cleaning processes, a protective shutter was used to cover the substrate to avoid contamination.

As both segmented targets contained strong nitride-forming elements (Zr, Mo, Al and B), upon introducing nitrogen gas, there was a risk of forming an insulating ceramic layer on the target surface which would be deleterious to the sputtering rate. To overcome this, positive pulses were applied to these segmented targets to achieve 20% duty cycle. The

substrates were applied with pulse-free direct current using the left ENI DCG-100DC unit.

Although no nitrogen is introduced during the base layer deposition, the connections of plasma generators were not changed, in order to avoid possible change in deposition parameters. During the nanocomposite coating deposition process, the final one-hour nitrogen-involved period included 20 minutes of ramping the nitrogen flow rate. Nitrogen content was increased through a ramping period at 5 minute intervals until the desired value was reached. For instance, for P1-60-10sccm, 2 sccm of nitrogen flow rate was initially set after one-hour of base layer deposition. The nitrogen flow rate was then increased by 2 sccm every 5 minutes, until a flow rate of 10 sccm was reached. This resulted in a compositionally graded layer between the base layer and the top nanocomposite coating.

4.3. Coating Analysis

The as-deposited samples were subjected to a series of analytical techniques for investigations of their microstructures, compositions, tribological, and corrosion properties.

4.3.1. X-ray diffraction analysis

X-ray diffraction (XRD) measurements were performed to investigate the phase composition using Siemens D5000 diffractometer (with Cu-K α radiation, $\lambda = 0.15418$ nm, at 30 kV and 40 mA).

The phase compositions of base layers and nanocomposite coatings were analysed by glancing-angle (GA) XRD mode, which was carried out at a fixed glancing angle of 1° to the incident X-ray beam with a step size of 0.02° and a step time of 20s in 20° to 70° detecting 2θ range. The use of GAXRD allowed a shallow X-ray penetration and predominately eliminate the signal interference from substrate.

4.3.2. Scanning electron microscopy observation

Scanning electron microscopy (SEM) was used to observe the morphologies of both the coating surfaces and fracture cross-sections. An accelerating voltage of 5-20 kV was applied using a Philips XL30 field emission gun scanning electron microscope (FEG-SEM) and a FEI Nova NanoSEM 450. The FEI Nova NanoSEM 450 allowed the use of through-lens detection (TLD) mode at low accelerating voltage (<5.0 kV) to give

improved resolution images.

For surface morphology observations, the samples were prepared by sticking on an aluminium stub using an electrical conductive carbon tape. In some cases, the sample surface needed to be sputter-coated with carbon to eliminate the charging interference under electron bombardment during SEM characterisation.

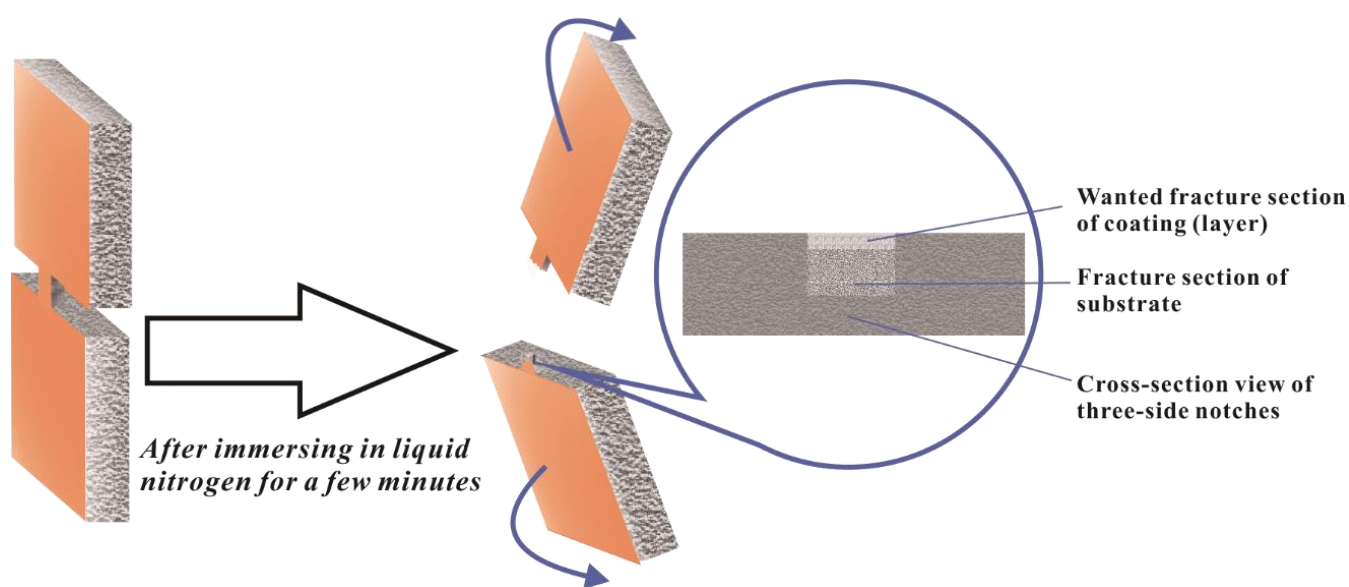


Figure 4.5 Schematic of preparing fracture sections

The fracture appearance exhibits the coating cross-sectional morphology, which cannot be obtained through cross-sectional mounting of the sample as sample preparation (sectioning, grinding, and polishing) would all influence and damage the original coating growing morphology. The preparation of the fracture section sample is as displayed in **Figure 4.5**. Firstly, notches were cut into a small segment of the coated sample, as shown in **Figure 4.5**. The notched samples were then rapidly put in liquid nitrogen. After a few minutes of immersion, the sample became brittle and was fractured by bending in tension (as indicated in **Figure 4.5** by the blue lines). Finally, the fractured cross-sectional morphology can be observed

using SEM by preparing the sample using the method as outlined previously.

4.3.3. *Energy dispersive x-ray analysis*

The quantitative chemical composition analyses of the as-deposited base layers and nanocomposite coatings were carried out by energy dispersive X-ray (EDX) detectors fitted on a JEOL JSM-6400 and Philips XL30 SEM equipment in combination with Oxford Instruments INCA software. The parameters used were an accelerating voltage of 20 kV, a working distance of 5 mm, and spot size of 3.0.

In order to obtain reliable results of the chemical compositions of the samples with boron and nitrogen concentrations, calibrations were performed by using reference specimens with known concentrations. The reference specimens were: AlB (*i.e.* 90 wt%Al and 10 wt%B; ~79 at%Al and 21 at%B), and a AlNiTiSi(B, N) coating of known chemical composition (27.6 at%Al, 8.6 at%Ni, 11.7 at%Ti, 8.4 at%Si, 24 at%B and 17.7 at%N) evaluated independently by both EDX and glow-discharge optical emission spectroscopy (GDOES).

Using these reference specimens, ratios of Al/N and Al/B can then be obtained to indicate values of the corrected elemental compositions. A selection of calibrated results were further confirmed by GDOES analysis which is a sensitive technique for multi-element depth-profiling of surface layers [132, 133].

4.3.4. *Transmission electron microscopy analysis*

Both conventional and high-resolution (HR) transmission electron microscopy (TEM) were applied to analyse a selection of base layers and nanocomposite coatings. Conventional TEM was performed in a Philips EM420 machine (fitted with a tungsten filament and 120 keV accelerating voltage) and a FEI Tecnai T20 (fitted with a LaB₆ filament and 200 keV accelerating voltage). Both voltages were set in the high-tension configuration. Use of both TEM machines allowed the acquisition of bright field (BF) images and dark field (DF) images with corresponding selected area electron diffraction (SAED) patterns. HRTEM was performed by in a JEOL 2010F fitted with a Schottky field emission gun (at 200 keV).

All TEM thin-foil specimens (cross-section) were prepared by a FEI Quanta 200 3D scanning electron microscope fitted with gallium Focused Ion Beam (FIB). The foil was extracted from the surface of a coated sample. Then, after adhering to a copper grid, the foil was ion-milled to a thickness at least less than 100 nm under an accelerating voltage of 30 keV and various currents (smaller current values were used for thinner foils).

4.3.5. *Nanoindentation*

Surface nanoindentation testing was performed to measure the hardness (H) and elastic modulus (E) of all base layers and nanocomposite coatings. A Hysitron. Triboscope® fitted with a Berkovich triangular-pyramidal diamond indenter (with a tip radius of curvature of approximate 150 nm) was exerted. Nine indentations were applied in each run at a load of 1500-3000 μ N to ensure the suitable indentation depth that was ideally limited to around 3% of coating thickness whilst exceeded the minimum allowance of indentation depth of the equipment (*i.e.* 50 nm) [134, 135].

4.3.6. Scratch-adhesion testing

A modified VT scratch-adhesion tester fitted with a Rockwell diamond indenter with a tip radius of 200 μm and spherical heads angle of 120° was used to assess the coated sample's adhesion properties. Due to limitation of the scratch-adhesion tester in which normal load given by the indenter was very unstable in the range of 0-5N (*i.e.* not precise, sometimes even applied an excessive load), a continuously increasing normal load from 5 N to 20 N was performed in each scratch which resulted in a final scratch track with a length of 5 mm. The tangential force was recorded during the test to help to determine critical loads at which the first chipping occurs (*i.e.* L_{C1}), the first adhesive failure occurs (*i.e.* L_{C2}) and the complete removal of layer occurs (*i.e.* L_{C3}). By the assistance of SEM and its fitted EDX detection, the critical loads could also be calculated via measuring the distance of corresponding characteristic failure occurrence. The scratch-adhesion testing for each sample was repeated three times and each scratch scar was separated by 2 mm. **Figure 4.6** illustrates this schematically.

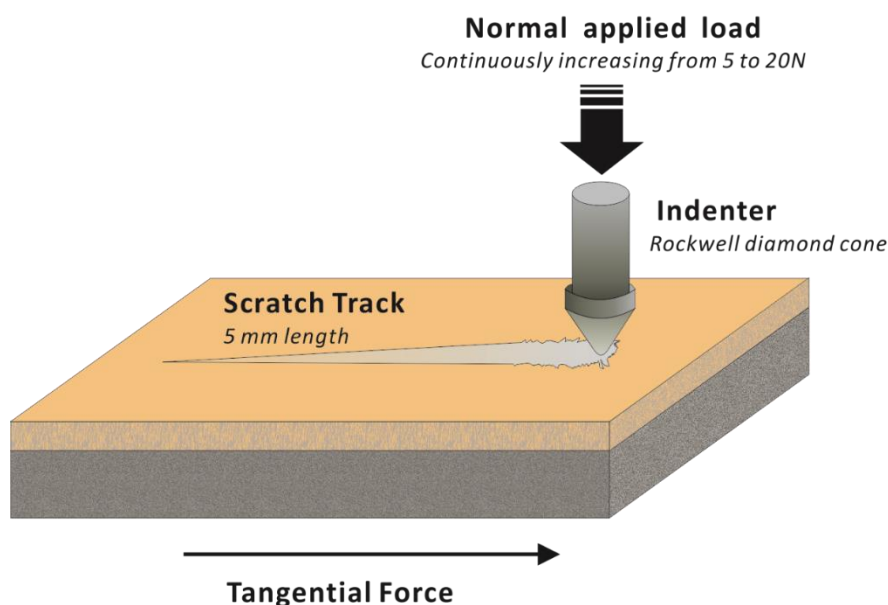


Figure 4.6 Schematic view of scratch-adhesion tester arrangement

4.3.7. *Micro-abrasion wear testing*

4.3.7.1. *Two-body and three-body abrasions*

Micro-abrasion is a convenient technique widely applied to evaluate the tribological information of coating and bulk materials [136-140]. In addition, from the investigation of wear scars, the presence of coating defects (*e.g.* pores and cracks) and adhesive condition could be revealed.

In the micro-abrasion test, the abrasive wear mode can be divided as two-body abrasion and three-body abrasion, a mixture of the previous two modes. Two-body abrasion results from some particles in slurry rigidly embedded onto the ball surface, leaving multiple parallel grooves in the counterface [141]. In three-body abrasion, the particles roll in the contact region by a uniform multiply motion [142]. The study of Adachi and Hutchings [143] has indicated that specific wear rates in 3B abrasion is relatively less dependent on test conditions compared with that in 2B abrasion. Moreover, 2B abrasion is expected to produce non-spherical wear scars which are observed to be full of ridges [144]. The ridges around the edges of the scar make the measure of diameter difficult. Therefore, it leads to a non-linear relationship between load and wear volume. Conversely, a directly proportional relationship between the wear volume and the applied normal load is generally found in 3B abrasion, which makes the subsequent analysis meaningful [141]. Therefore, test conditions of micro-abrasion wear testing favours 3B abrasion.

A ‘fixed-ball’ micro-abrasion apparatus (see **Figure 4.7**) was used in this testing. Prior to each run, a SAE52100 bearing steel ball (with a diameter of 25 mm and hardness of 8.5 GPa) was clamped between coaxial shafts, with the sample being mounted vertically on a pivoted arm. By adjusting the weight system at zero load, the ball and sample surfaces can be configured so that they are in contact with each other. In order to obtain a 3B abrasive wear mode, a SiC abrasive slurry with a concentration of 0.8g/ml was prepared. Moreover, the normal load and ball rotating speed were set as 0.05N and 100rpm.

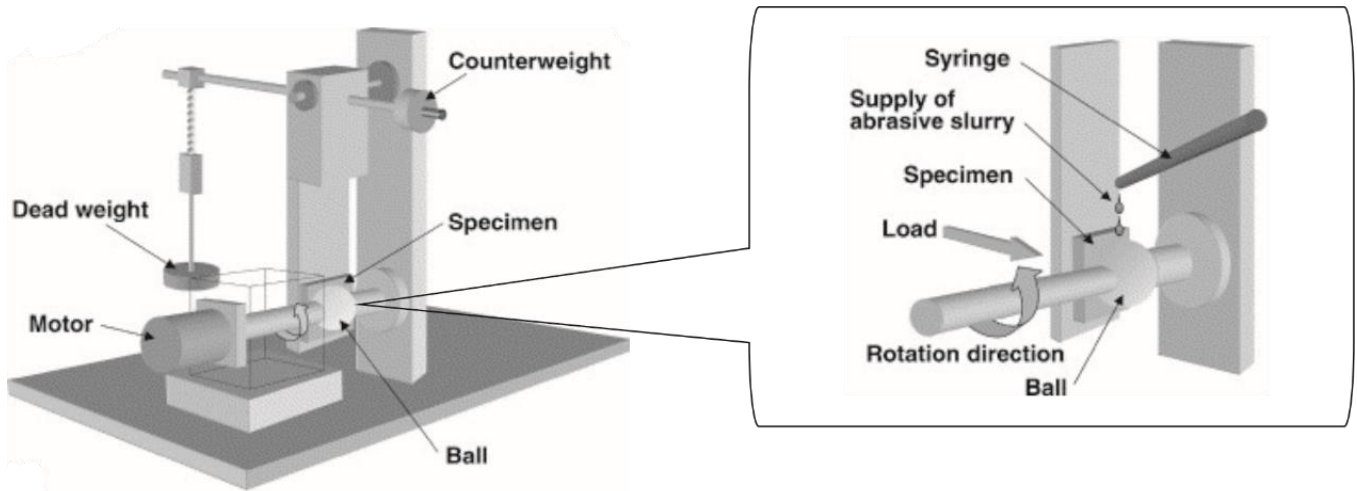


Figure 4.7 Schematic diagram of the “fixed-ball” micro-abrasion apparatus and its operating details [145]

During the micro-abrasion test, a syringe was used to supply the abrasive slurry to the contact zone between the ball and sample. Meanwhile, the slurry was stirred continuously in order to avoid SiC particle agglomeration. After the test, surface micro-profilometry (operated by a Veeco Dektak® 150 stylus profilometer) and SEM were used to observe the wear scars and measure the size.

4.3.7.2. *Test conditions of three-body abrasion*

The wear resistance of the AlCuMoMgZrB(N) coatings was evaluated through micro-abrasion wear testing. As previously introduced, it is favourable to use three-body (3B) abrasive wear mode (*i.e.* rolling) micro-abrasion test conditions rather than two-body (2B) abrasive wear mode (*i.e.* grooving). This is because, in the 3B wear mode, the volume of wear scar produced by uniform rolling abrasion is found to be proportional to applied normal load (*i.e.* highly reproducible).

For the 3B wear abrasive mode, the normal load and the ball rotation speed were chosen as 0.05 N and 100 rpm. A SiC abrasive slurry (with a mean particle size $\sim 3.0 \mu\text{m}$) and a particle concentration of 0.8 g/ml was prepared and used. The surface morphology which was observed *via* SEM confirmed the presence of 3B wear; a typical SEM micrograph is shown in **Figure 4.8**.

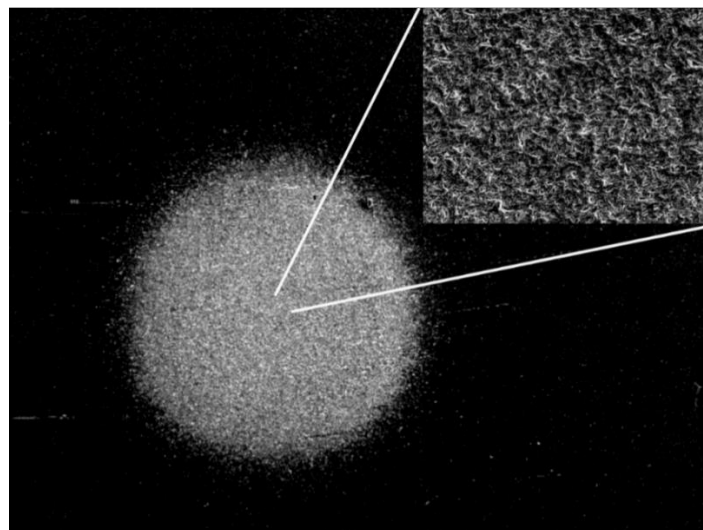


Figure 4.8 SEM image of 3B abrasive wear mode in WE43 Mg alloy

4.3.7.3. Calculation of specific wear rates

Perforating and non-perforating tests were used to determine specific wear rates of the coatings and the substrate (in perforating test). All calculation methods here are derived from Archard's equation for sliding wear [146]:

$$WS = \frac{V}{k} \quad \text{Equation 4.1}$$

where W is the normal load, V is the total wear scar volume, S is the sliding distance and k is the specific wear rate (conventionally quoted in units of mm^3/Nm).

Equation 4.2 and **4.3** below show the calculations of V and S , respectively:

$$V = \frac{\pi b^4}{64R} \quad \text{Equation 4.2}$$

$$S = 2\pi R \cdot Rev \quad \text{Equation 4.3}$$

where b is the crater diameter, R is the radius of the ball and Rev represents the number of revolutions.

Therefore, the specific wear rate of the coating (k_c) in the non-perforating test can be calculated:

$$k_c = \frac{V}{SW} = \frac{\pi b^4}{64R} \cdot \frac{1}{2\pi R \cdot Rev \cdot W} = \frac{b^4}{128R^2 \cdot Rev \cdot W} \quad \text{Equation 4.4}$$

Equation 4.4 has been extended by Rutherford and Hutchings [147, 148] for the combined abrasion of both coating (k_c) and substrate (k_s) in perforating tests:

$$SW = \frac{V_c}{k_c} + \frac{V_s}{k_s} \quad \text{Equation 4.5}$$

V_c and V_s represent the wear volume of coating and substrate, respectively. And the total wear volume (V) is equal to the sum of V_c and V_s . Hence, **Equation 4.5** can be rewritten as [148]:

$$\frac{SW}{V} = \left(\frac{1}{k_c} - \frac{1}{k_s} \right) \frac{V_c}{V} + \frac{1}{k_s} \quad \text{Equation 4.6}$$

Therefore, in **Equation 4.6**, S and W can be calculated; V and V_c can be measured by SEM and surface micro-profilometry. If drawing a linear fit based on the data from **Equation 4.6**, k_c and k_s can in principle be calculated by knowing the gradient and intercept.

4.3.8. *Electrochemical corrosion evaluation*

The corrosion of magnesium involves the transfer of electrons, which are released from the oxidation of magnesium atoms and consumed by the reduction of the corrosive species. Thus, corrosion can be regarded as a consequence of the balance of these electrochemical processes. The corrosion properties of nanocomposite coatings on WE43 magnesium alloys were investigated by performing a series of electrochemical

corrosion tests, including open circuit potential (OCP) with time, electrochemical impedance spectroscopy (EIS), and potentiodynamic polarisation scans.

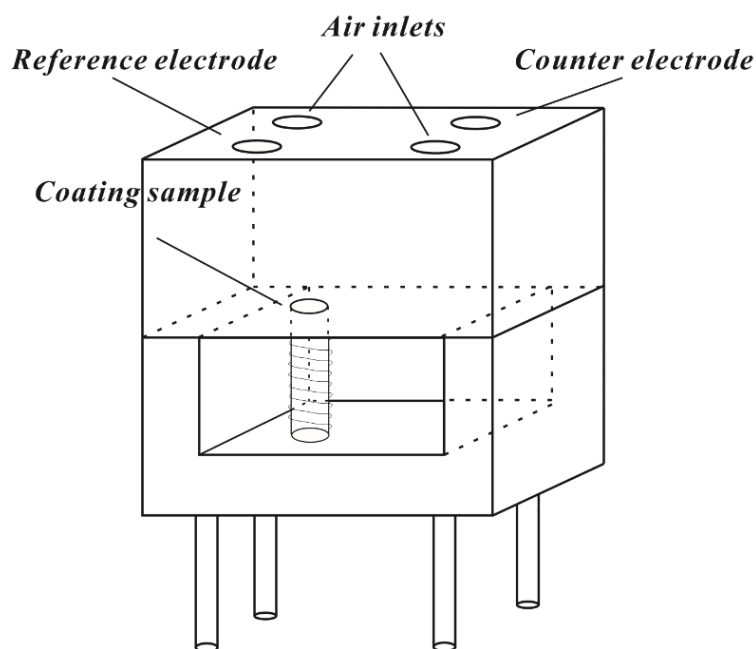


Figure 4.9 A schematic diagram showing the plane three-electrode cell

A standard plain three-electrode cell was used in the test. **Figure 4.9** displays the schematic of the plane three-electrode cell. The holes on the top of the cell indicated the corresponding positions of inserted electrodes and air inlet. The counter electrode was a platinum plate (10 x 25 mm) and the reference electrode was a saturated calomel electrode (SCE) (0.2444 V relative to standard hydrogen electrode (SHE)). The coating sample (*i.e.* working electrode) was clamped to the bottom of the cell with the support of a spring-loaded system. The exposed area of the sample was around 0.423 cm². The air inlets allow air bubbles out; these were produced from the chemical reaction with a 3.5 wt% NaCl solution.

CHAPTER 5: COMPOSITION AND MICROSTRUCTURE OF NOVEL NANOCRYSTALLINE/GLASSY ALCUMOMGZRB PVD COATINGS

This chapter reports on investigations into the composition and microstructure of a novel AlCuMoMgZrB PVD coating layer. The layers were prepared by pulsed direct current closed-field unbalanced magnetron sputtering. Four deposition runs were carried out with substrate negative bias of 50 V, 60 V, 75 V and 100 V. For each deposition run, four Elektron-proprietary WE43 magnesium alloy substrates were placed at fixed intervals along the middle row of the substrate holder (see **Figure 4.1** in Chapter 4). In total, sixteen AlCuMoMgZrB PVD coatings of varying composition were produced for experimental characterisation.

The phase composition of all as-deposited AlCuMoMgZrB PVD coating layers, shown from XRD characterisation, was consistent with the expected amorphous and/or nanocrystalline structures. The applied substrate negative bias was found to have a significant impact on both the elemental composition and the final microstructure of the layers, particularly for those located in the middle positions (*i.e.* P2 and P3). The substrate negative bias was observed to promote crystallisation of the layers between 50 V and 75 V; however, crystallisation appeared to be suppressed when a substrate negative bias of 100 V was applied. The relationship between microstructural evolution, substrate bias, and elemental composition with the energy spectrum of the deposited particles on arrival is examined

The primary aim of the investigation was to establish a solid understanding of these novel coating layers, prior to subsequent mechanical, scratch-adhesion and corrosion property evaluation. After characterisation, the ‘best’ layer (with optimised combination of desired properties) is selected as a ‘coupling’ base layer for PVD coating deposition (nitride ceramic or nitrogen-doped hard metallic) onto Mg-alloy substrates.

5.1. Elemental composition

The elemental compositions of each as-deposited layer were detected using EDX technique. The results are shown in **Table 5.1** below.

Layer Designations	Elemental composition (at.%)					
	Al	Mg	Cu	Mo	Zr	B
P1-50	68.5	13.7	5.5	4.8	2.8	4.7
P2-50	63.3	8.6	10.7	8.7	4.5	4.2
P3-50	45.9	2.5	23.4	18.2	6.9	3.0
P4-50	26.4	2.0	30.0	30.6	8.2	2.8
P1-60	71.0	11.3	7.2	4.5	2.1	3.8
P2-60	66.8	6.6	11.7	8.2	3.5	3.2
P3-60	36.3	2.0	27.7	23.2	8.1	2.8
P4-60	18.4	1.8	31.3	36.6	9.6	2.3
P1-75	72.4	9.9	7.3	4.9	2.6	2.8
P2-75	66.0	6.2	12.0	9.1	4.3	2.4
P3-75	32.6	1.9	26.2	27.7	9.5	2.2
P4-75	18.4	1.3	28.1	39.4	10.9	1.9
P1-100	77.8	8.0	6.6	3.6	1.9	2.1
P2-100	71.6	3.9	11.5	7.6	3.5	1.9
P3-100	22.5	1.7	27.0	37.4	9.9	1.4
P4-100	15.4	1.0	28.7	42.8	10.9	1.2

Table 5.1 Elemental compositions of as-deposited AlCuMoMgZrB layers

As can be seen from **Table 5.1**, in each run, the deposition position between the two composite targets significantly influences the elemental composition of each layer. In particular, the compositional difference between P2 and P3 was found to be unexpectedly large, although all four substrates were placed at similar fixed intervals along the middle row of the sample holder (see **Figure 4.1** in Chapter 4).

5.1.1. Effect of increasing substrate negative bias on elemental composition

The applied substrate negative bias voltages were also found to have a significant influence on the elemental composition as shown in **Figure 5.1**.

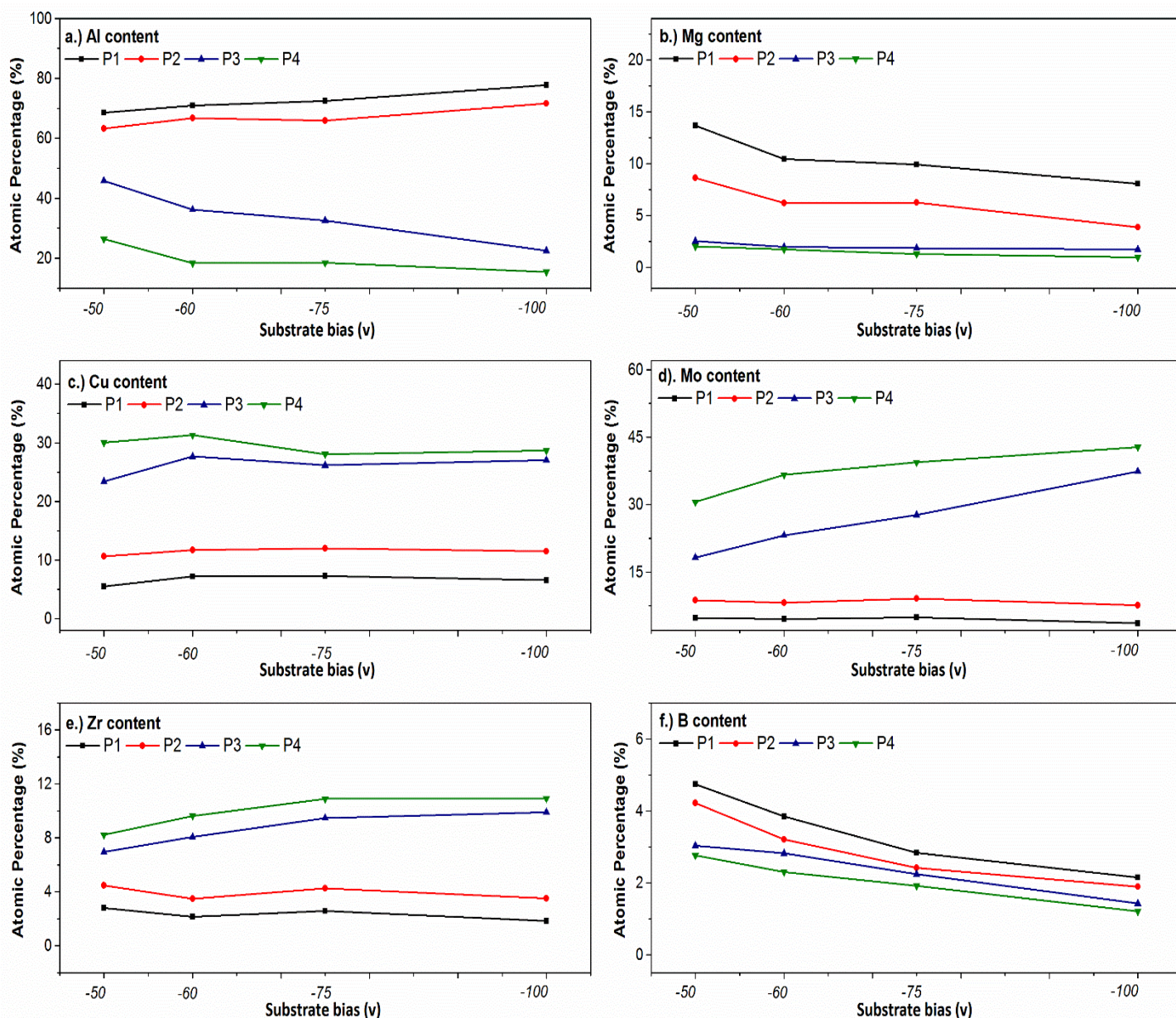


Figure 5.1 Elemental compositions varying with substrate negative bias; (a) Al; (b) Mg; (c) Mo; (d) Cu; (e) Zr; (f) B

The total composition of other elements (e.g. oxygen, carbon and iron) was detected below 1at%.

Therefore, their compositions were eliminated

In **Figure 5.1(a)**, the Al content of the samples deposited at P1 and P2 positions can be seen to increase with substrate negative bias. Conversely, Al content in P3 and P4 layers was found to decrease with increasing substrate negative bias, especially when a substrate negative bias of 50 V or 60 V was applied.

Figure 5.1(b) shows a descending trend of Mg content in P1 and P2 layers, particularly when a substrate negative bias of 50 V or 60 V was applied. In addition, Mg content in P3 and P4 layers barely changed as the substrate negative bias was varied.

With increasing distance away from the AlMg/AlB two-piece composite target, Cu and Mo were observed as the primary elements in P3 and P4 layers instead of aluminium. In **Figure 5.1(c)**, the Cu content in P3 and P4 layers was found to increase when the substrate negative bias was increased from 50 V to 60 V. A moderate reduction of Cu content was observed as the negative bias was further increased to 75 V, but no effect on Cu content of increasing the negative bias further to 100 V was observed. Cu content in P1 and P2 layers could be considered to remain constant, regardless of the substrate negative bias applied.

The Mo content in P3 and P4 layers demonstrated a considerable increase with substrate negative bias. On the other hand, this effect was not observed in P1 and P2 layers (see **Figure 5.1(d)**). The concentration of Zr followed the same trend as that of Mo (see **Figure 5.1(e)**)

In **Figure 5.1(f)**, the B content in all layers showed a considerable reduction with increasing substrate negative bias. The decrease in magnitude of B content in P1 and P2 layers appeared to be larger than that in P3 and P4 layers

5.1.2. Discussion of influence of substrate negative bias on elemental composition

As displayed in **Figure 5.1**, the large difference of elemental composition between P2 and P3 layers could be attributed to the large distance between these samples (see **Figure 4.1**). Moreover, the compositional behaviours of all elements in each deposition position with respect to applied substrate negative bias could be divided into two sub-groups: P1/P2 and P3/P4. In each sub-group, the layers possessed not only similar stoichiometries, but also similar performance under the influence of increasing substrate negative bias

5.1.2.1. Resputtering effect

Although the compositional difference between P2-50 and P3-50 layers was initially large (particularly for Al, Cu, Mo and Zr), the discrepancy was found to be amplified with increasing substrate negative bias. This behaviour may be attributed to preferential resputtering effects. During film growth, the lighter elements (*i.e.* B, Mg and perhaps Al) might be resputtered by the arriving heavier elements (*i.e.* Zr, Mo, Cu).

Such resputtering effects would be expected to become more pronounced at higher substrate negative bias. This is because (with other parameters remaining constant) a higher substrate negative bias will tend to increase the average energy of the arriving ions, resulting in enhanced ion bombardment and increased sputter yield per arriving ion. Additionally, the layers deposited close to the target containing heavy elements (*i.e.* P3 and P4 layers) are more prone to be influenced by the resputtering effect. The hypothesis corresponds to a decreasing Al content (and increasing Zr, Mo

and Cu content) in P3 and P4 layers, with increasing substrate negative bias (although the increasing magnitude of Cu content was relatively minor, compared with Zr and Mo).

Moreover, during the growth of P1 and P2 layers, B and Mg were expected to be extensively resputtered by Al. Al possesses not only the largest concentration in P1 and P2 layers, but also the highest atomic mass in the AlB/AlMg composite target that is close to the deposition position of P1 and P2 layers. This could account for the decreasing B and Mg content and the increasing Al content in P1 and P2 layers as substrate negative bias increased.

5.1.2.2. *Sputter yield*

Although the resputtering effect might lead to the reduction of Mg and B due to their low atomic mass, their concentrations are still found to be abnormally low. As the AlMg/AlB target segments contain 50 wt.% Al and 50 wt.% Mg, and 90 wt.% Al and 10 wt.% B, respectively, this corresponds to 47 at.% Al and 53 at.% Mg, and 79 at.% Al and 21 at.% B. This meant that Mg and B compositions in the two-piece composite target combination are approximate 26.5 at.% and 10.5 at.%, respectively. However, this is much higher than the layer with the largest Mg and B concentrations (*i.e.* P1-50) detected in EDX, corresponding to only 13.7 at.% and 4.7 at.%, respectively (*i.e.* roughly one half of the ‘expected’ content).

To explore the reason for this, **Table 5.2** exhibits the sputter yield of each element and the corresponding power and voltage.

Elements	Applied powers (corresponding voltages)	Sputter yield*
Al	600 W (330 V)	0.7
B	600 W (330 V)	0.2
Mg	600 W (330 V)	1.6
Zr	400 W (290 V)	0.3
Mo	400 W (290 V)	0.3
Cu	400 W (290 V)	1.3

Table 5.2 Sputter yield of each element

** sputter yields are estimated according to the data given by the UK National Physical Laboratory [149]*

As seen from **Table 5.2**, the lowest sputter yield of B may account for its lower concentration. However, when taking into account Mg which possesses the highest sputter yield, the yield from B should be lower than the EDX results as both elements will be influenced by resputtering effect. This may be explained by a boride-forming effect, where B may react with other boride-forming elements (*e.g.* Al and Zr) during the deposition. This can reduce the risk of resputtering and collision, and thus increase B concentration to a higher level than expected. Moreover, although Zr and Mo possess similar sputter yields, the closer distance between the Mo segment and the substrate led to a higher concentration of Mo compared to Zr (*i.e.* Mo segment and substrates were both placed in the middle of the target and the substrate holder respectively, see **Figure 4.3** in Chapter 4).

5.2. Phase composition

The phase composition of each layer was characterised using glancing angle X-ray diffraction analysis (GAXRD), the results of which are shown in **Figure 5.3**. In addition, a diffraction pattern of the WE43 substrate was also obtained from θ - 2θ scanning mode, for comparison to the as-deposited AlCuMoMgZrB layers

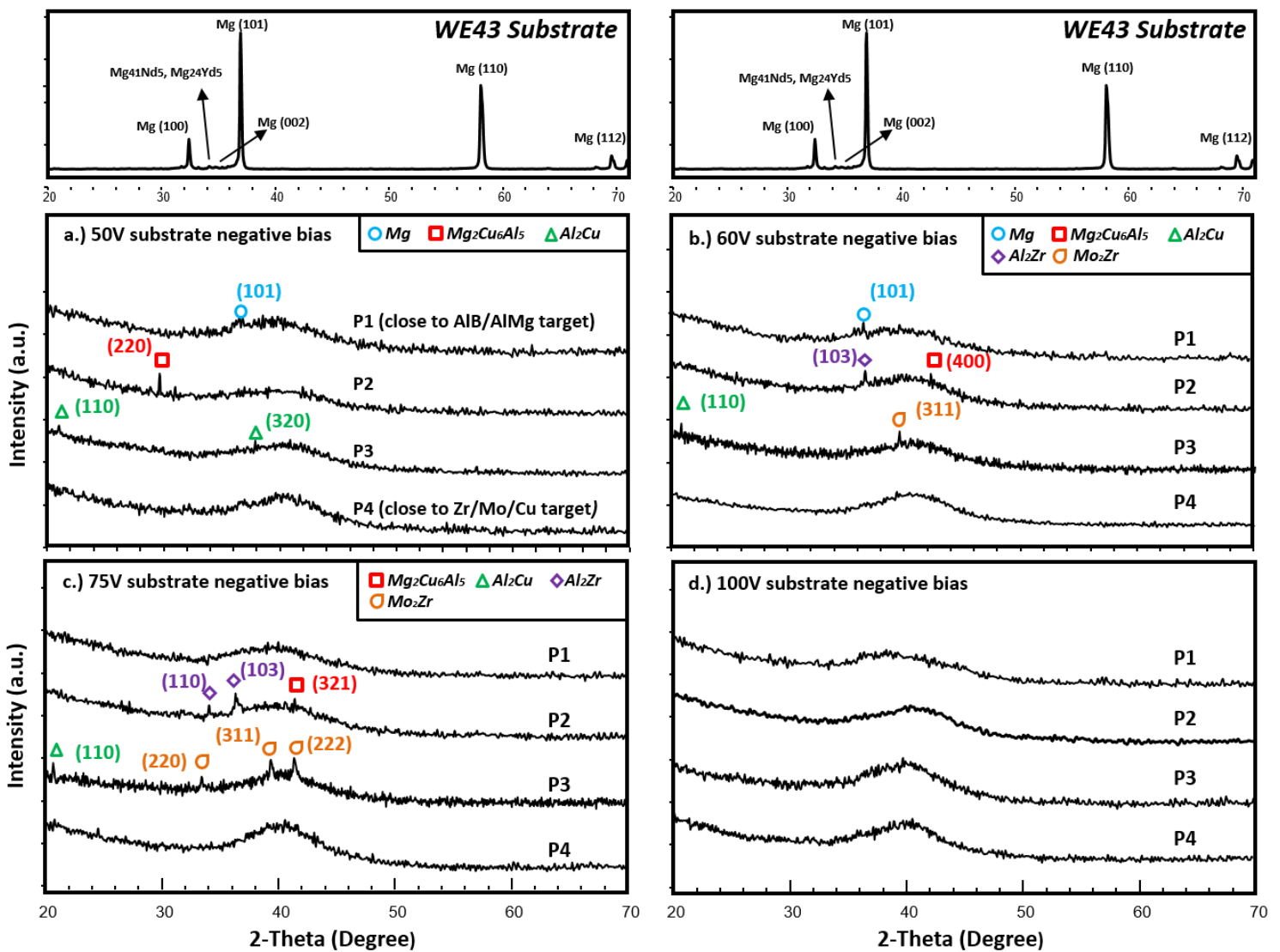


Figure 5.3 XRD patterns of WE43 substrate and AlCuMoMgZrB layers deposited at: (a) 50 V; (b) 60 V; (c) 75 V; (d) 100 V substrate negative bias

In **Figure 5.3**, all diffraction patterns of AlCuMoMgZrB layers exhibited a primary broad reflection approximately between 38° to 46° of 2-theta. This indicates the presence of a large proportion of amorphous phase in the layers. Furthermore, small characteristic peaks were found to appear in some patterns, suggesting the existence of a small number of intermetallic nanocrystallites. It is difficult to precisely distinguish the presence of either ultra-fine grain sizes (in the order of a few to a few tens of nanometres), or of amorphous phase constituents, or (most probably) both.

5.2.1. Discussion of the formation of nanocrystalline phases

Although extensive amorphisation is observed in each layer in terms of broad reflection, several sharp crystalline peaks still are still found (*e.g.* Mg, $\text{Mg}_2\text{Cu}_6\text{Al}_5$ and Al_2Cu).

5.2.1.1. Intermetallic characteristic peaks

As the substrate negative bias increases from 50 V to 75 V, more characteristic crystalline peaks appear in P2 and P3 layers, which are characterised as intermetallic phases: $\text{Mg}_2\text{Cu}_6\text{Al}_5$, Al_2Zr , Al_2Cu and Mo_2Zr . This is indicative of a promotion of crystallisation within the intermediate substrate bias range. Moreover, the evolution of texture indicates a significant growth competition among the phases (*e.g.* the Miller index of (220) $\text{Mg}_2\text{Cu}_6\text{Al}_5$ phase evolves to (400) and (321) at higher substrate negative bias). In contrast, P1 and P4 layers are less affected and retain highly amorphous characteristics across the chosen substrate bias range.

When a substrate negative bias of 100 V is applied, all patterns show a broad and smooth XRD profile, indicating a significant proportion of amorphous phase. It can be concluded that the crystallisation of the intermetallic phases is promoted in the negative bias range between 50 V and 75 V, but suppressed at the substrate negative bias of 100 V.

5.2.1.2. *Mg characteristic peak*

As seen from **Figure 5.3 (a) and (b)**, a small Mg(101) peak appears in the XRD patterns of both P1-50 and P1-60 layers. In comparison to the XRD pattern of WE43 alloy, the characteristic peak is expected to be interference from the substrate. This indicates that the Cu-K α X-rays are able to penetrate through the layer and reach the substrate. The reason perhaps is that P1-50 and P1-60 layers contained a large proportion of light elements (*i.e.* B, Mg, and Al) although the glancing angle used was as low (only 1° in the present study).

5.2.2. *Discussion of the formation of amorphous phase*

As seen from **Figure 5.3**, the broad reflection appearing in each layer is indicative of the presence of a large proportions of amorphous phase. This is caused by the selected different atomic sizes and/or preferred crystallographic structures of Al (small/fcc), Cu (medium/fcc), Mo (medium/bcc), Mg (medium/hcp) and Zr (large/hcp). The mixture of these elements, together with B that is small enough to locate in interstitial sites, considerably frustrates the crystallisation process.

5.2.2.1. *Atomic collision cascade model*

The layers deposited at a substrate negative bias of 100 V exhibit little to no characteristic crystalline peaks, indicating the highest possibility to have an amorphous microstructure.

This could be explained by the atomic collision cascade model [150, 151]. This model elucidates that, when an energetic ion bombards the surface and penetrates to a certain depth, it collides with the atoms of the near-surface. If the energy delivered from energetic ions exceeds a certain threshold value, the substrate atom will be scattered from its own lattice site, leaving a vacancy. If the energy of the scattered atom is still much greater than the threshold energy, it can cause further collisions. This gives rise to the formation of a distorted atom network, and thereby exhibiting highly amorphous microstructures such as those observed in the XRD patterns.

5.2.2.2. *Compositional difference*

Another postulation is that the formation of amorphous microstructure correlates with the elemental composition. The amorphous microstructure may be formed in the layers containing the elements from either of the two composite targets.

For instance, P1 layers show a highly amorphous microstructure because their deposition positions were close to AlMg/AlB composite target. As a result, P1 layers are rich in Al with a small addition of Zr, Mo and Cu. This leads to the formation of amorphous microstructure. Similarly, the amorphous characteristic of P4 layers is probably attributed to their stoichiometry composed mainly of Mo and Cu, while depleted in Al, Mg and B.

This argument might explain the highly amorphous phase constitution observed in all layers deposited at 100 V substrate negative bias. This is because these layers exhibited the largest compositional difference between Al and the elements Zr, Mo and Cu as compared with their counterparts deposited at a lower substrate negative bias (see **Figure 5.1**).

5.2.2.3. Elemental selection

As mentioned in Chapter 4, different preferred crystallographic structures and atomic sizes (above ~12% among the three main constituent elements) tend to promote the formation of bulk metallic glass (BMG) [122]. In each layer group (P1, P2, P3 and P4), three most abundant elements, together with their crystallographic structures and atomic radii, are listed in **Table 5.3**. The table is used to illustrate the relationship between elemental selection and formed microstructures.

Group	Three most abundant elements with crystallographic structure and atomic radius (pm)	The fourth most abundant element with crystallographic structure and atomic radius (pm)
P1	Al (<i>fcc</i> ; 125); Mg (<i>hcp</i> ; 150); Cu (<i>fcc</i> , 135)	Mo (<i>bcc</i> , 145); B* (<i>rhombohedral</i> ; 87)
P2	Al (<i>fcc</i> ; 125); Cu (<i>fcc</i> , 135); Mo (<i>bcc</i> , 145)	Mg (<i>hcp</i> ; 150)
P3	Al (<i>fcc</i> ; 125); Cu (<i>fcc</i> , 135); Mo (<i>bcc</i> , 145)	Zr (<i>hcp</i> ; 160)
P4	Mo (<i>bcc</i> , 145); Cu (<i>fcc</i> , 135); Al (<i>fcc</i> ; 125)	Zr (<i>hcp</i> ; 160)

*Boron is the fifth most abundant element in P1 layers but is comparable in elemental content to Cu and Mo

Table 5.3 Atomic information of main constituent elements in P1-P4 layers

In each layer group, the three most abundant elements can be considered to form a ternary system, and addition of the fourth element is regarded as

an addition to the ternary system which contributes to the glass forming ability of the layer.

Generally, in BMGs, the solvent element not only has the largest concentration, but also has the largest atomic size (preferentially with an atomic radius of 150pm or more) [152]. Thus, amorphisation of Al-based alloys is expected to be more difficult than alloys based on systems with larger atomic radii in the primary elements (*e.g.* Zr, Ca and rare earth elements).

However, the results of the XRD patterns suggest extensive amorphisation of the Al-rich layers (see **Figure 5.3**). This can be attributed to a rapid cooling rate of the PVD process and low thickness (which is below that of the critical thickness for glass formation). Therefore, the criteria used for the development of BMGs may not be completely suitable to produce a thin film metallic glass via PVD processing. Hence, the introduction of elements with different crystallographic structures and increasing difference in atomic size is believed to be beneficial to enhance the glass-forming ability of the coating. This design criterion has recently been used to produce Al-based multielement PVD amorphous coatings for wear and corrosion protection of steels [153].

The components of the Al-Mg-Cu ternary system in P1 layers contains two different crystallographic structures: fcc and hcp. The concentration of Cu in the system is roughly similar to that of Mo (which is the fourth abundant element and possesses bcc structure). As **Table 5.3** showed, Mo serves as an addition to the ternary system and further improves its glass forming ability by introducing another crystallographic structure (*i.e.* bcc). In addition, B content in the P1 layers is also similar to Cu and Mo (particularly for layers deposited at low substrate negative bias). The addition of B which has a rhombohedral structure and small atomic radius

(87pm) should significantly promote the formation of amorphous microstructure in P1 layers.

In the P2 layers, the ternary system of Al-Cu-Mo has two different crystallographic structures: fcc and bcc. The atomic radius of the system ranges from 125pm to 145pm. This represents an atomic size difference exceeding 12%. The addition of Mg introduces another crystallographic structure (hcp), while expanding the atomic radius range to 125-150pm.

Considering the Al-Cu-Mo ternary system in P3 layers, the addition of Zr is somewhat different with P1 and P2 layers. This is because, although Zr is the fourth most abundant element, the concentration of Zr is less than half of the third most abundant element in the system (Mo). Therefore, the effect of Zr addition to the Al-Cu-Mo ternary system is limited.

In comparison, the improved potential of glass forming ability by adding Zr to the Mo-Cu-Al ternary system in P4 layers appears to be promising. This is because the concentration of Zr is comparable to the third most abundant element (Al).

From the above discussions, it can be concluded that, when comparing P1-P4 layers, the glass forming ability of P3 layers is expected to be the lowest. Although distinguishing the best glass former amongst the remaining three layers is difficult, P4 layers are expected to possess a better glass forming ability than P2 layers due to the larger difference in atomic radius (*i.e.* 125-160pm of P4 layers in comparison to the 125-150pm of P2 layers). Although speculative, these arguments seem to be in a good agreement with the results of XRD patterns (see **Figure 5.3**). P3 layers in XRD patterns are observed to present the most characteristic peaks. The XRD patterns of P4 layers appears smoother compared with those of P2 layers. Therefore, P2 and P3 layers tend to possess a strong intermetallic-forming ability. In contrast, P1 and P4 layers tend to possess a strong glass-forming

ability.

5.3. Thickness and morphology

5.3.1. Fracture cross-sections

Fracture cross-sectional morphologies of all the layers were observed by SEM and are shown in **Figure 5.4** below.

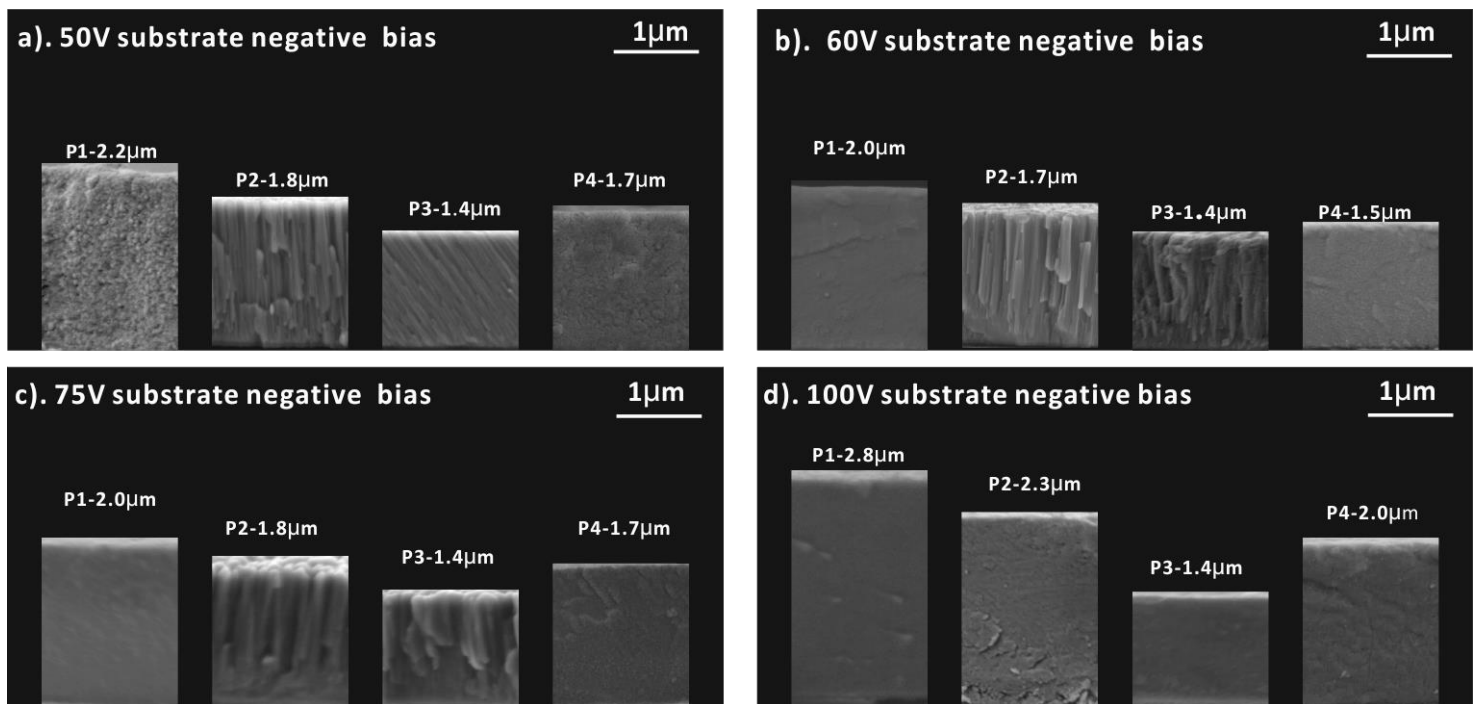


Figure 5.4: Fractured cross-sectional morphologies of AlCuMoMgZrB layers deposited at: (a) 50 V; (b) 60 V; (c) 75 V; (d) 100 V substrate negative bias

The SEM images of the fracture cross-sections in **Figure 5.4** indicate an evolution of coating morphology as a result of changing substrate negative bias especially in the P2 and P3 layers.

As seen from **Figure 5.4 (a)**, some voids are found in the fracture cross-sections of P1-50 and P4-50 layers. The fracture cross-sections of P2-50

and P3-50 layers exhibit a columnar morphology in which the fine columns penetrate from bottom to top through the thickness. The P3-50 layer exhibits a tilted columnar appearance caused by shadowing effects. This is characteristic of a Zone I structure, according to the Thornton model [154, 155]. The formation of Zone I structure correlates with a low homologous temperature (T_s/T_m ; T_s and T_m represent deposition temperature and melting point, respectively) at which adatom diffusion is negligible and columns preserved the random orientation of the nuclei. Hence, an underdense structure is expected to form [156, 157]. This indicates possibly insufficient ion bombardment effect at the substrate negative bias of 50 V.

When a substrate negative bias of 60 V or 75 V is applied, a densification of the fracture cross-sectional morphology is found in P1-60, P4-60, P1-75 and P4-75 layers (see **Figure 5.4(b) and (c)**). A competitive growth is observed in the layers which is characterised by columns near the top surface, V-shape grains in the next thickness range and dense microstructure at the near-substrate area. The larger boundary between the bottom dense texture and the middle V-shape grains is found to rise from 60 V to 75 V negative bias. This microstructure results from the competitive growth of differently oriented neighbouring crystals, suggesting a significant surface self-diffusion and a wide distribution of grain sizes [158]. The column width near the top surface is found to increase from 60 V to 75 V negative bias.

When the substrate negative bias is increased further to 100 V (see **Figure 5.4(d)**), all layers exhibit a homogeneous and dense morphology. The absence of columns can be explained by the atomic collision cascade model [150, 151] which was discussed previously in section 5.2.2.1.

The evolution of fracture cross-sectional morphology is in good agreement

with the observations in XRD patterns. A microstructural evolution is promoted in the negative bias range between 50 V and 75 V, but suppressed at the substrate negative bias of 100 V. The microstructure of P1 and P4 layers is less affected by the increasing substrate negative bias compared to that of P1 and P3 layers.

Moreover, a microstructural transition with increasing substrate negative bias has also been observed in other studies of nanocomposite coatings [159, 160]. These studies revealed a clear microstructural transition from columnar to glassy morphology and suggested a correlation to ion energy distributions on the substrate surface during deposition. Thereby, a discussion of the ion energy distributions in the present research will be carried out later, in section 5.3.4.

5.3.2. Layer thickness

In each run, the layer thicknesses are observed to be considerably different. In each deposition run, the thickness is sorted by descending order of P1>P2>P4>P3. In general, the layer thickness of each group increases with increasing substrate negative bias.

The variation in layer thickness can be explained by target element sputter yields, homologous temperatures of involved elements and/or resputtering effects. Combined with data from **Table 5.2** which shows the sputter yields of each element at corresponding voltages (*i.e.* Al, Mg and B: 330V; Zr, Cu and Mo:290V), **Table 5.4** below is provided to clarify the factors that influence the layer thickness.

Elements	Sputter yield	T _m °C (K)	Relative atomic mass
Mg	1.6	651 (924)	24.31
Al	0.7	660 (933)	26.98
Cu	1.3	1083 (1356)	63.55
Zr	0.3	1852 (2125)	91.22
B	0.2	2076 (2349)	10.81
Mo	0.3	2610 (2883)	95.94

Table 5.4 Sputter yield, melting point and relative atomic mass of each element

As P1 layers are rich in Al and Mg both of which possess low melting points, their homologous temperature is relatively higher compared to

other layers (although the melting point of B is very high, the content of B is not comparable to those of Al and Mg, see **Table 5.1**). Moreover, the sputter yields of Al and Mg are relatively high, indicating a large number of Al and Mg atoms arriving to P1 layer surface during the deposition. As a result, layer growth is promoted and thus, the thickness of P1 layers is the highest.

Similarly, as the deposition position of P2 layers is the second closest to the AlMg/AlB composite target, P2 layers is expected to possess a considerable thickness.

Although the high melting points of Zr, Mo and -to some extent- Cu (and associated low homologous temperatures) constrain the growth of P4 layers, the sputter yield of Cu is considerably higher than the other two elements. Moreover, as these elements all possess relatively high atomic mass, the resputtering effect plays an important role in influencing the deposition of P3 layers. The layer growth of P3 samples is therefore limited. Thus, the thickness of P4 layers is higher than that of P3 layers.

The increased layer thickness of each group with increasing substrate bias can be interpreted from the point of view of the homologous temperature. The deposition temperature (T_s) is expected to be somewhat increased (all other condition remaining approximately constant) when a higher substrate bias is applied. Hence, a higher homologous temperature (T_s/T_m) can be obtained which leads to the promotion of layer growth. The increasing magnitude of thickness is found to be larger in P1 and P2 layers which is in agreement with their higher homologous temperature than P3 and P4 layers, as discussed above.

5.3.3. Surface morphology

The surface morphologies of all AlCuMoMgZrB layers were also observed by SEM and are shown at high magnification in **Figure 5.5**.

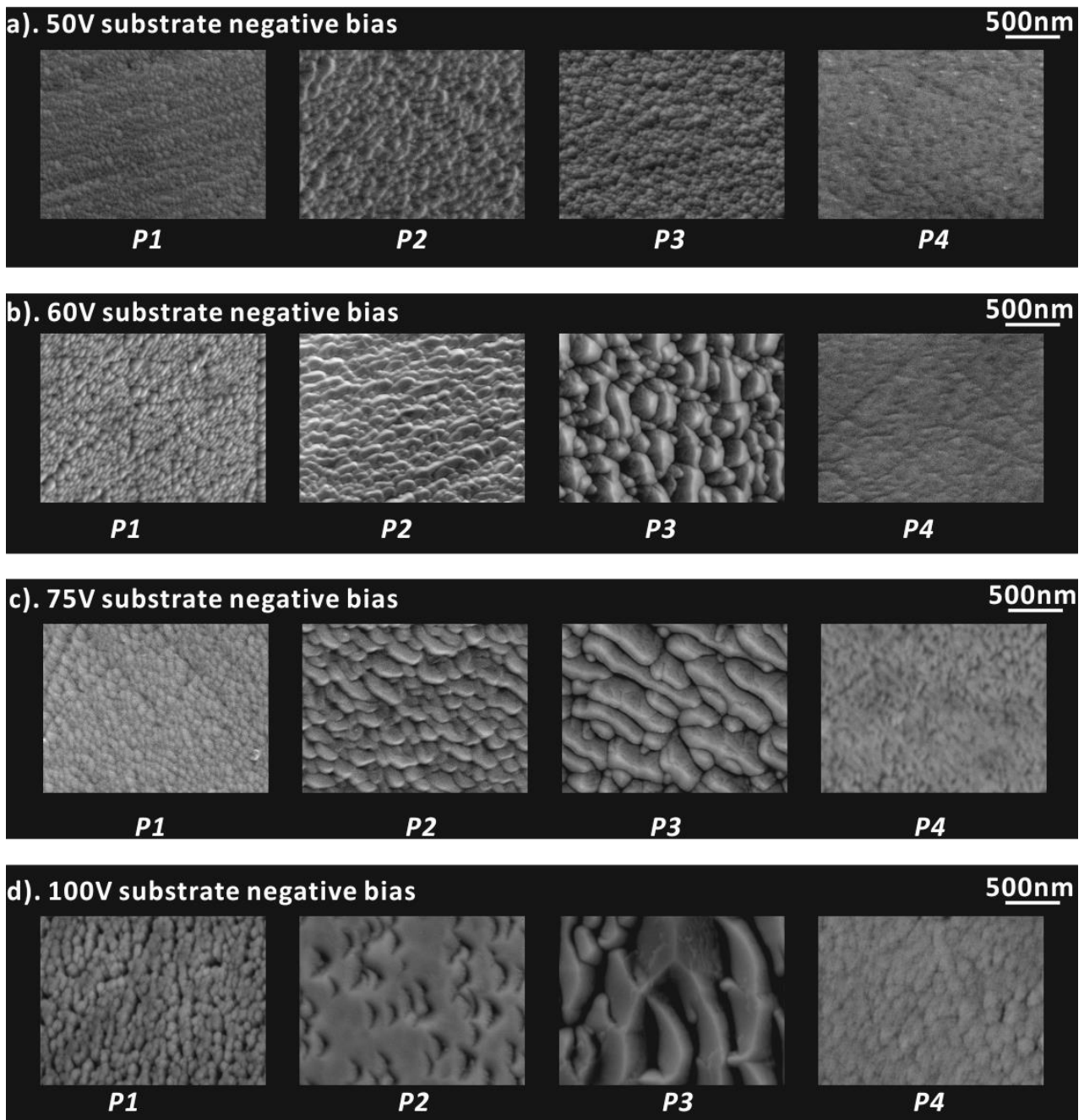


Figure 5.5 Surface morphologies of AlCuMoMgZrB layers deposited at: (a) 50 V; (b) 60 V; (c) 75 V; (d) 100 V substrate negative bias

The surface morphologies observed in **Figure 5.5** can be classified into following five categories as listed in **Table 5.5**:

Morphological Category	Corresponding Layer
Smooth	P4-50, P4-60, P4-75 and P4-100
Bump-shaped	P1-50, P1-60, P1-75, P1-100, P2-50 and P3-50
Wave-shaped	P2-60 and P2-75
Combined wave-bump shaped	P3-60 and P3-75
Crescent-shaped	P2-100 and P3-100

Table 5.5 Surface morphological categories of AlCuMoMgZrB layers

In **Figure 5.5**, all P1 and P4 layers show bump-shaped and smooth morphologies respectively, at all applied substrate negative bias conditions. Both P2-50 and P3-50 layers initially exhibit a bump-shaped morphology. As the substrate negative bias increases, P2 and P3 layers show wave-shaped and combined wave-bump morphologies, respectively, between the substrate negative bias of 60 V and 75 V. When a substrate negative bias of 100 V is applied, a crescent-shaped morphology is found in P2-100 and P3-100 layers. It should be noticed that the size of crescent-shaped features of the P3-100 layer is significantly larger than those of the P2-100 layer.

The bump-shaped surface morphology observed in P2-50 and P3-50 layers correlates with their columnar fracture morphology seen in cross-section. When a substrate negative biases of 60 V or 75 V is applied, the columnar growth is observed in both wave-shaped and combined wave-bump surface morphologies. The increase in columnar size with substrate negative bias can be interpreted as a consequence of higher adatom mobility induced by

higher intensity ion bombardment [161]. In particular, the combined wave-bump morphology of P3-60 and P3-75 layers (in terms of small bumps surrounded by larger wave-shaped columns) reveals a strong competitive growth.

The combined wave-bump morphology can be regarded as an evolutionary consequence of bump-shaped and wave-shaped morphologies. The columns in the bump-shaped and wave-shaped morphologies are subject to competitive growth and finally evolve into columns with different sizes. This seems to be in agreement with the analysis of XRD patterns. The crystallisation is promoted from the substrate negative bias between 50 V and 75 V.

Although all P1 layers are found to show the bump-shaped morphology, P1-100 layer exhibits columns with flat caps, rather than the ‘arched’ caps observed in the equivalent coatings deposited at lower substrate negative bias. This can be considered to be as a result of energetic ion bombardment at high substrate negative bias, in which the protruding topographical textures are rapidly re-sputtered and then produce flat caps. This is indicative of irradiation damage by excess heat generated during deposition. The arriving energetic particles (*i.e.* ions and/or neutral atoms with high thermal energy) participate in collision cascades, which dissipate their energy to the layer surface and yield a thermalisation stage. Excessive ion bombardment has been found to produce many defects to roughen the layer surface [162, 163]. The speculation of irradiation damage may explain the crescent-shaped features observed in P2-100 and P3-100 layers.

By combining the results of XRD patterns, fracture cross-sections and surface morphologies, a more comprehensive understanding about the microstructural evolution can be obtained. A microstructural evolution is promoted in the negative bias range between 50 V and 75 V, but suppressed

at the substrate negative bias of 100 V. The microstructures P1 and P4 layers are less affected by the increasing substrate negative bias compared those of P2 and P3 layers. The substrate negative bias associated with the energetic bombardment (from ions and neutrals) should have the most influence on the microstructure of P3 layers. This can be seen from that the tilted fracture morphology of P3-50 layer (indicating insufficient ion bombardment) that evolves to the most extensive crescent-shaped surface morphology (indicating irradiation damage by excess energetic bombardment). Considering the consistent smooth surface morphology of P4 layers, the increasing magnitude of the energetic bombardment with the substrate negative bias should be in the sequence of P3>P2>P1>P4.

5.3.4. Discussion of the ion energy distribution during deposition

As discussed previously, a speculation about the energetic bombardment during the layer growth has been proposed. The bombardments can be investigated from the standpoint of the arriving ion energy spectrum at each applied substrate negative bias.

5.3.4.1. L/λ ratio

Many studies of ion energy spectra in vacuum plasma processing have pointed out the importance of L/λ ratio, where L is the cathode fall distance and λ is the mean free path for charge exchange collision [164-166]. A smaller ratio indicates less energy loss and ensures bombardments with ions of sufficient energy to provide the necessary coating growth conditions. The ratio critically influences the distribution of energies for ions arriving at the substrate surface.

The value of L can be evaluated by the studies of Chapman [167] using the derived free-fall version of the Child-Langmuir equation:

$$L = \frac{2}{3} \left(\frac{\epsilon_0}{J} \right)^{\frac{1}{2}} \left(\frac{2q}{m} \right)^{\frac{1}{4}} V^{\frac{3}{4}} \quad \text{Equation 5.1}$$

where ϵ_0 is the permittivity of free space, J is the cathode current density, q is the ionic charge, m is the ion mass and V is the potential drop across cathode fall distance.

The value of λ can be determined by:

$$\lambda = \frac{1}{n\sigma} \quad \text{Equation 5.2}$$

where n is the number density of the gas and σ is the value of the collision cross-section for charge exchange.

ϵ_0 is known as approximately 8.854×10^{-12} F/m and n is expected to be consistent in each run as the vacuum condition of all depositions in this research is the same (i.e. 0.02 mTorr (2.67×10^{-3} Pa) base pressure, 2.0 mTorr (0.267 Pa) deposition pressure and 9 sccm Ar flow rate). Moreover, for most practical systems, σ is considered to be approximately $4 \times 10^{-15} \text{cm}^2$ [166].

5.3.4.2. Ionised argon gas

If the investigation focuses on role of argon ions during the deposition, the values of q and m can be assumed constant in each deposition. Therefore, the evaluation of the ratio of L/λ can be simplified as the ratio of $V^{3/4}/J^{1/2}$ (i.e. derived from **Equation 5.1**), which is directly proportional to L/λ . The potential drop across the cathode fall distance (V) can be considered to be the applied substrate negative bias if assuming the ions originated from the negative glow with an initial energy of zero (i.e. 0 eV). By combining area of sample holder (i.e. 300 mmx130mm) and deposition current (see **Table 4.2** in Chapter 4), the current density (J) can be calculated. The calculated current density and $V^{3/4}/J^{1/2}$ ratio of each deposition run are exhibited in **Table 5.6**.

Substrate negative bias (V)	Current density (A/m ²)	$V^{3/4}/J^{1/2}$ ratio
50	1.795	14.03
60	2.051	15.05
75	2.051	17.80
100	2.564	19.75

Table 5.6 Calculation of $V^{3/4}/J^{1/2}$ ratio

In **Table 5.6**, the ratio of $V^{3/4}/J^{1/2}$ increases with the substrate negative bias, suggesting a larger proportion of energetic ions arriving to the substrate surface at lower substrate negative bias.

Table 5.6 indicates a larger proportion of ions can arrive to the substrate surface when lower substrate negative bias is applied. However, the average ion energy at lower substrate negative bias should also be lower. Thus, it is hard to compare the total ion energy delivery to the surface.

5.3.4.3. *Ionised metal species*

In practice, the ionised species are not only the argon gas, since many metal atoms sputtered from the targets can be ionised by Penning ionisation and deposited onto substrate surfaces. It is an argument with respect to the ionisation mechanism of the metal species. One proposal illustrates that it is purely one of distortion of discharge which produces a separate and improved ionised discharge [166].

In general, the L/λ ratio has been found to reduce when metal ions are introduced to argon glow discharges. The metal ions are considered to suffer less charge transfer collisions than argon in the cathode fall distance (though the dominant charge transfer mechanism is not clear). Therefore metal ion energy distributions would tend to have a larger amount of high energy species than that given by the argon ions [151, 164, 168].

If investigating the effect caused by metal ions (and including B in the research), it is reasonable to establish a separate ionised discharge system. Hence, the values of q and m in from **Equation 5.1** will be different in each deposition run. The concepts of the effective ionic charge (symbol: q' ; unit: e) and the effective atomic mass (symbol: m' ; unit: g) are introduced. The two values can be calculated by knowing the ionic charge of each metal element (symbol: q_i ; the preferential ionic charges: Al^{3+} , Cu^{2+} , Mo^{6+} , Mg^{2+} , Zr^{4+} and B^{3+}), the relative atomic mass of each metal element (symbol: A_i ; the relative atomic mass: 26.98Al; 63.55Cu; 95.95Mo; 24.31Mg; 91.22Zr;

10.81B), the corresponding atomic percentage, % (symbol: χ_i ; see **Table 5.1**) and the Avogadro constant (symbols: L ; $6.022 \times 10^{23} \text{mol}^{-1}$):

$$q' = \sum (q_i \times \chi_i) \quad \text{Equation 5.3}$$

$$m' = \sum \left(\frac{A_i \times \chi_i}{L} \right) \quad \text{Equation 5.4}$$

Similar to the calculation of $V^{3/4}/J^{1/2}$ ratio, the evaluation of L/λ ratio for metal ions can be simplified as the ratio of $V^{3/4}/J^{1/2} \cdot (2q'/m')^{1/4}$, which is still directly proportional to L/λ . The results of the calculation of $V^{3/4}/J^{1/2} \cdot (2q'/m')^{1/4}$ ratios for each layer are shown in **Table 5.7**.

Seen from **Table 5.7**, the ratio of $V^{3/4}/J^{1/2} \cdot (2q'/m')^{1/4}$ shows an overall increase with substrate negative bias. In each deposition, the ratios are decreased from P1 to P4 layers. This implies that a higher proportion of energetic metal ions arrive at the substrate surface at lower substrate negative bias. In addition, a higher proportion of energetic metal ions are likely to be deposited onto substrate surfaces closer to the Zr/Mo/Cu target in each run.

Layer	J (A/m ²)	q' (e)	m' (×10 ⁻²³ g)	$V^{3/4}/J^{1/2} \cdot (2q'/m')^{1/4}$ ratio (×10 ⁶)
P1-50	1.79	2.98	5.48	8.07
P2-50	1.79	3.11	6.46	7.83
P3-50	1.79	3.35	8.63	7.42
P4-50	1.79	3.68	10.60	7.22
P1-60	2.05	2.97	5.50	8.63
P2-60	2.05	3.10	6.39	8.40
P3-60	2.05	3.48	9.60	7.81
P4-60	2.05	3.86	11.53	7.66
P1-75	2.05	3.00	5.64	10.17
P2-75	2.05	3.13	6.62	9.88
P3-75	2.05	3.65	10.19	9.21
P4-75	2.05	4.00	11.81	9.08
P1-100	2.05	2.98	5.40	12.72
P2-100	2.56	3.11	6.35	11.05
P3-100	2.56	3.93	11.41	10.13
P4-100	2.56	4.10	12.25	10.05

Table 5.7: Results of calculated $V^{3/4}/J^{1/2} \cdot (2q'/m')^{1/4}$ ratios

The smallest value of $V^{3/4}/J^{1/2} \cdot (2q'/m')^{1/4}$ for the P4 layer in each run indicates the most intensive ion bombardment. This explains their highly amorphous characteristics in XRD patterns and the dense morphologies observed.

P1 layers are expected to undergo the least ion bombardments if considering the largest $V^{3/4}/J^{1/2} \cdot (2q'/m')^{1/4}$ ratio. This seems inconsistent with the previous XRD and SEM results. As discussed section 5.2.2.3, the amorphous appearance of P1 layers might be ascribed to a wide range of atomic sizes (i.e. 125-150pm) and three different crystallographic structures (i.e. fcc, hcp and bcc). Thus, besides the energetic ion bombardments, the microstructure of the layer also relates to the elemental composition.

The change of $V^{3/4}/J^{1/2} \cdot (2q'/m')^{1/4}$ ratio of P3 layers is observed to be relatively small compared with other layers. Thus, the dramatic microstructural evolution is expected to be mainly attributable to neutrals with high kinetic energy, rather than to ions.

Moreover, first ionisation energy is considered to be an important factor to indicate the ionisation condition of metal species. The first ionisation energy of each element involved in the coating deposition here is shown in **Table 5.8**.

Elements	First ionisation energy kJ/mol (eV)
Al	577.5 (5.99)
Mg	737.7 (7.65)
B	800.6 (8.30)
Zr	640.1 (6.63)
Mo	684.3 (7.09)
Cu	745.5 (7.73)

Table 5.8 First ionisation energy of each element

As seen from **Table 5.8**, all elements show a very low first ionisation potential compared to the applied powers (i.e. 600 W (330V) and 400 W (290V)). This indicates that a large proportion of metal species sputtered from the target will be ionised in the plasma (the ionisation should be significantly higher than that of argon species), but arriving to the substrate surface in terms of energetic neutrals which, in turn, affect the microstructural evolution of the layers.

5.3.4.4. *Limitations of the investigation of ion energy spectra*

The investigation of the ion energy spectrum has some limitations. As seen from **Table 5.7**, the increasing magnitude of the $V^{3/4}/J^{1/2} \cdot (2q'/m')^{1/4}$ ratio (representing the decreasing ion energy spectrum) with substrate negative bias is found to be in the sequence of P1>P2>P4>P3. Combined with the analysis based on the XRD and SEM results, it indicates the increasing magnitude of the energetic bombardment (including the bombardment from both ions and neutrals) is in the sequence of P3>P2>P1>P4. It can be concluded that a large proportion of energetic neutrals are involved in the bombardment during the growth of P3 layers. This is unable to be represented using the evaluation of L/λ ratio.

In addition, the majority of the energetic neutrals are believed to originate from ionised metal species in the plasma. However, the speculation is difficult to investigate and confirm because it is impossible to sputter the metal species from target without the introduction of argon gas using magnetron sputtering technique. Therefore, the increasing pressure only related to the sputtered metal species cannot be measured. However, the investigation is available if using other PVD techniques, such as electron-beam plasma assisted physical vapour deposition (EB-PAPVD). For example, in the operation of EB-PAPVD, the argon gas can be temporarily switched off, while remaining electron gun to evaporate the target. The increasing pressure (i.e. from the evaporated metal species) in the chamber can be measured and the ionisation condition can be analysed using optical spectroscopy.

The assumption of the preferred multiple ionic charges of metal species is not accurate as it is based on the circumstance of the chemical reactions at atmospheric pressure, rather than vacuum plasma conditions of magnetron sputtering, where ions will mainly be singly charges.

Another factor is the inaccuracy when recording the current. The current in each deposition run was recorded by detecting secondary electrons of the whole substrate holder. The accurate current density corresponding to each substrate surface is unknown. Thus, this has a significant influence on the value of J.

5.4. Summary

Sixteen AlCuMoMgZrB layers were successfully produced. The investigation of elemental composition, phase composition and morphologies can be summarised as follows:

Elemental composition

- Both deposition position and applied substrate negative bias significantly impacted on the coating elemental compositions.
- The target sputter yield and substrate resputtering effects for each coating element are important factors which impact on the coating composition and structure.

Phase composition

- All the layers exhibited a large proportion of amorphous phase constituents.
- The substrate negative bias was observed to promote crystallisation of the layers between 50 V and 75 V; however, crystallisation appears to be suppressed when a substrate negative bias of 100 V was applied.

-
- P1 and P4 layers were less affected and retain strongly amorphous characteristics compared with P2 and P3 layers, where intermetallic phase peaks could also be observed.

Thickness and morphology

- The SEM observation of fracture cross-sections and surface morphologies correlates to the XRD analysis, with respect to the applied substrate bias affecting the microstructural evolution.
- Dramatic microstructural evolution with increasing substrate bias was observed in P2 and P3 layers.
- The thickness of the deposited layers is strongly influenced by target element sputter yield, homologous temperatures of involved elements and/or resputtering effects.
- The ion energy spectra of depositing species for each layer was discussed; energetic neutrals appear to play an important role in the microstructural evolution of each layer.

CHAPTER 6: MECHANICAL AND ELECTROCHEMICAL PROPERTIES OF NOVEL NANOCRYSTALLINE/GLASSY ALCUMOMGZRB PVD COATINGS

In the previous chapter, the chemical composition, phase constitution and microstructure of sixteen AlCuMoMgZrB PVD coatings was investigated. It was found that both the depositing position and applied substrate negative bias significantly influenced the elemental composition of the layers. Moreover, all layers exhibited highly amorphous characteristics. Crystallisation in P2 and P3 layers was observed when a substrate negative bias range between 50 V and 75 V was applied, but was suppressed at a high substrate negative bias of 100 V.

In this chapter, investigations into the mechanical and electrochemical corrosion properties of the layers will be carried out. One layer will be selected as the base for subsequent PVD ceramic nitride (or nitrogen-doped hard metallic) coating deposition. Since a hard but compliant layer is beneficial for accommodating both elastic and plastic strains under mechanical or tribological loading, a high ratio of hardness (H) to elastic modulus (E) is desired. In addition, strong adhesion is required to maximise coating lifetime. Finally, a good corrosion resistance of the layer is required to achieve good protection of the underlying WE43 magnesium alloy substrate.

6.1. Mechanical properties

6.1.1. Evaluation of H and E

To evaluate the mechanical properties of the AlCuMoMgZrB layers, nanoindentation was carried out to measure hardness (H) and elastic modulus (E). The results are shown in **Figure 6.1**.

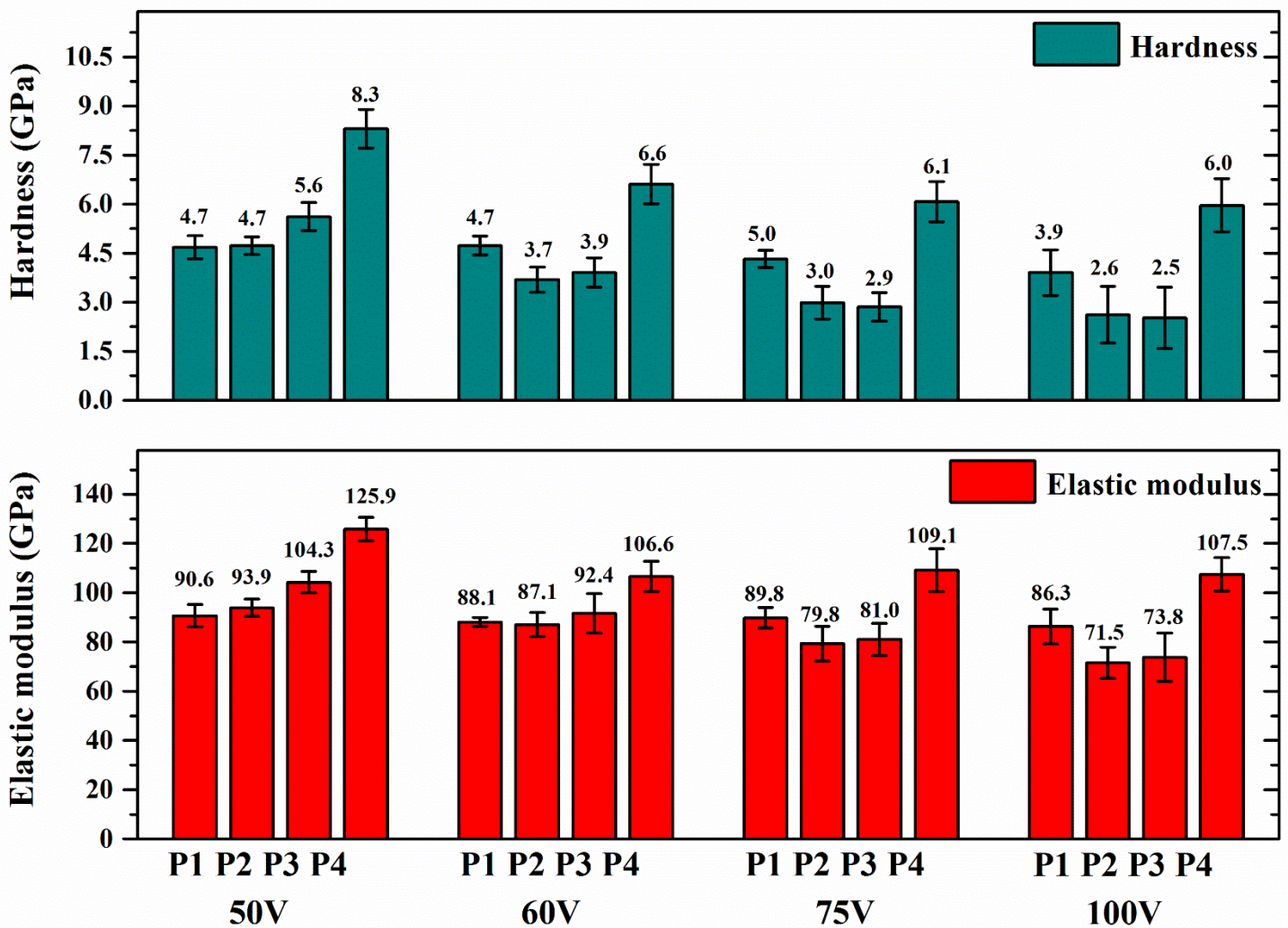


Figure 6.1 Hardness and elastic modulus of AlCuMoMgZrB layers

H and *E* of WE43 substrate were detected as 56.2 GPa and 1.4 GPa, respectively

Compared to WE43 substrate (with H of 56.2 GPa and E of 1.4 GPa), all AlCuMoMgZrB layers showed increasing hardness and elastic modulus. In general, both H and E are observed to decrease with increasing substrate negative bias. The decrease in H for P2 and P3 layers in particular appears to be more significant than that of P1 and P4 layers.

Referring to the results of SEM analysis of the fracture and surface morphology in the previous chapter, the high values of H and E of layers deposited at low substrate negative bias might be as a result of the refinement of columnar grain size. Coatings composed of fine columns that exhibit high H can be explained by the Hall–Petch effect [169]. High measured H can also occur partly due to the residual compressive stress state of the coating. In addition, the formation of open and large columns (possibly with inter-columnar porosity) at a higher substrate bias may contribute to a decrease in measured H and E values. A decrease in resistance to microcrack formation has also been found to be associated with PVD coating columnar growth morphologies [170]. This is in agreement with the observation of large columns and rough crescent-shaped surface morphologies in P2-100 and P3-100 layers (see **Figure 5.5(d)** in Chapter 5).

For each deposition run, the P4 layers exhibited the highest values of H and E. This could be attributed to the deposition position which was near the Zr/Mo/Cu composite target, resulting in a total composition of Cu (E~124 GPa) and Mo (E~330 GPa) in excess of 60 at% being present in each P4 layer (see **Table 5.1** in Chapter 5).

Although the P1 layers contained a large proportion of light elements which was expected to show the lowest H and E values, in comparison, P2 and P3 layers were found to have lower H and E values when a substrate negative bias of 75 V or 100 V was applied. The proposed significant changes in the distribution of energetic particles (both ions and non-

thermalised neutrals) on the surface of P2 and P3 layers could account for the significant reductions in H and E. Although bias-induced ion bombardment during coating growth is thought to increase the surface mobility of adatoms (and hence produce dense microstructure); excessive high-energy bombardment is considered to result in higher residual compressive stress, a coating surface full of defects and rougher coating surface. This corresponds to the observation of crescent-shaped surface morphology of P2-100 and P3-100 layers, which indicates the irradiation damage caused by excessive energetic bombardment. Similar behaviour of decreasing H and E values by applying extremely high substrate negative bias was also reported by Odén *et al.* [170] and Kondo *et al.* [171].

Furthermore, the variation in H and E values were also found to increase with substrate negative bias, particularly in P2 and P3 layers. This is associated with the columnar growth and surface roughening. The smaller variations observed at low substrate negative bias are indicative of reliable deformation behaviour in practical applications.

6.1.2. H/E ratio

The H/E ratio is acknowledged as a potentially an important indicator in revealing coating mechanical performance in practical wear applications. High H values indicate good wear resistance of the coating, while low E values ensure the coating possesses elastic properties close to the underlying substrate. This is particularly beneficial for the surface treatments of soft, compliant substrates (*e.g.* magnesium alloys) to achieve good “engineering toughness” and resilience. **Figure 6.2** shows the H/E ratios of the AlCuMoMgZrB layers

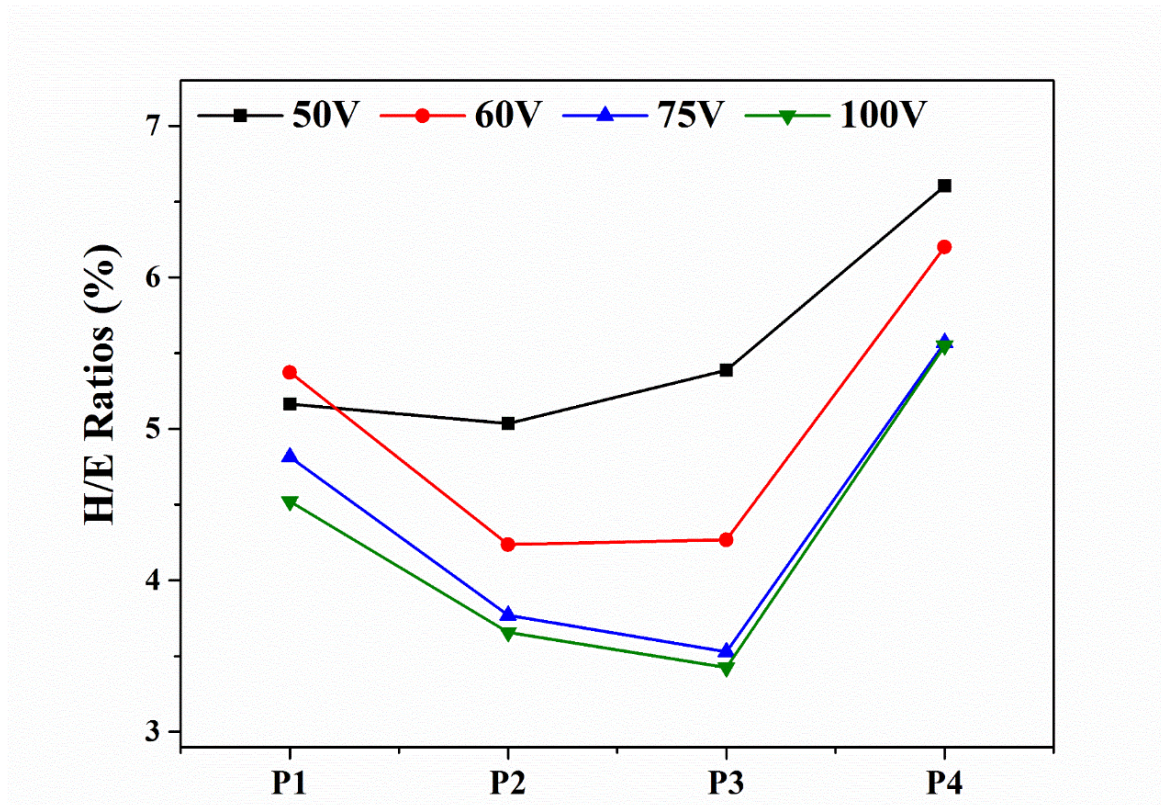


Figure 6.2 H/E ratios of AlCuMoMgZrB layers

H/E ratio of WE43 substrate was ~ 2.49%

As may be seen from **Figure 6.2**, P2 and P3 layers exhibit lower ratios of H/E than those of P1 and P4 layers, for each deposition run. Moreover, the difference is amplified with increasing substrate negative bias. As discussed previously, this may be attributed to a dramatic change in distribution of energetic particles arriving at the substrate during deposition. Although the P4 layers show a slightly higher ratio of H/E than those of the P1 layers, they also possess the highest E values (as high as 125.9 GPa). This indicates an increased risk of elastic strain incoherency with the underlying WE43 substrate ($E \sim 44$ GPa) under high mechanical load. However, despite P2 and P3 layers exhibiting low E (as low as 71.5 GPa), their low H/E ratios may impair tribological properties. It is a controversial factor whether a low elastic modulus or a high H/E ratio would be the more critical parameter in the selection of the ‘best’ AlCuMoMgZrB layer for subsequent PVD ceramic nitride (nitrogen-doped hard metallic) coating trial.

P1 layers show not only low E values, but also moderate H/E ratios. Therefore, P1 layers appear to be likely candidate as the most promising base layer. In particular, P1-60 layer exhibits the highest H/E ratio compared to its counterparts deposited at other substrate negative bias. The E value of P1-60 layer was only 88.1 GPa, which should be adequate to accommodate considerable plastic strain from WE43 substrate. Therefore, based on this analysis, P1-60 layer is expected to be the most suitable base layer for subsequent PVD coating.

6.2. Adhesive strength

To investigate the adhesion strength of all AlCuMoMgZrB coating layers, scratch-adhesion tests were carried out. A good adhesion of the AlCuMoMgZrB layer to the WE43 substrate is important to provide sufficient support for following PVD nanocomposite hard coatings working in harsh service environments (*e.g.* combined wear and corrosion). Due to the soft and compliant nature of the WE43 substrate, with extremely low E (~ 44 GPa), substantial plastic deformation was observed to occur after each scratch. This inevitably gave rise to inferior performance of coatings deposited onto Mg alloy substrates, compared to those deposited onto hard substrates (*e.g.* stainless steel). The results of the scratch-adhesion tests are characterised by the parameters L_{C1} , L_{C2} and L_{C3} . Corresponding definitions and descriptions are as listed in **Table 6.1** below.

<i>Critical loads</i>	<i>Description of failure</i>	<i>Observable characteristics</i>
L_{C1}	First chipping occurrence	The first chipping observed along the edge of scratch track
L_{C2}	Adhesive failure	The first exposure of substrate in the centre of scratch track
L_{C3}	Complete layer spallation	Continuous exposure of the substrate in the scratch track

Table 6.1 Descriptions of failure events and corresponding critical loads in the scratch-adhesion tests

All AlCuMoMgZrB layers formed cracks at the onset of scratching (*i.e.* under an initial load of 5N). Therefore, the parameter L_{C1} , which refers to the load at which the first crack occur, is not considered to be of significance in the tests. Instead, values of L_{C1} in this work is taken to be indicative of the load at which chipping first occurs along the edge of

scratch track (which may still be considered as a type of cohesive failure). However, although significant plastic deformation occurred, all the scratch track widths were measured by surface micro-profilometry to be below 200 μm , which corresponds to the radius of the Rockwell C diamond indenter tip. Once the track width exceeds the diamond tip radius, geometrical similarity is considered to be no longer effective, and thus comparisons should not be carried out [172]. Therefore, comparison of the adhesive strength of the layers is still considered to be appropriate as a criterion in selecting the optimised base layer.

6.2.1. Adhesive strengths of sixteen AlCuMoMgZrB layers

The results of the scratch-adhesion tests are summarised in **Figure 6.3**.

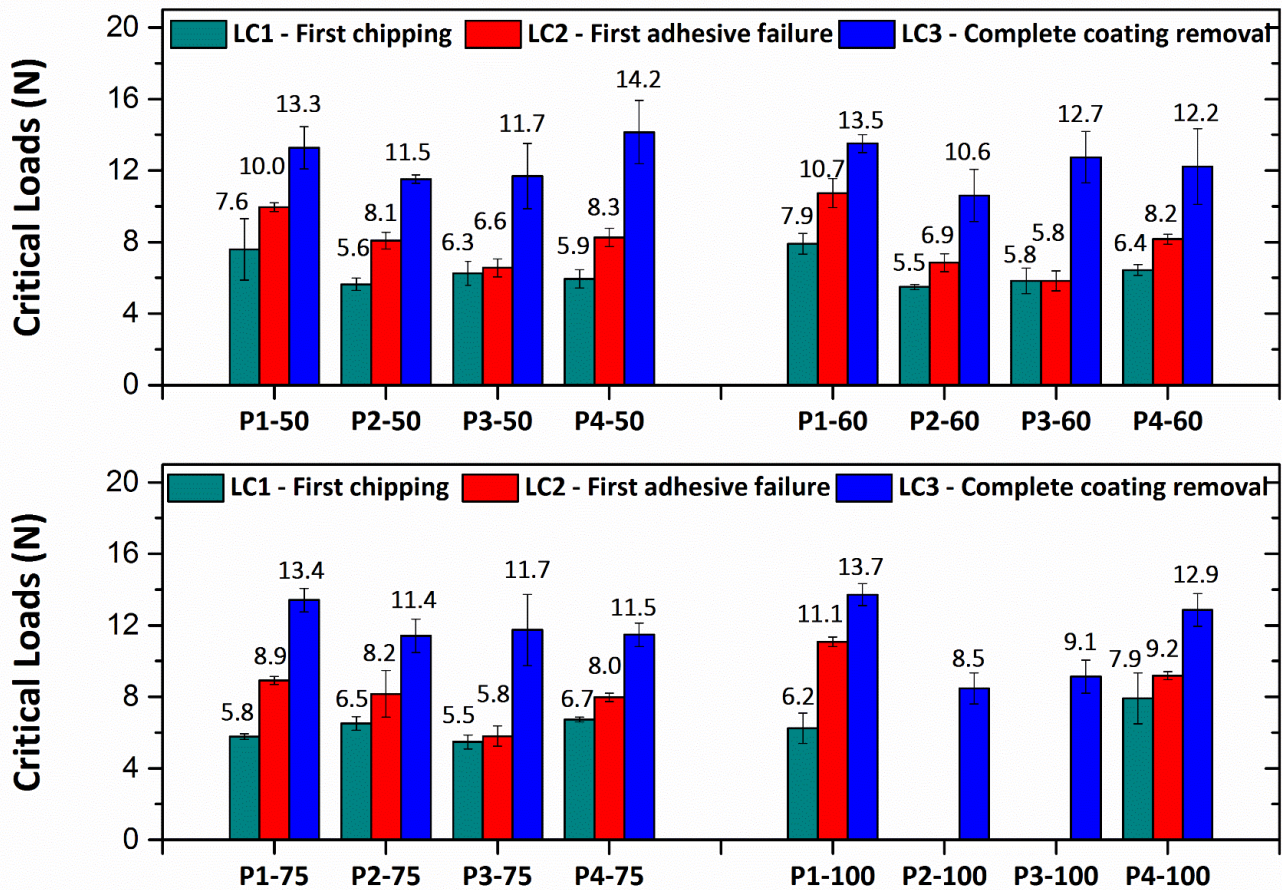


Figure 6.3: Critical loads in scratch-adhesion tests for AlCuMoMgZrB layers

After the scratch-adhesion tests, the critical loads can be determined through observation of the location at which each failure event occurs, through SEM characterisation and converting the corresponding loads.

From the results in **Figure 6.3**, all layers exhibit considerable adhesive strength as they are found to adhere to the substrates for a relatively long period after the first occurrence of adhesive failure (*i.e.* large LC_3 values for

all coatings).

The different thicknesses of the layers may however significantly affect their performance in scratch-adhesion tests. According to a study by Burnett and Rickerby [173], L_{C2} values increased with the thickness; although one argument proposed was that values of L_{C2} should decrease, as the internal energy increases with increasing thickness. To study the possible effect of thickness on measured performance. L_{C2} values should be normalised to a standard of 2 μm . The results are shown in **Figure 6.4**.

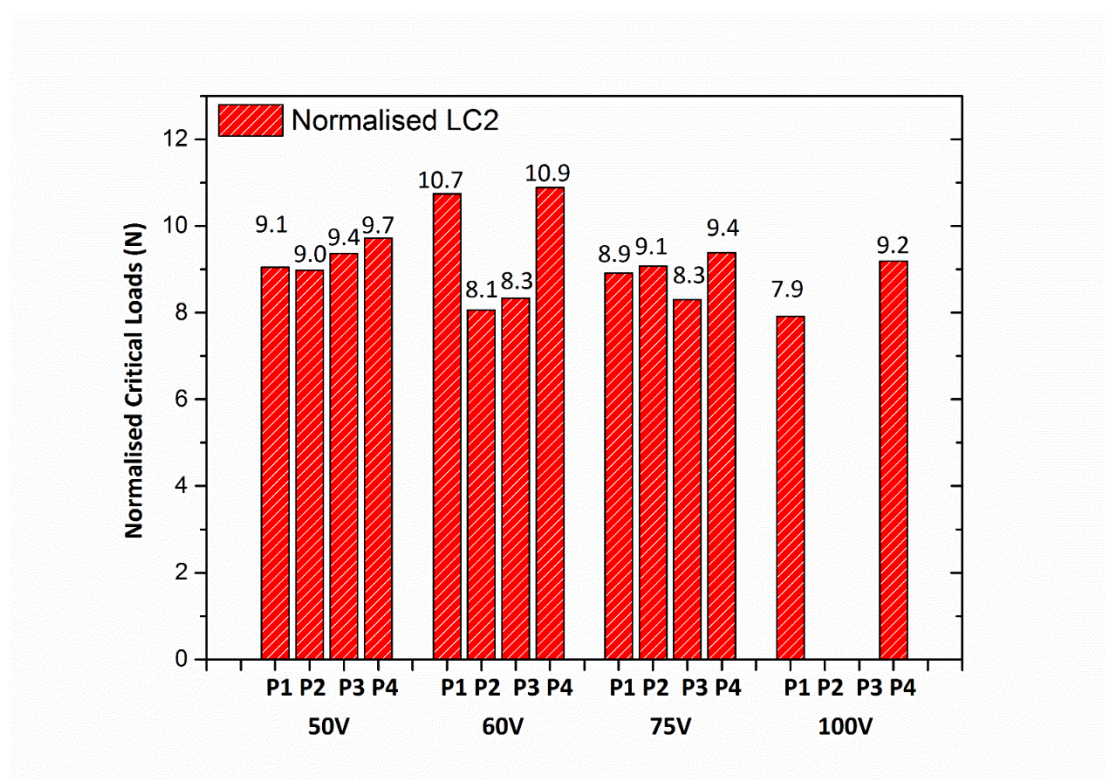


Figure 6.4: Normalised L_{C2} of AlCuMoMgZrB layers

As seen from **Figure 6.4**, the performance of the AlCuMoMgZrB layers in scratch-adhesion tests can be correlated with the nanoindentation results. The overall high values of the normalised L_{C2} of layers deposited at substrate negative bias of 50 V is attributed to their high H/E ratios. With increasing substrate negative bias, the normalised L_{C2} of P2 and P3 layers generally decreases until the testing range limits are reached. P2-100 and P3-100 layers exhibit both chipping and adhesive failures at the onset of

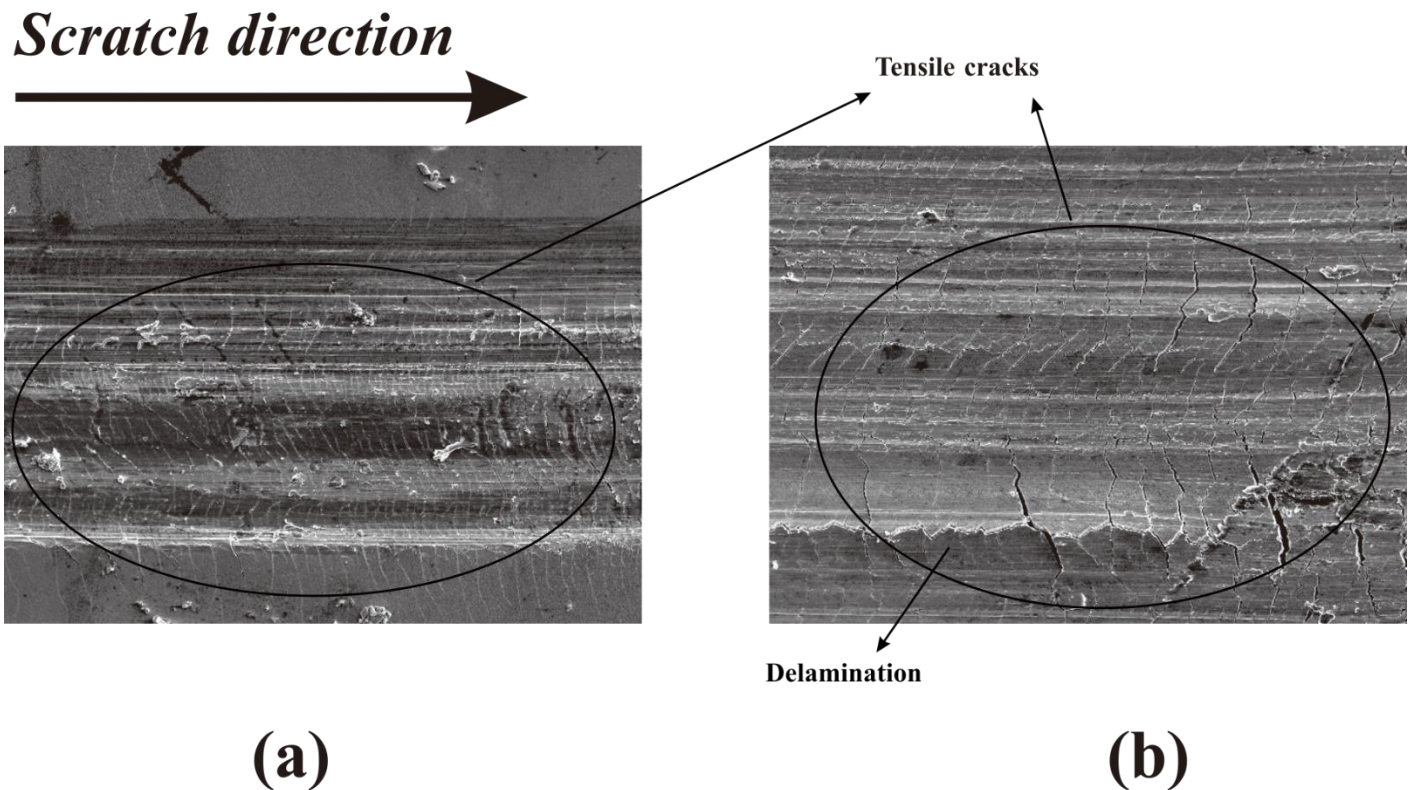
scratching. This may be related to their extremely low hardness, which could not resist the initial load (5N). As the layers (*e.g.* P2-75 and P3-75) deposited at high substrate negative bias possess low E values, their performance in the scratch-adhesion test can be enhanced by achieving good strain coherency with the underlying WE43 substrate, under plastic deformation. Overall, to obtain a good adhesion on magnesium alloy substrates requires not only a high H/E ratio, but a low E and moderately high H values.

However, some unique characteristics were found in **Figure 6.4**. Unlike the results of nanoindentation, the normalised L_{C2} values for each deposition run did not always decrease with increasing substrate negative bias. The maximum value of normalised L_{C2} was observed in the P4-60 layer. In addition, P1-60 also displays a comparable normalised L_{C2} value. Overall, P1-60 and P4-60 layers possess the two best performances, and may be considered as good base layer candidates for subsequent PVD nanocomposite coatings.

6.2.2. Comparison of adhesion between P1-60 and P4-60 layers

To further investigate the adhesion strength of the P1-60 and P4-60 samples (which have been narrowed down as candidates from the other layers in the above investigations), analysis of failure modes was carried out. In general, if the adhesion of the layer is not good enough to confine the coating material within the scratch track, brittle failure modes are likely to occur. This is especially common if using a soft material as substrate (*i.e.* WE43 alloy in this research). This is because the soft substrate is unable to provide sufficient support and thus, tends to bend under a moderate load [174].

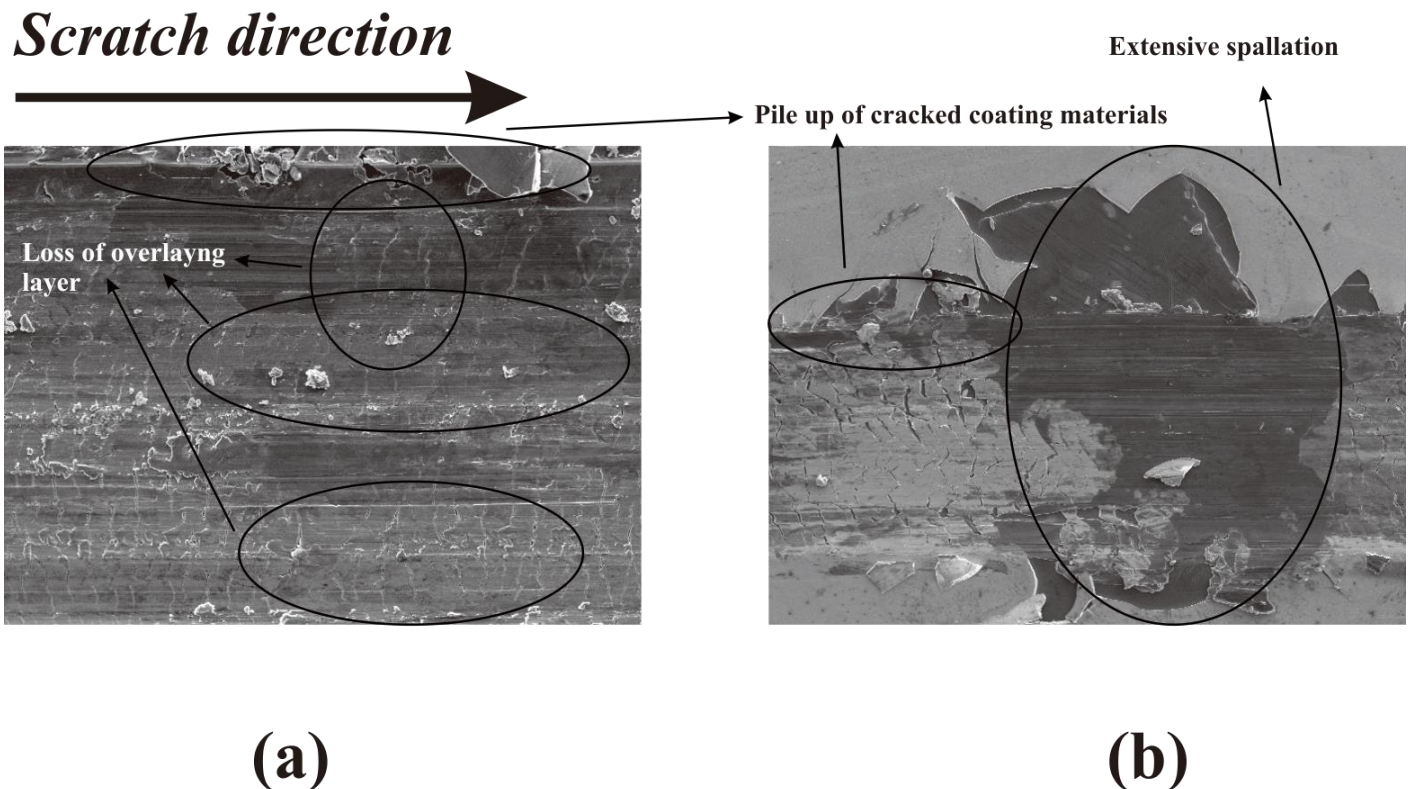
The cohesive failures of P1-60 and P4-60 layers were observed by SEM and shown in **Figure 6.5**.



(a) **(b)**
Figure 6.5 Cohesive failures of (a) P1-60; (b) P4-60

Both layers exhibit a large magnitude of through-thickness cracks before the occurrence of adhesive failure. In **Figure 6.5(a)**, the crack morphology of the P1-60 layer can be observed to open away from the direction of scratch (*i.e.* heading towards the scratch direction, which was from left to right for the present test, as indicated in the figure above). In addition, the layer damage was confined within the scratch track. It may therefore be classified as tensile (ductile) cracking, caused by the tensile stresses at the rear of the indenter during the test [173]. In **Figure 6.5(b)**, although the crack morphology of the P4-60 layer could also be considered to open away from the direction of scratch, the curvature was much less than that of the P1-60 layer. The cracks with curvature indicates an inferior

resistance to scratch sliding. Moreover, a clear delamination was seen near the track edge, possibly attributable to the large difference of elastic moduli between the P4-60 layer (~107 GPa) and the WE43 substrate (~44 GPa). The first adhesive failures of P1-60 and P4-60 layers were also observed and are shown in **Figure 6.6**.



(a) **(b)**
Figure 6.6 First adhesive failures of (a) P1-60; (b) P4-60 layers

Figure 6.6 displays the adhesive failures occurring in P1-60 and P4-60 layers. Pile-up of the cracked layer material beyond the edge of the scratch track was observed in both layers due to the substantial plastic deformation. As seen in **Figure 6.6(a)**, moderate loss of the overlying layer is present in the P1-60 sample, indicating a good adhesion of a compliant layer to soft substrate [174]. The magnitude of failure in P1-60 sample was not large (*i.e.* partial spallation) in terms of limited substrate exposure.

In **Figure 6.6(b)**, however, extensive spallation can be observed. This was

generally caused by large compressive stresses associated with the moving stylus (*i.e.* compressive spallation). In addition, delamination along the scratch track could be found. This delamination could be attributed to through-thickness cracks propagating and passing out of the loading area. The delamination and spallation of the P4-60 layer could be regarded as a consequence of minimising the amount of stored elastic energy (*i.e.* recovery spallation). This corresponds to the large difference in elastic moduli between the surface layer and the substrate. This mixture of recovery and compressive spallation has also been observed in other work [174]. The inferior performance of P4-60 indicates a higher coating internal stress than P1-60.

In summary, although the P4-60 layer had a slightly higher normalised critical load (*i.e.* L_{C2}), its failure mode was more brittle than that of the P1-60 layer. Therefore, considering the coatings used in mechanical and tribological applications, P1-60 was considered to be the most suitable base layer, among all the sixteen candidates.

6.3. Electrochemical corrosion properties

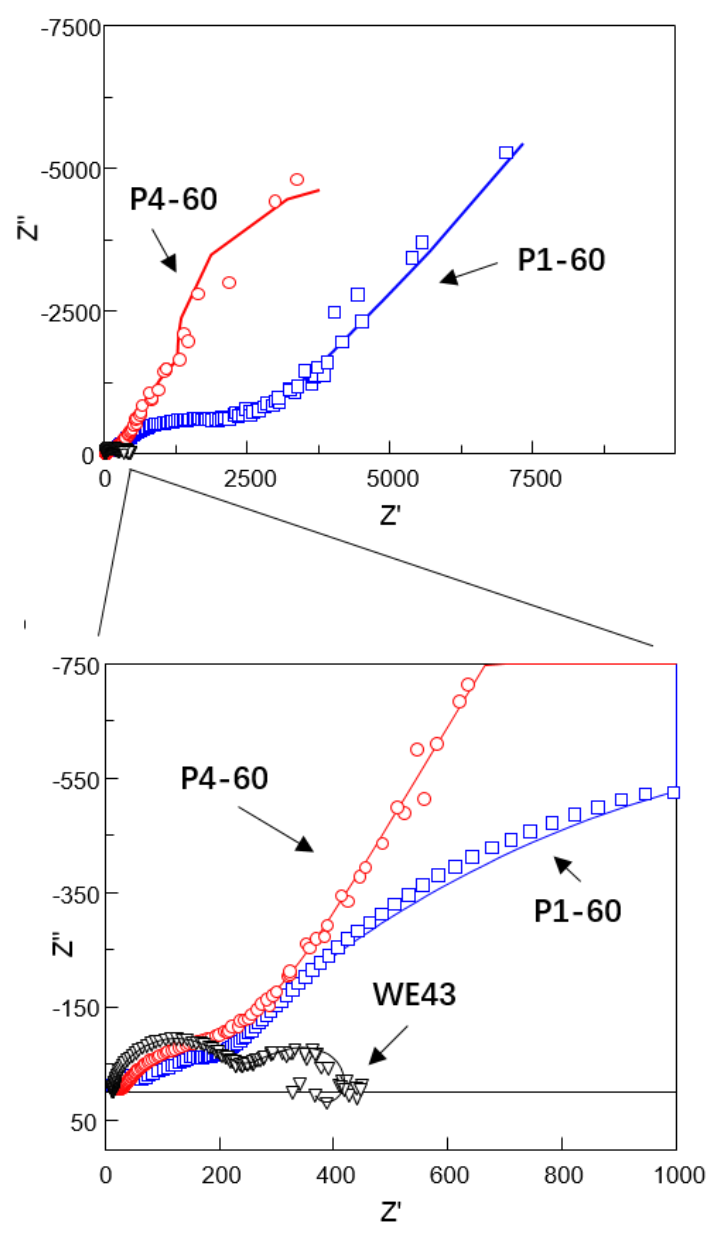
The results of scratch-adhesion tests indicate that P1-60 and P4-60 layers perform much better than other candidates. In particular, the P1-60 layer may be the best base layer for the subsequent nanocomposite PVD coating, for applications in mechanical and tribological usage.

Apart from good mechanical and tribological properties, an outstanding protection given by interfacial layer for underlying magnesium alloy substrate against corrosive environment is also important. Therefore, electrochemical corrosion properties of P1-60 and P4-60 layers should also be evaluated in order to determine and confirm the most suitable base layer.

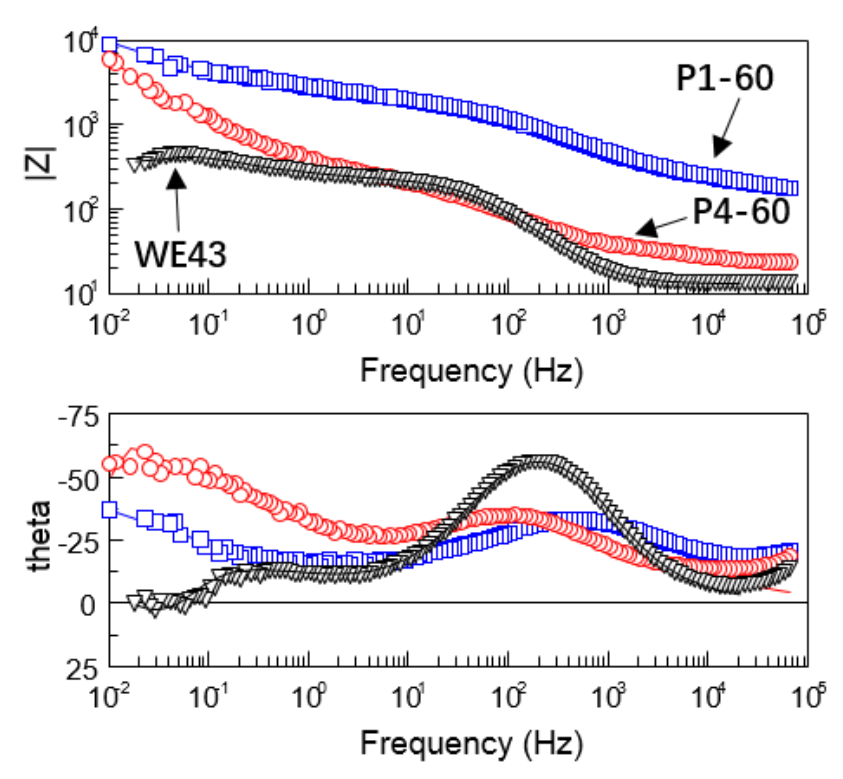
6.3.1. *Open circuit potential evaluation and electrochemical impedance spectroscopy*

The open circuit potential (OCP) of both P1-60 and P4-60 layers was found to shift to significantly more positive values, which were -0.16 V *vs.* saturated calomel electrode (SCE) and $+0.19$ V *vs.* SCE, respectively, compared to -1.75 V *vs.* SCE of WE43 substrates. The increase in OCP values is indicative of an improved electrochemical stability given by the as-deposited layers (but maybe a risk of galvanic corrosion between coating and substrate).

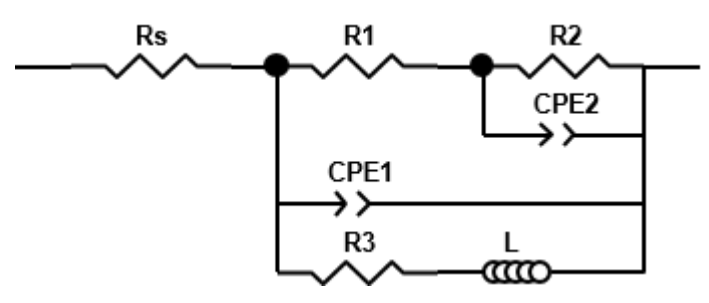
After the OCP test, the electrochemical impedance spectroscopy (EIS) was performed to reveal the corrosion properties. Characteristic impedance diagrams of P1-60 layer, P4-60 layer and WE43 substrate are displayed in **Figure 6.7**.



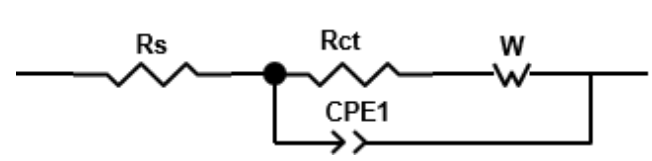
(a)



(b)



(c)



(d)

Figure 6.7 EIS analysis of P1-60 and P4-60 layers and WE43 substrate: (a) Complex plot, (b) Bode plots, (c) equivalent circuit for WE43 substrate and (d) equivalent circuit for P1-60 and P4-60 layers

Overall, the EIS spectra of both P1-60 and P4-60 layers exhibit increasing impedance when compared with that of a bare WE43 substrate (see Bode plots in **Figure 6.7(b)**), indicating improved corrosion resistance [175].

In addition, the as-deposited layers also possess different EIS behaviour compared to the substrate. In **Figure 6.7(a) and (b)**, the EIS spectra of the WE43 substrate (black lines) displayed two capacitive loops in the medium to high frequency range, and an inductive loop in the low frequency range. On the other hand, the EIS spectra of P1-60 and P4-60 layers shown in **Figure 6.7(a) and (b)** (blue and red lines, respectively) exhibit a depressed semicircle in the high frequency range and a linear slope in the low to medium frequency range.

EIS results are commonly explained using equivalent circuits [176]. The three loops displayed in the EIS spectrum of the WE43 substrate are indicative of the degradation of WE43 magnesium alloy involving different time constants. The two capacitive loops are displayed as moderately depressed rather than an ideal semicircle, suggesting a non-ideal capacitor behaviour due to the passive oxide film defects and interface roughness [177]. In this case of equivalent circuit, constant phase element (CPE) is used instead of capacitor (C). The first capacitive loop in the high frequency range represents the porous oxide film on WE43 magnesium alloy surface, which is normally displayed as a parallel combination of resistor and constant phase element in the equivalent circuit [177]. The second capacitive loop in the medium frequency range is associated with charge transfer processes, which is analogous to a parallel combination of a resistor (charge transfer resistance) and a constant phase element (double layer capacitance) [177]. The final inductive loop in the low frequency range can be represented by a series combination of resistor and inductor (L). Such inductive behaviour has been commonly recognised to be associated with active corrosion processes involving the formation of an

Mg⁺ ion intermediate corrosion product (rather than direct evolution from Mg to Mg²⁺) [178-181]. Therefore, an equivalent circuit is proposed in **Figure 6.7(c)**.

The depressed semicircles in EIS spectra of P1-60 and P4-60 layers can be regarded as an indication of non-ideal behaviour of the double layer capacitance (*i.e.* dispersive properties due to roughness and porosity) [177]. Consequently, a constant phase element is used to replace the capacitor, as mentioned above. Moreover, a Warburg impedance element (W) is introduced in the equivalent circuit to describe the linear behaviour which indicates semi-infinite diffusion behaviour. It usually refers to geometrical or activation inhomogeneity of the coating surface and represents the diffusional effects which do not obey Fick's second law (*i.e.* the rate of accumulation, or depletion, of specie concentration within the volume is proportional to the local curvature of the concentration gradient). In addition, the high intersected values in the low frequency domain of the Bode plots (**Figure 6.7(b)**) also indicate the presence of a diffusional mass transport process [176, 182]. Therefore, a typical Randles-type equivalent circuit was used to analogise the corrosion processes, as displayed in **Figure 6.7(d)**. Similar equivalent circuits have also been found in other literature to describe the corrosion processes involving charge-transfer kinetics [183-185].

The corresponding equivalent circuit data for WE43 substrate, P1-60 and P4-60 layers are listed in **Table 6.2**.

Data	WE43	P1-60	P4-60
R_s ($k\Omega \cdot cm^2$)	0.01	0.14	0.02
$CPE1-T$ ($Fsn^{-1}cm^{-2}$)	3.12×10^{-5}	2.57×10^{-5}	39.61×10^{-5}
$CPE1-P$	0.91	0.52	0.53
R_{ct} ($k\Omega \cdot cm^2$) *	0.21	2.62	0.41
$W-R$ ($k\Omega \cdot cm^2$)	-	27.27	13.05
$W-T$	-	171.10	32.64
$W-P$	-	0.53	0.71
R_2 ($k\Omega \cdot cm^2$)	0.33	-	-
$CPE2-T$ ($Fsn^{-1}cm^{-2}$)	3.98×10^{-3}	-	-
$CPE2-P$	0.48	-	-
R_3 ($k\Omega \cdot cm^2$)	1.03	-	-
L	5891	-	-

* R_{ct} refers to R_1 in the equivalent circuit of WE43 substrate

Table 6.2 Results of EIS data fitting by equivalent circuits

As seen in **Table 6.2**, the high impedance magnitude ($|Z|$) of P1-60 and P4-60 layers in **Figure 6.7(b)** is mostly attributed to the high corrosion resistance originated from the Warburg impedance (W). The values are

remarkably larger than that of R_{ct} because of the semi-infinite diffusion of charged particles, indicating the corrosion rate of P1-60 and P4-60 layers depends mainly on diffusional mass transport process.

One important parameter to assess the corrosion rate is the polarisation resistance, R_p , proposed by Birbilis *et al.* [179]. The value of polarisation resistance is thought to be inversely proportional to the corrosion rate [186]. The polarisation resistance is defined as the difference in impedance between zero and infinite frequencies. The polarisation resistance of WE43 substrate P1-60 and P4-60 layers can be obtained respectively, using the equations below:

WE43 substrate:

$$R_p = |Z|_{f \rightarrow 0} - |Z|_{f \rightarrow \infty} = \left(\frac{1}{R_1 + R_2} + \frac{1}{R_3} \right)^{-1} \quad \text{Equation 6.1}$$

P1-60 and P4-60 layers

$$R_p = |Z|_{f \rightarrow 0} - |Z|_{f \rightarrow \infty} = R_{ct} + W \quad \text{Equation 6.2}$$

By substituting the corresponding data from **Table 6.2**, the R_p of WE43, P1-60 and P4-60 can be readily calculated, which are $354 \Omega \cdot \text{cm}^2$, $29890 \Omega \cdot \text{cm}^2$ and $13460 \Omega \cdot \text{cm}^2$, respectively. Clearly, P1-60 has the highest polarisation resistance and the corresponding lowest corrosion rate. This is also consistent with the observation of the highest impedance magnitude in **Figure 6.7(b)**.

6.3.2. Potentiodynamic polarisation

Potentiodynamic polarisation scans were also utilised to qualitatively compare the corrosion rate of these samples. In the potentiodynamic polarisation graph, values of corrosion potential (E_{corr}) reveals the susceptibility of a material to corrosion. The corrosion current density (i_{corr}) describes the corrosion from a kinetic point of view. E_{corr} is defined as the potential at which the anodic current density is equal to the cathodic current density. The results of potentiodynamic polarisation evaluation are presented in **Figure 6.8**.

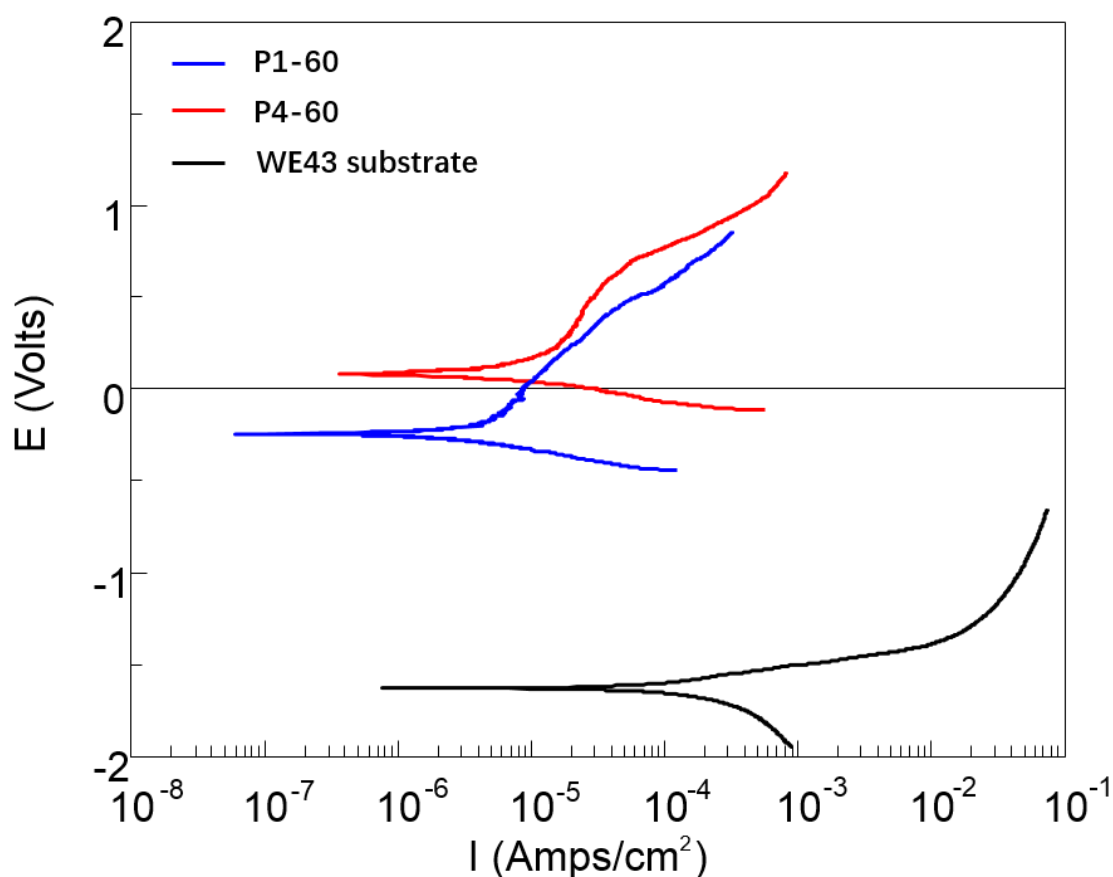


Figure 6.8 Potentiodynamic polarisation curves of WE43 substrate, P1-60 and P4-60 layers

In **Figure 6.8**, both P1-60 and P4-60 layers showed polarisation curves in a more positive region, which were shifted from -1.62 V *vs.* SCE for WE43 substrate to -0.25 V *vs.* SCE and +0.07 V *vs.* SCE for P1-60 layer and P4-60 layer, respectively. This is fairly consistent with the previous OCP results.

In general, if coatings can exhibit Tafel behaviour, the Tafel extrapolation method is applied to obtain i_{corr} . However, all the three curves in **Figure 6.8** do not show a clear Tafel behaviour. Therefore, the corrosion rates of these samples are evaluated by qualitatively comparing the relative positions of the potentiodynamic polarisation curves. Curves located to the right are indicative of a higher corrosion rate than those to the left. From this point of view, since the polarisation curves of P1-60 and P4-60 layers are both located in the left region, compared to that of WE43 substrate, it can be concluded that deposition of both layers P1-60 and P4-60 layers will reduce the corrosion rate of WE43 substrates particularly if they could be deposited with sufficient thickness to eliminate through-coating porosity and thus act as a physical barrier for the substrates. In particular, the P1-60 layer is likely to have a lower corrosion rate than P4-60 layer.

The anodic branch of the WE43 substrate increases significantly for a relative small polarised overpotential, indicating insufficient polarisation resistance. Subsequently, with further increasing polarised overpotential, the anodic current density increased only slightly due to the accumulation of corrosion products covering the sample surface.

The absence of Tafel behaviour in P1-60 and P4-60 layers could be attributed to the previously mentioned diffusional mass transport process. Moreover, their anodic branches do not show a single continuous linear behaviour, indicating multiple activation polarisation processes (*i.e.* the presence of several concurrent electrochemical reactions). If the anodic branches are too short to derive a reliable Tafel slope, i_{corr} can be

determined using the intersecting point of extrapolated linear cathodic curve and E_{corr} [187]. In this regard, i_{corr} of P1-60 and P4-60 layers are obtained as $2.32 \mu\text{A}/\text{cm}^2$ and $6.65 \mu\text{A}/\text{cm}^2$. This confirms the lowest corrosion rate provided by P1-60 layer.

6.4. Microstructural investigation of P1-60 base layer

According to the previous discussion, the P1-60 layer was chosen as the ‘best’ base layer for the subsequent nanocomposite PVD hard coating in terms of outstanding mechanical and electrochemical properties.

To confirm the microstructure of the P1-60 layer, TEM investigations were carried out. An area of the cross-section TEM foil of P1-60 layer was observed by high-resolution transmission electron microscopy technique (HRTEM). This and the selected area electron diffraction (SAED) pattern results are displayed in **Figure 6.9** below.

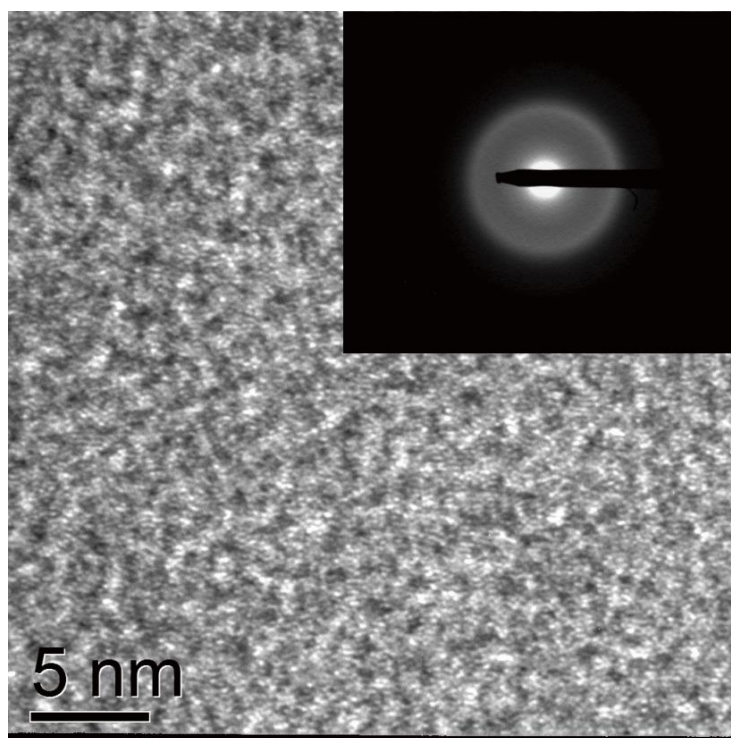


Figure 6.9 HRTEM and SAED pattern images of cross section foil of P1-60 layer

No nanocrystallinity can be observed in in **Figure 6.9**; the coating appears to be completely amorphous (with the SAED pattern displaying a typical wide and blurred diffraction ring). Both results indicate a fully amorphous microstructure for the P1-60 layer. This amorphous microstructure is beneficial for the subsequent production of a nanocomposite microstructure via the PVD process and also will tend to suppress pitting corrosion- despite the noble OCP of the coating compared to the WE43 substrate.

6.5. Summary

In this chapter, sixteen AlCuMoMgZrB layers were characterised via nanoindentation and scratch-adhesion tests. From the results, two promising layers, P1-60 and P4-60, were chosen for further characterisation experiments.

Mechanical properties

- In general, H values, E values, and H/E ratios of the layers in each deposition run can be sorted by descending order of $P4 > P1 > P2 / P3$. This may be attributed both to their elemental compositions and to the coating microstructure caused by the energetic bombardment effects during the deposition process.
- H values, E values, and H/E ratios were found to decrease with increasing substrate negative bias. This is attributed to the increasing energetic bombardment which causes rough surfaces and coarser columnar growth (with the associated voids and defects).

Adhesive strength

- The results of the scratch-adhesion test are, in general, consistent with those of nanoindentation.
- The good adhesion of the layer requires not only a high H/E ratio, but also a low E value and a moderately high H value.
- P1-60 and P4-60 layers showed superior adhesive strengths compared with other layers.
- In particular, the P1-60 layer exhibited a more ductile failure mode than the P4-60 layer, indicating a better performance in terms of withstanding plastic deformations in practical applications.

Electrochemical corrosion properties

- The electrochemical corrosion properties of the layers P1-60 and P4-60 were evaluated in detail and compared with the WE43 substrate.
- Both P1-60 and P4-60 layers, showed significantly more positive OCP values, but also much higher polarisation resistance and lower corrosion rates than the WE43 substrate.
- The P1-60 layer showed the superior performance in the tests.
- Therefore, the P1-60 layer was selected as the most suitable base layer for coupling to subsequent nanocomposite PVD hard coating.

TEM analysis

- The P1-60 layer is confirmed to possess a fully amorphous microstructure.

CHAPTER 7: INVESTIGATION OF NOVEL NITROGEN-CONTAINING ALCUMOMGZRB(N) PVD COATINGS

The previous two chapters explored the selection process followed to develop the base layer of the nanocomposite coating. As a result, the P1-60 sample was chosen as be the most suitable candidate amongst the sixteen AlCuMoMgZrB coating layers due to its superior mechanical properties, electrochemical properties, and amorphous microstructure.

In this chapter, four novel AlCuMoMgZrB(N) nanocomposite PVD coatings were produced on top of the P1-60 ‘coupling’ layer. During the deposition sequence of the AlCuMoMgZrB(N) coating, the first hour follows the production process of the P1-60 layer. Following that, the next hour of the deposition process involved the addition of nitrogen reactive gas. It should be mentioned that a 5-minute stepping period of adding nitrogen gas was used at the beginning of the final hour of each deposition run. For instance, in the deposition of P1-60-20sccm, the flow rate of nitrogen gas was increased by 4 sccm per minute from the 60th minute, reaching 4 sccm at the 61st minute, 8 sccm at the 62nd minute, *etc*, until 20 sccm at the 65th minute, and thereafter maintained constant at 20 sccm for the remaining 55 minutes.

The synthesised samples are therefore each labelled according to the final nitrogen gas flow rates applied (which were 5 sccm, 10 sccm, 15 sccm, and 20 sccm, respectively). These are shown in **Table 7.1**.

Final flow rate of nitrogen gas (sccm)	Designation	Current (A)
5	P1-60-5sccm	0.09
10	P1-60-10sccm	0.09
15	P1-60-15sccm	0.10
20	P1-60-20sccm	0.11

Table 7.1 Classification of AlCuMoMgZrB(N) nanocomposite coatings

All as-deposited AlCuMoMgZrB(N) nanocomposite coatings were then subjected to a series of tests to investigate their elemental chemical composition, phase composition, microstructure, together with mechanical, micro-abrasion wear, and corrosion property measurement.

7.1. Elemental composition

Table 7.2 shows the elemental composition of each AlCuMoMgZrB(N) coating, in atomic percentage.

Layer Designations	Elemental Compositions (at%)						
	Al	Mg	Cu	Mo	Zr	B	N
P1-60-5sccm	60.17	9.61	7.10	3.28	2.08	3.39	14.37
P1-60-10sccm	52.56	8.83	6.24	3.45	1.70	2.92	24.30
P1-60-15sccm	46.27	8.71	5.35	3.63	1.30	2.65	32.08
P1-60-20sccm	40.48	7.91	4.18	4.34	1.55	2.13	39.41

Table 7.2 EDX elemental compositions of AlCuMoMgZrB(N) coatings

The total composition of other elements (e.g. oxygen, carbon and iron) was detected below 1at%.

Therefore, their compositions were eliminated

As expected (see **Table 7.2**), the nitrogen content in the coatings increased systematically with increasing nitrogen flow rate. The introduction of nitrogen systematically decreased the fractional total of the other six elements. However, it can be clearly seen that the atomic composition of

Mo showed a net increase with increasing nitrogen content (unlike all other target elements).

If only considering the elemental content of the six elements other than N, the compositional profile of each as-deposited coating may be summarised and shown in **Figure 7.1**.

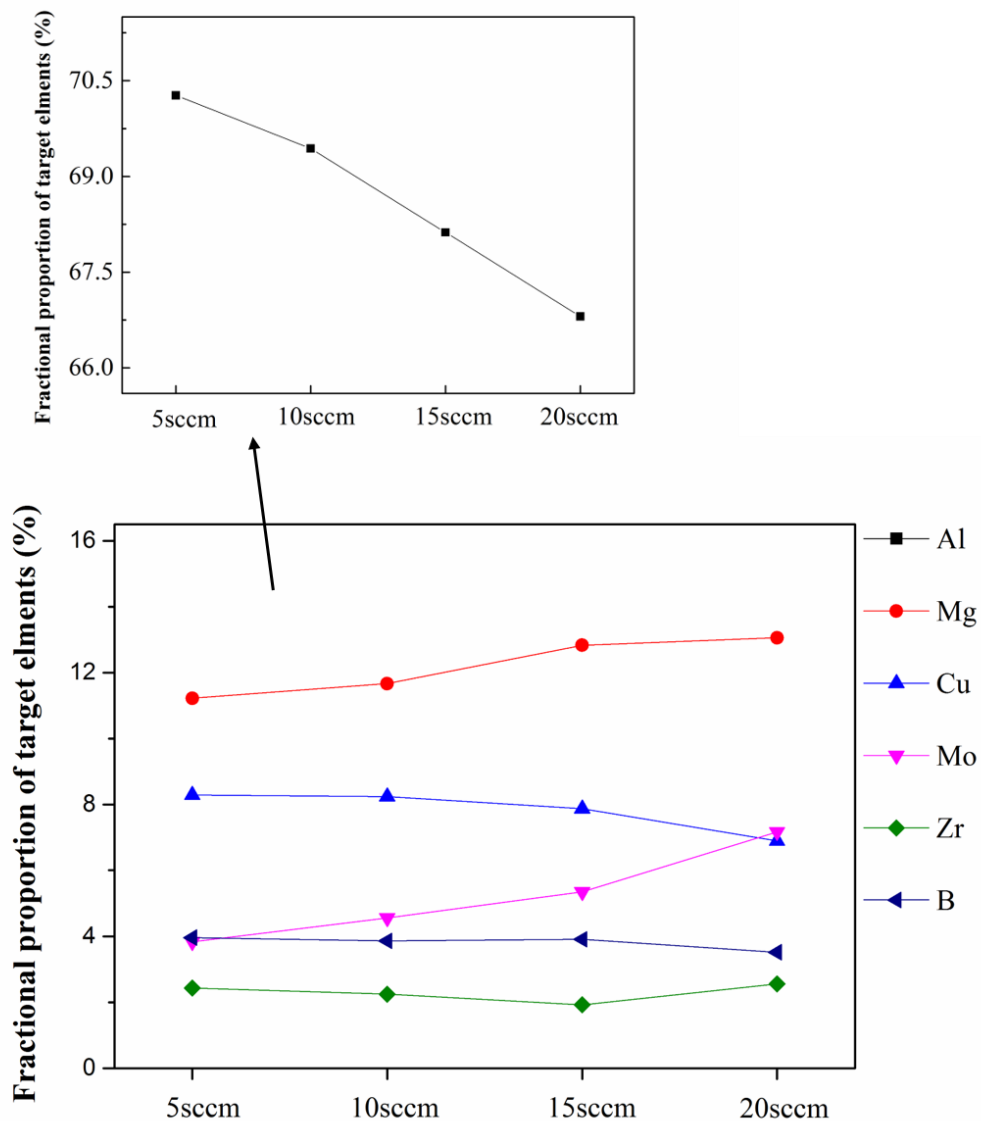


Figure 7.1 Fractional proportion of Al, Mg, Cu, Mo, Zr and B elements in each as-deposited coating excluding N

As seen from **Figure 7.1**, the net change in concentration of the six target elements with increasing nitrogen flow rate may be summarised into three separate observations: The Mg and Mo content increased, the Al and Cu content decreased, while the Zr and B content remained constant.

Unlike the observations of the elemental content of AlCuMoMgZrB base layers, obtaining and interpreting information on the compositional behaviour of the six elements is complex, in light of substrate resputtering effects and target element sputter yields (see section 5.1). In addition, the introduction of nitrogen gas did not seem to increase composition of nitride-forming elements (*i.e.* Al, Zr and Mo elements). The compositional behaviour of the six elements is probably related to phase composition of the coatings, where increasing nitrogen content appears to affect formation of certain phases, thus leading to a change in the concentration of the corresponding elements, which will be discussed in detail in section 7.2.

7.2. Phase composition

The phases present in each AlCuMoMgZrB(N) coating were investigated via GAXRD, the patterns of which are shown in **Figure 7.2** below.

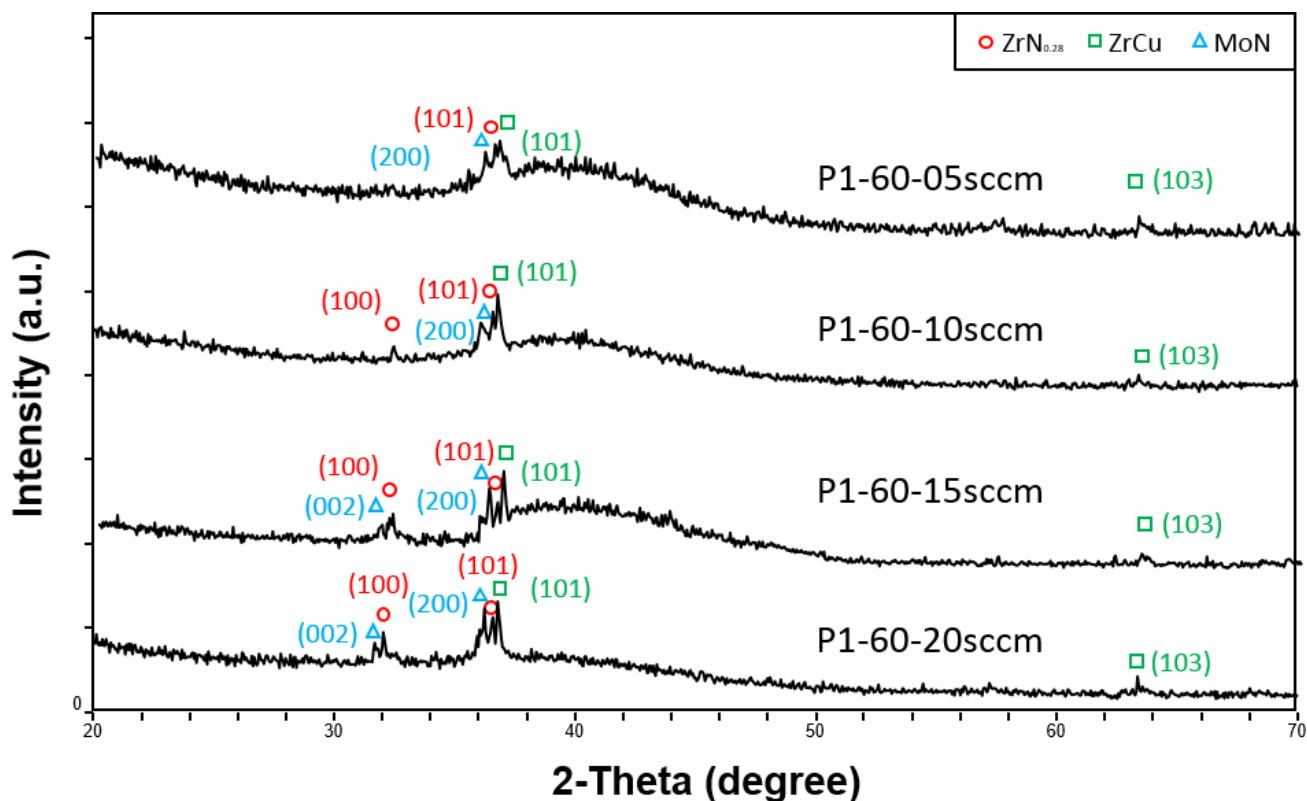


Figure 7.2 GAXRD patterns of AlCuMoMgZrB(N) coatings

Compared with the XRD pattern of the P1-60 base layer which showed highly amorphous characteristic (see **Figure 5.3**), the XRD patterns of all nitrogen-containing coatings exhibited nanocrystalline characteristics in terms of sharp peaks appearing on (or adjacent to) the broad amorphous reflection. This is indicative of the formation of ultra-fine crystallites with the amorphous matrix.

7.2.1. *Formation of characteristic peaks*

As shown in **Figure 7.2**, the characteristic peaks visible in the XRD patterns can be identified as nitrides and a ZrCu intermetallic phase. The formation of ceramic nitrides is expected to increase hardness. However, the formation of the ZrCu intermetallic phase may be deleterious to the corrosion resistance of the coating system. The ZrCu intermetallic phase might be galvanically coupled to the cathodic amorphous matrix (with OCP~-0.16V, see section 6.3). Therefore, microgalvanic cell action may be promoted, leading to an accelerated corrosive attack.

Furthermore, characteristic peaks become narrower and sharper with increasing nitrogen content. Such peak shape evolution was previously found to correlate with larger crystallite size and a columnar microstructure [188].

Moreover, peaks characteristic of $ZrN_{0.28}$ and MoN were observed to appear in coatings possessing high nitrogen content. The appearance of MoN peaks seems to correlate with the results shown in **Figure 7.1**, which showed an increase in Mo content as the nitrogen flow rate increased.

7.2.2. Confirmation of nanocomposite microstructure

To confirm nanocrystallite formation resulting from the introduction of nitrogen, high-resolution transmission electron microscopy (HRTEM) was used to observe the P1-60-5sccm and P1-60-20sccm microstructures. The results are shown in **Figure 7.3**.

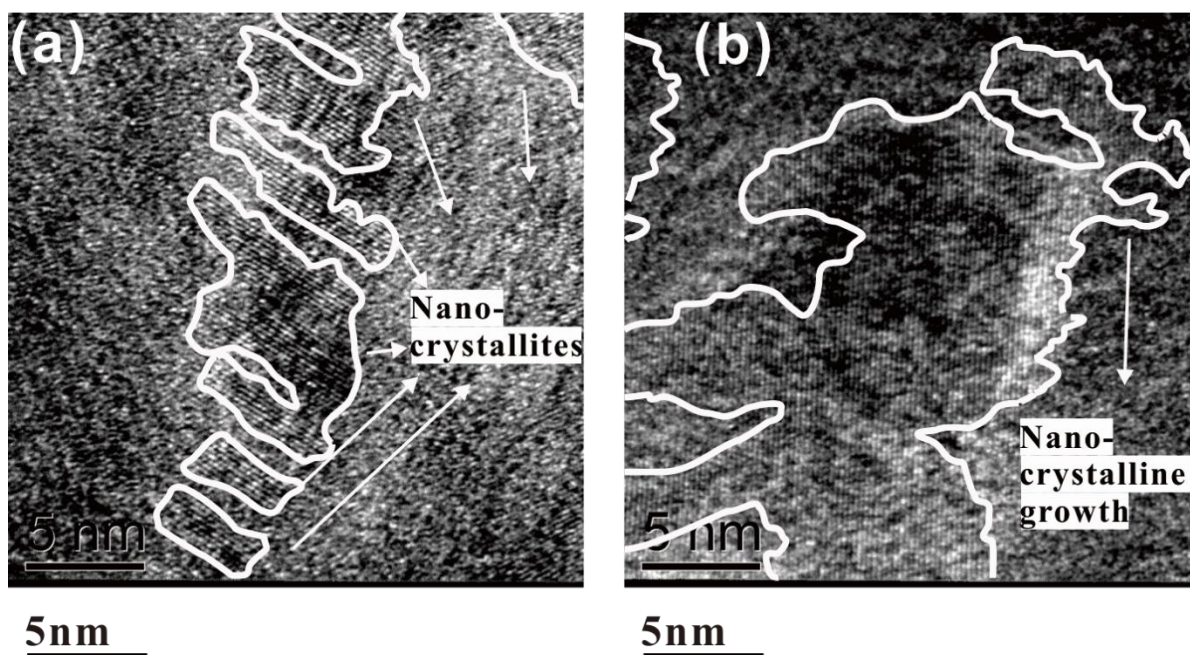


Figure 7.3: HRTEM images of (a) P1-60-5sccm; (b) P1-60-20sccm

As seen in **Figure 7.3**, nanocrystallites were observed in both images with sizes ranging from a few nanometres to several tens of nanometres.

The selected area electron diffraction (SAED) pattern image of P1-60-15sccm is shown in **Figure 7.4**.

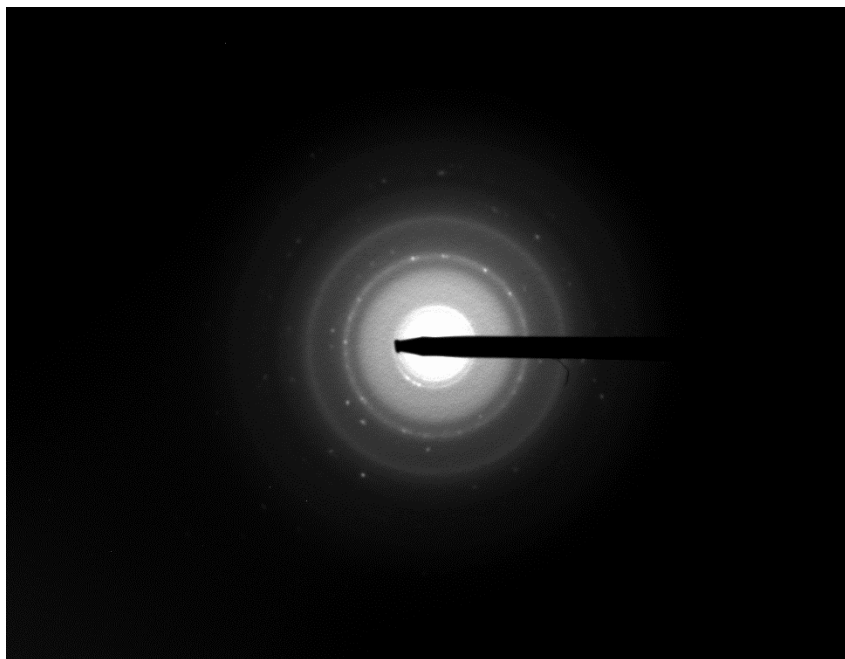


Figure 7.4 SAED pattern images of P1-60-15sccm coating

Small diffraction spots can be seen in Figure 7.4. The limited amount of spots (with relatively low intensity) indicates the presence of crystallites with ultra-fine grain sizes, which are embedded in an amorphous matrix. According to the results of the XRD patterns, P1-60-15sccm is the coating with the second-highest degree of crystallisation. Consequently, it is reasonable to conclude that all AlCuMoMgZrB(N) coatings possess a nanocomposite microstructure.

7.3. Thickness and morphology

7.3.1. Fracture cross-sections

Fractured cross-sectional morphologies of AlCuMoMgZrB(N) coatings were observed by SEM and are shown in **Figure 7.5**.

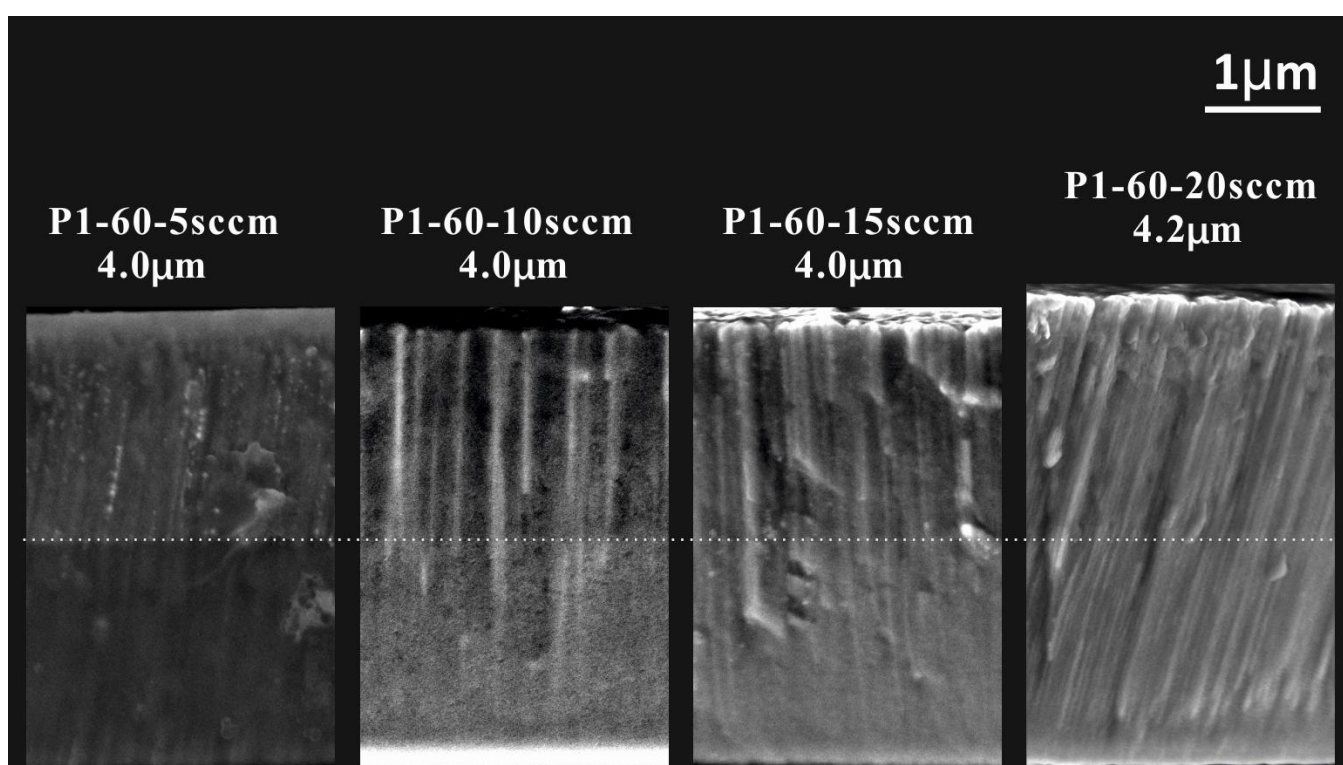


Figure 7.5 Fracture cross-sectional morphologies of AlCuMoMgZrB(N) coatings

All four nitrogen-containing coatings shown in **Figure 7.5** possessed a thickness of around 4.0 μm. The coatings displayed a columnar fracture morphology. Additionally, columnar growth near the top surface was clearly observed, with increasing nitrogen content.

Grains in the coatings are observed to coarsen with increasing N content. Therefore, N is considered as a ‘grain promoter’, which serves to facilitate surface diffusion and crystallisation. This corresponds also to the increasing column size found nearer to the coating surface in the fractured sample’s morphology – and to the appearance of an increasing number of sharp characteristic peaks in the XRD patterns of the coatings with high nitrogen content.

Another noticeable feature is the evolution of a boundary between the base layer and the nitrogen-containing coating (the dotted line in **Figure 7.5**). For the P1-60-5sccm coating, the boundary is easily identified to be between the top columnar morphology and the bottom featureless morphology. As N content increases however, the boundary become less distinct and the fracture cross-sectional morphology tends to become more homogeneous. This may be attributed to the improved surface diffusion at high N content with sufficient atom mobility to form crystalline columns. In addition, excessive N atoms (‘escaped’ from the reaction with nitride-forming elements in the plasma) can penetrate below initial nucleation sites at early stages of deposition. The penetrated N atoms react with nitriding-forming elements (*i.e.* Al, Zr and Mo) underneath to produce a columnar microstructure.

7.3.2. Surface morphology

The surface morphologies of the four coatings were observed by SEM. The results are shown in **Figure 7.6**.

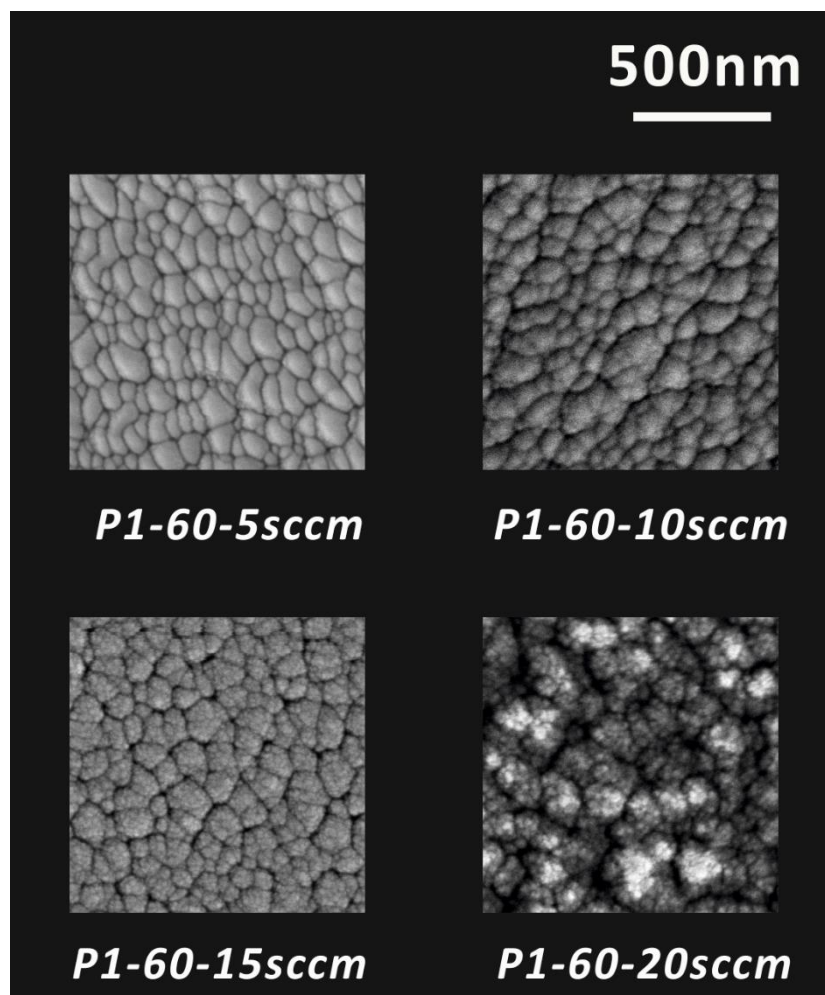


Figure 7.6 Surface morphologies of AlCuMoMgZrB(N) coatings

The surface morphology of the coatings appears to exhibit roughening with increasing N content. The surface of the P1-60-5sccm coating is observed to show the bump-shaped morphology, which is consistent with the surface morphology of nitrogen-free P1-60 base layer (see **Figure 5.5** in Chapter 5). The surface morphology evolves to be cauliflower-shaped feature in the

P1-60-20sccm coating. This surface morphology indicates competitive columnar grain growth among different columns. This is in agreement with the observation of the fracture cross-sectional morphology and XRD characterisation. Moreover, some voids and porosity appear as the nitrogen content increases, particularly for the P1-60-20sccm coating surface.

The cauliflower-shaped surface morphology may be attributed in part to the effect of non-uniform ion bombardment. As **Table 7.1** shows, all substrate currents during deposition of the top nanocomposite coatings are higher than that of the base P1-60 layer (*i.e.* with no nitrogen content; see **Table 4.2** in chapter 4). In addition, the current recoded in **Table 7.1** is increased when a higher nitrogen flow rate is introduced. This indicates a higher flux of ions (which are, in fact, likely to be mainly metal ions) arriving at the surface as the nitrogen content increases. As a consequence, ion bombardment is promoted. Moreover, a promotion of columnar growth with the increasing nitrogen content is observed in the fracture cross-sections. The P1-60-20sccm sample is considered to tend to form surface protuberances at the early stages of film growth. The protuberances are likely to be subjected to preferential sputtering effects from the arriving energetic ions due to a local non-uniformity of bombardment caused by the coating topography. This, in turn, leads to many small defects on the protuberances; furthermore, ion bombardment occurring in the open, inter-columnar area of the P1-60-20sccm coating (compared to the more dense counterparts deposited at lower nitrogen flow rate), is expect to further promote the formation of voids and porosity.

The two-dimensional profiles of the coating surfaces were characterised by a Veeco Dektak® 150 stylus profilometer (see **Figure 7.7**). The results lead to the conclusion that the coating surface roughness increases significantly with increasing nitrogen content.

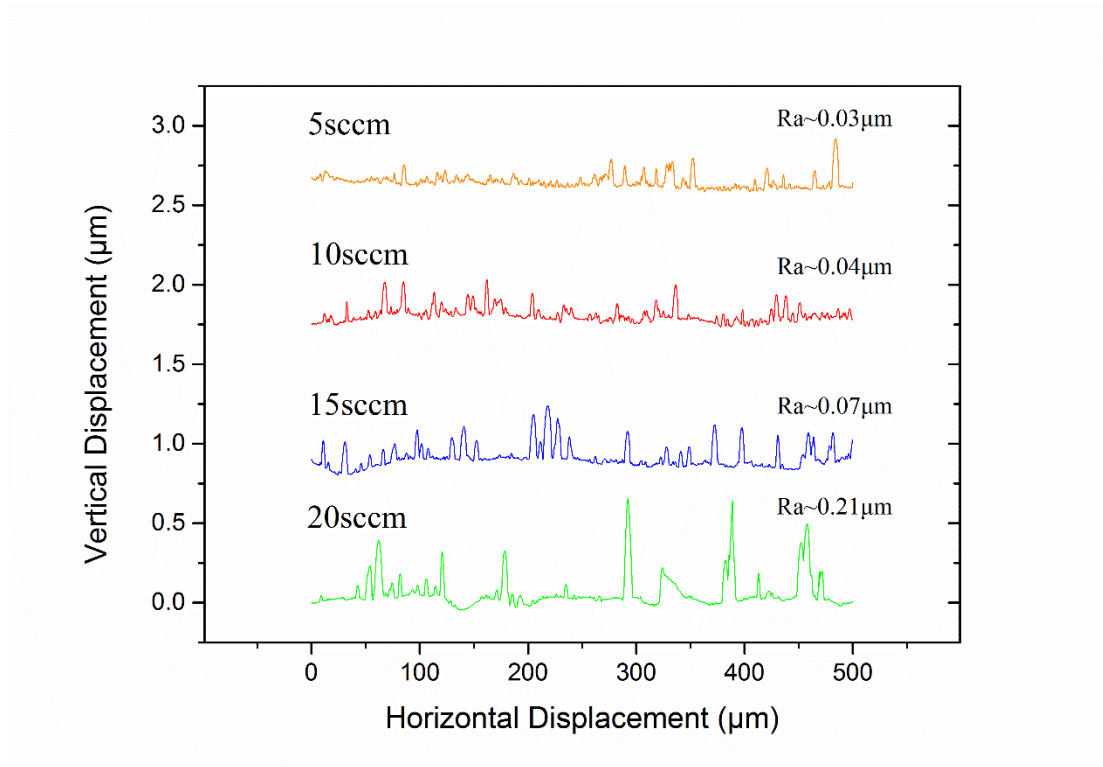


Figure 7.7 Two-dimensional surface profilometry of AlCuMoMgZrB(N) coatings

7.4. Mechanical properties

The mechanical properties (*i.e.* hardness and elastic modulus) of the AlCuMoMgZrB(N) coatings were evaluated through nanoindentation. The results are shown in **Figure 7.8**.

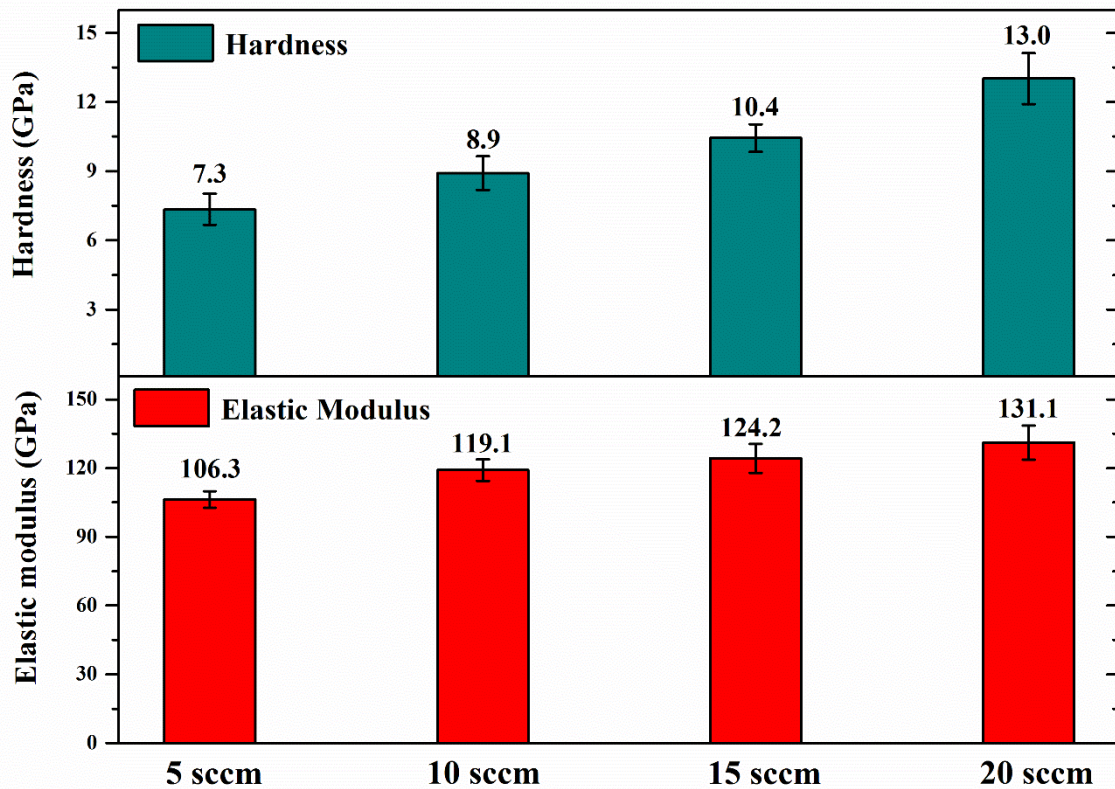


Figure 7.8 Hardness and elastic modulus of AlCuMoMgZrB(N) coatings

As seen in **Figure 7.8**, both H and E values of the coatings were found to increase with nitrogen content. Moreover, variations of H and E values were also found to increase with nitrogen content. This is indicative of unstable deformation behaviour in practical applications. This increasing variation is expected to be correlated to the roughening effect of surface.

The presence of voids and porosity seen in coatings of high nitrogen content is expected to cause unstable performance in the Nanoindentation tests.

The H/E ratios of the coatings are shown in **Figure 7.9**.

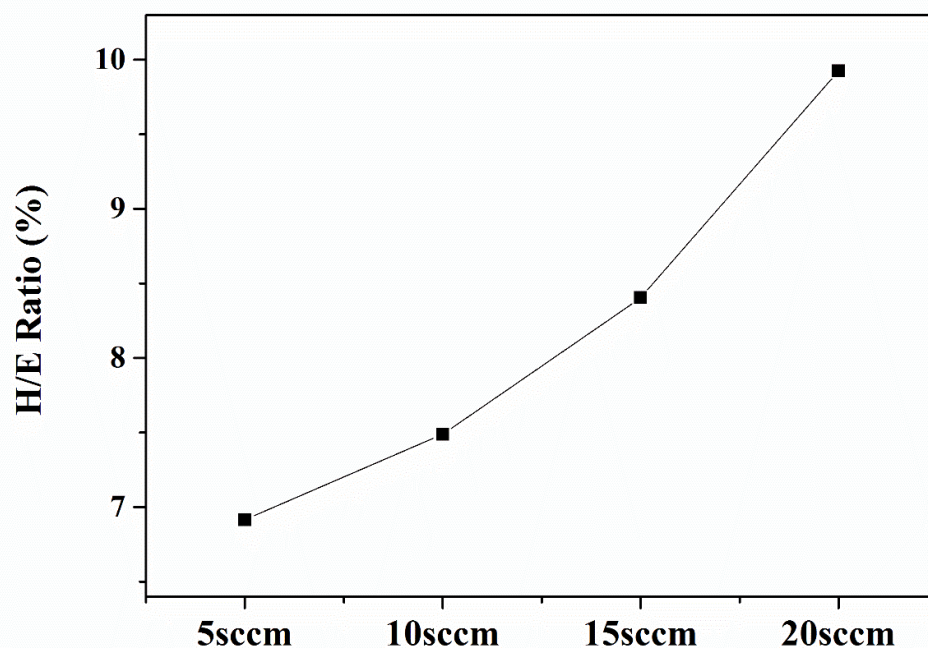


Figure 7.9 H/E ratios of AlCuMoMgZrB(N) coatings

Figure 7.9 shows a significant improvement of the H/E ratio with increasing N content. The highest ratio was close to 0.1 (0.099). The increase of the H/E ratio may be contributed to by the precipitation of ceramic nitrides (which serve to increase hardness) in an amorphous matrix (which acts to retain low elastic modulus). However, the increase in open columnar structure (and associated voids and porosity) at higher nitrogen flow might lead to reductions in (particularly) the measured E-values (*i.e.* the ‘real’ increase of E in the coating material (with increasing nitrogen flow) may be even more than Figure 7.8 suggests, so the H/E values in Figure 7.9 above should be treated with caution.

7.5. Abrasive wear behaviour

Both non-perforating and perforating tests were carried out to evaluate the specific wear rates of the coatings. The corresponding number of ball revolutions is 30, 50, 70 and 100, 120, 150, 200, 250 respectively.

The specific wear rates of the coatings from the non-perforating test were compared shown in **Table 7.3**.

<i>Sample</i>	<i>k_c ($\times 10^{-4}$ mm³/Nm)</i>
P1-60-5sccm	11.60
P1-60-10sccm	7.16
P1-60-15sccm	6.90
P1-60-20sccm	11.05

Table 7.3 Specific wear rates of AlCuMoMgZrB(N) coatings from non-perforating micro-abrasion tests

In addition, a micro-abrasion test was also carried out on the WE43 substrate, which revealed a specific wear rate of $k_s=236.81 \times 10^{-4}$ mm³/Nm. All coatings in **Table 7.3** showed much lower specific wear rate than the substrate (at least 95% lower). It should be mentioned that in soft materials such as magnesium alloys, smear, rather than abrasion wear may be the dominant wear mechanism [189].

P1-60-15sccm was found to possess the lowest specific wear rate in the non-perforating test. The specific wear rate was observed to decrease with

increasing nitrogen content in the coating as the nitrogen flow rate increases (seen from coatings P1-60-5sccm to P1-60-15sccm). However, P1-60-20sccm appears to have a higher specific wear rate compared to P1-60-15sccm. The reason for this will be discussed later by combining the results from the perforating test.

As previously mentioned, the specific wear rates of both coating and substrate from the perforating test can be obtained by plotting the linear fit of SW/V against V_C/V . Through knowledge of the intercept and slope of the linear equation, the specific wear rates of coating (k_c) and substrate (k_s) can be obtained; these are shown in **Table 7.4**.

<i>Sample</i>	$k_c (x10^{-4} mm^3/Nm)$	$k_s (x10^{-4} mm^3/Nm)$
P1-60-5sccm	17.22	213.49
P1-60-10sccm	10.77	169.90
P1-60-15sccm	7.91	214.78
P1-60-20sccm	16.97	125.76

Table 7.4 Specific wear rates of AlCuMoMgZrB(N) coatings and substrate from perforating test

Similar to the results of non-perforating test, the magnitude of k_c was found to be sorted by descending order of P1-60-15sccm > P1-60-10sccm > P1-60-20sccm > P1-60-5sccm.

Among P1-60-5sccm, P1-60-10sccm and P1-60-15sccm coatings, k_c appears to follow $1/H_C$ trend, which is consistent with the prediction of

Archard for abrasive wear [190]. However, the increase of k_c of P1-60-20sccm indicates that, although high H values gives resistance to scratching and/or ploughing, E values should also be low enough (preferentially close to the substrate) to resist plastic deformation against a counterface [191]. This is particularly relevant in the present research. Moreover, the rough surface of P1-60-20sccm is expected to accelerate the abrasion to some extent. At the beginning of the test, the local contact stresses on the coating surface increase as a result of the small real contact area. Hence, the instantaneous wear rate is increased.

k_c was found to be larger in the perforating test compared with that in the non-perforating test. This may be attributed to the possibility that, with the increasing number of revolutions, larger grains near the top surface are plucked out and may act as an additional source of wear particles to the subsequent softer base layer and substrate. This situation has also been observed in other study [192].

The decreased k_s in the perforating tests is likely to be due to the edge of the coating around the worn substrate supporting the ball and resisting further abrasion. The forward movement of the ball is therefore impeded by the remaining ‘rim’ of hard coating.

Overall, in both non-perforating and perforating tests, P1-60-15sccm coating was found to have the highest abrasive wear resistance.

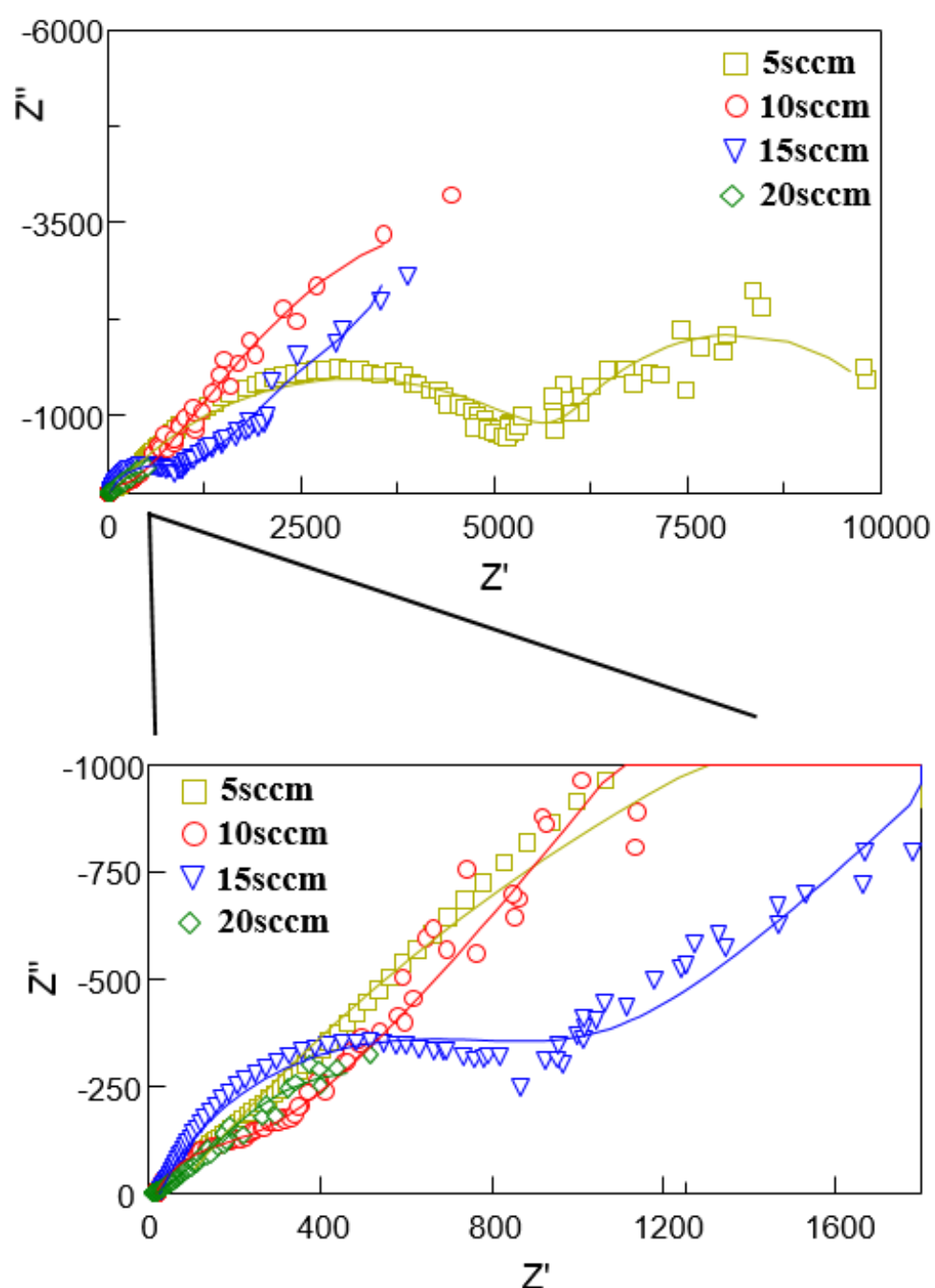
7.6. Electrochemical corrosion properties

The electrochemical corrosion properties of the AlCuMoMgZrB(N) coatings were evaluated by carrying out open circuit potential (OCP) stability test, electrochemical impedance spectroscopy (EIS), and potentiodynamic polarisation scans.

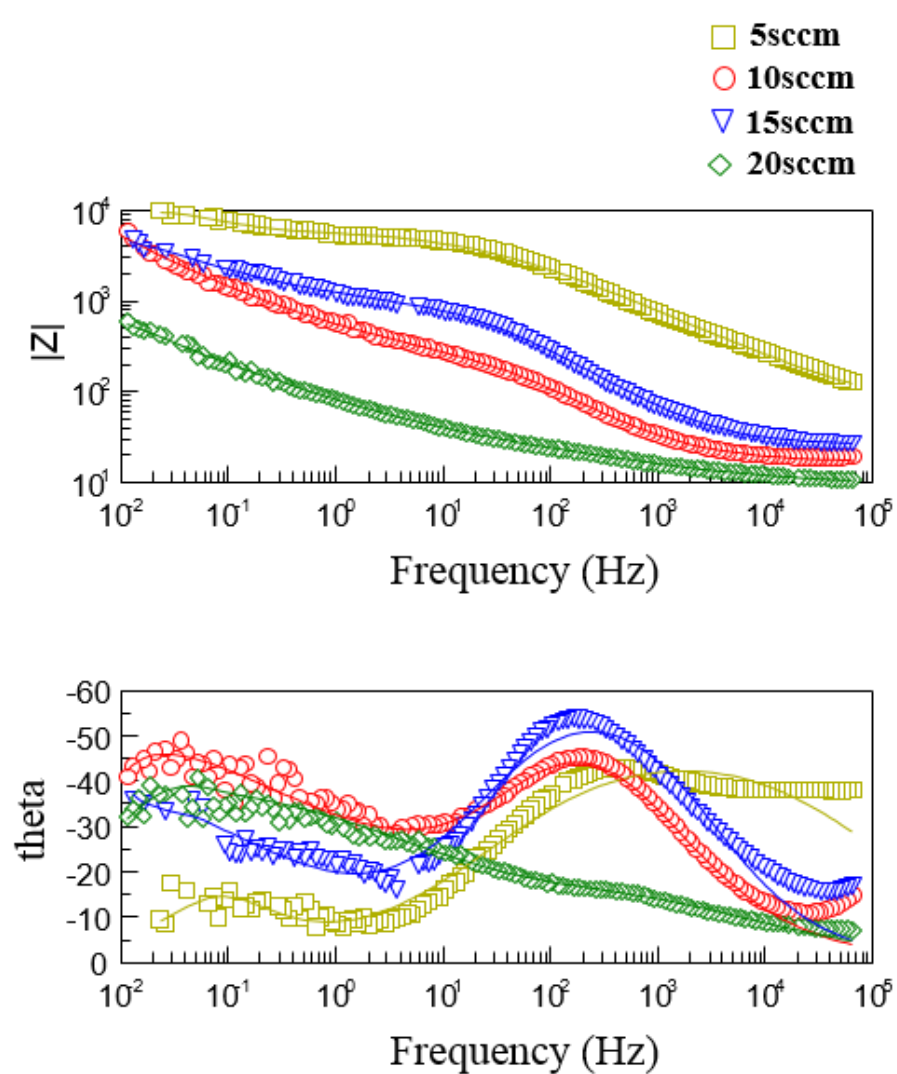
7.6.1. Open circuit potential evaluation and electrochemical impedance spectroscopy

The OCPs of the four coatings deposited with the increasing nitrogen flow rate from 5 sccm to 20 sccm were -1.05 V, -1.09 V, -1.13 V and -1.15 V, respectively. The OCPs of the coatings were found to be located between P1-60 base layer (\sim -0.16 V) and the substrate (\sim -1.75 V). The introduction of nitrogen content was observed to significantly reduce the OCP of the coating.

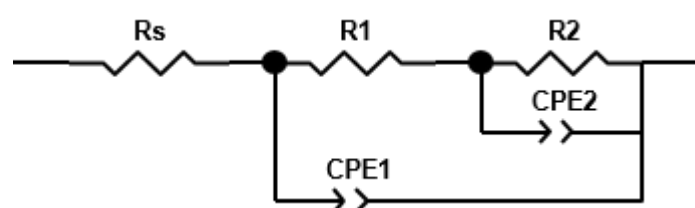
After the OCP test, EIS was carried out. The characteristic impedance of the coatings together with corresponding equivalent electric circuits were shown in **Figure 7.10**.



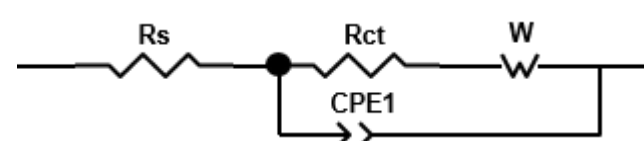
(a)



(b)



(c)



(d)

Figure 7.10 EIS analysis of AlCuMoMgZrB(N) coatings: (a) Complex plot, (b) Bode plots, (c) equivalent circuit for P1-60-5sccm coating and (d) equivalent circuit for P1-60-10sccm, P1-60-15sccm and P1-60-20sccm coatings

As seen from **Figure 7.10(b)**, the Bode plots reveal a tendency that the impedance of the coatings decreased with the increasing nitrogen content. P1-60-5sccm was found to show the largest magnitude of impedance, indicating the best corrosion resistance [175].

The coatings also exhibited different EIS behaviours. In **Figure 7.10(a)**, the EIS spectrum of P1-60-5sccm (yellow line) was observed to show two capacitive loops: one in the high to medium frequency range and the other in the low frequency range. The spectra of other coatings showed a diffusion-controlled impedance behaviour: a depressed semicircle in the high frequency range and a linear slope in the low to medium frequency range. This impedance behaviour was also observed in the spectrum of the P1-60 base layer (see **Figure 6.7(a)** in Chapter 6).

Equivalent circuits are normally proposed as a means to help interpret the EIS behaviour of the test materials [176]. All capacitive loops shown in **Figure 7.10** appear to be moderately depressed, indicating a non-ideal capacitor behaviour because of the coating defects and interface roughness [177]. Therefore, a constant phase element (CPE) is utilised to replace capacitor (C) in the present research.

The equivalent circuit of P1-60-5sccm contains two time constants (**Figure 7.10(c)**). CPE1 corresponds to the outer AlCuMoMgZrB(N) nanocomposite coating and CPE2 represents the inner amorphous

AlCuMoMgZrB base layer. The additional time constant is in agreement with the observation of the fracture morphology of P1-60-5sccm (see **Figure 7.5**). A distinct boundary between the top nanocomposite coating and the bottom amorphous base layer can be seen. Therefore, a two-layer structure is likely to form and causes the corrosion mechanism.

Similar to P1-60 base layer, a typical Randles type equivalent circuit is applied as an analogy to the corrosion processes of the P1-60-10sccm, P1-60-15sccm and P1-60-20sccm coatings. A Warburg element (W) is used to describe the linear behaviour. It is indicative of a mass transport/diffusion dominated process which generally happens for a case where diffusion does not obey Fick's 2nd law. Moreover, the high intersection in the low frequency domain of the Bode plots also supports the presence of diffusional mass transport process [176, 182].

The different EIS behaviours between the P1-60-5sccm coating and the other three coatings may correlate with their different crystalline phase constituents (*i.e.* predominantly intermetallic precipitates for P1-60-5sccm and ceramic precipitates for the others).

The data for the equivalent circuits are listed in **Table 7.5**.

Data	5 sccm	10 sccm	15 sccm	20 sccm
$R_s (k\Omega \cdot cm^2)$	0.06	0.02	0.03	0.01
$CPE1-T$ ($Fsn^{-1}cm^{-2}$)	9.18×10^{-6}	8.24×10^{-5}	2.72×10^{-5}	1.93×10^{-3}
$CPE1-P$	0.56	0.72	0.74	0.46
$R_l (k\Omega \cdot cm^2)$	6.22	0.29	0.96	0.02
$W-R (k\Omega \cdot cm^2)$	-	7.52	8.89	1.00
$W-T$	-	39.75	55.47	30.72
$W-P$	-	0.53	0.50	0.45
$R_2 (k\Omega \cdot cm^2)$	4.38	-	-	-
$CPE2-T$ ($Fsn^{-1}cm^{-2}$)	5.43×10^{-4}	-	-	-
$CPE2-P$	0.91	-	-	-

Table 7.5 Numerical results of EIS data fitting by equivalent circuits for AlCuMoMgZrB(N) coatings

As introduced in section 6.3.1, the polarisation resistances R_p can be 10.60 $\text{k}\Omega\cdot\text{cm}^2$, 7.81 $\text{k}\Omega\cdot\text{cm}^2$, 9.85 $\text{k}\Omega\cdot\text{cm}^2$ and 1.02 $\text{k}\Omega\cdot\text{cm}^2$, respectively, for the coatings with the increasing nitrogen content. The calculated results are in general, consistent with the observation of the EIS spectra.

7.6.2. Potentiodynamic polarisation scans

Potentiodynamic polarisation scans was also carried out to compare the corrosion rate of the coatings. The results, together with the polarisation curve of P1-60 base layer, are shown in **Figure 7.11**.

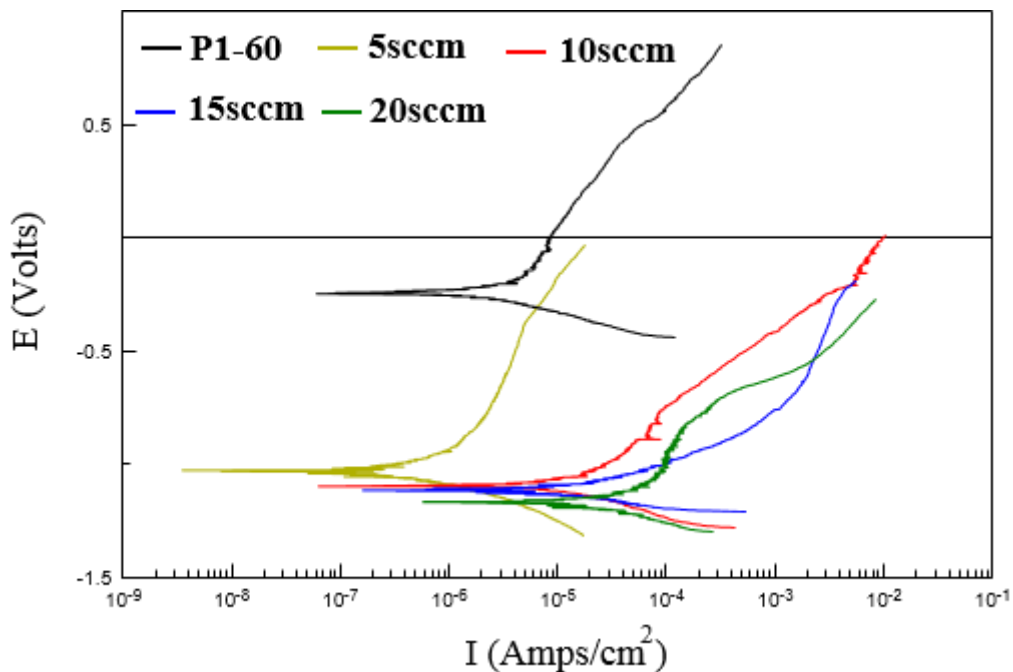


Figure 7.11 Potentiodynamic polarisation curves of AlCuMoMgZrB(N) coatings and the P1-60 base layer (ie. '0 sccm').

The corrosion potential (E_{corr}) of the curves shown in **Figure 7.11** is consistent with the result of the OCP tests. In addition, non-ideal Tafel behaviour was observed, in particular for the coatings which showed diffusion-controlled impedance behaviour. This should be attributed to the diffusional mass transport process. Thus, the intersecting point between extrapolated linear cathodic curve and E_{corr} is used to determine the corrosion rate (i_{corr}) [187]. The values of i_{corr} of the coatings with increasing nitrogen content is found to be $0.97 \mu\text{A}/\text{cm}^2$, $9.1 \mu\text{A}/\text{cm}^2$, $6.9 \mu\text{A}/\text{cm}^2$ and $18.70 \mu\text{A}/\text{cm}^2$. This is consistent with the calculation result of R_p from EIS spectra. From this, P1-60-5sccm can be confirmed to have the best corrosion resistance.

The degradation of corrosion resistance of the coatings with high nitrogen content is expected to correlate with surface roughening. The surface with voids and porosity allows the electrolyte to penetrate through the coating and react with underlying base layer and/or substrate. Another reason is considered to relate to the type of nanocrystallisation promoted by the nitrogen incorporation. As the nitrogen content increased in the coating, more ceramic nanocrystallites (*i.e.* $\text{ZrN}_{0.28}$ and MoN as XRD patterns show, see Figure 7.2) are found. This indicates that, with precipitation of Zr, Mo (and with these crystallites possibly also continuing Cu – either as an

intermetallic at lower nitrogen content, or substituted in the nitride at higher nitrogen content), an increasing proportion of Al (with a standard electrode potential of ~ -1.66 V) and Mg (with a standard electrode potential of -2.69 V) is 'left behind' in the amorphous matrix. Some Al and/or Mg precipitates may be formed (although these cannot be detected with confidence by XRD). The strong electronegativity of the elements remaining in the amorphous matrix would thus tend to decrease the overall OCP value of the coating system. In addition, the precipitated nanocrystallites are promoted to grow and accumulate as a cathodic phase, with increasing nitrogen content. As a result, local microcell reactions may in turn occur, accelerating corrosion of the coating (but possibly also protecting the substrate, indirectly).

7.7. Summary

Four AlCuMoMgZrB(N) nanocomposite coatings were produced with by applying different nitrogen flow rates (*i.e.* 5 sccm, 10 sccm, 15 sccm and 20 sccm). The as-deposited coatings were subjected to a series of tests to investigate their elemental chemical composition, phase composition, microstructure, together with mechanical, micro-abrasion wear, and corrosion property. Overall, AlCuMoMgZrB(N) nanocomposite coatings

offer good wear and corrosion protection to the underlying WE43 substrate.

The results are summarised as follows:

- The introduction of nitrogen content led to the formation of nitrides and intermetallic phase for all coatings.
- With increasing nitrogen content, the growth of both nitrides and intermetallic phase were promoted in which the growth MoN phase in the coatings with high nitrogen content may correlate with the corresponding net increase in elemental composition of Mo.
- Increasing levels of nanocrystallite precipitation were observed with increasing nitrogen content.
- All coatings displayed a columnar fracture morphology and the open columnar features were observed to be promoted with increasing nitrogen content.
- A coating surface roughening effect (and associated voids and porosity) was found with increasing nitrogen content.
- H and E values, and H/E ratios were found to increase with increasing nitrogen content in which P1-60-20sccm coating showed an H/E ratio approaching 0.1 (0.099), however the H/E values may be misleading – due to the development of coating porosity at higher nitrogen levels.

-
- The results of both non-perforating and perforating micro-abrasion tests showed the superior performance of P1-60-15sccm coating. It indicates that although high H values can provide resistance to scratching and/or ploughing, E values should also be low enough (preferentially close to the substrate value) to resist plastic deformation against a counterface.
 - The electrochemical corrosion evaluations revealed an unexpected increase in coating electronegativity with increasing nitrogen content (which might reduce coating/substrate galvanic corrosion effects) – despite the tendency of the corrosion resistance of the coatings to also increase; *i.e.* corrosion current tends also to increase with nitrogen content (except in the 5sccm coating).

Amongst the four AlCuMoMgZrB(N) coatings, P1-60-15sccm seems likely to possess the best combination of wear and corrosion resistance in terms of the best and the second-best performance in micro-abrasion and corrosion tests, respectively.

CHAPTER 8: SUMMARY, CONCLUSION AND RECOMMENDATIONS FOR FUTURE WORK

8.1. Summary and conclusion

Novel AlCuMoMgZrB(N) nanocomposite PVD coatings were prepared by pulsed direct current closed-field unbalanced magnetron sputtering. The development of the coatings contained two stages: production of an optimised base layer for protection of magnesium alloy and modification of the base layer by nitrogen reactive gas incorporation, to produce a hard and wear-resistant nanocomposite coating.

Sixteen AlCuMoMgZrB base layers were initially produced with a wide range of compositions by varying both the depositing positions (*i.e.* four positions in each run) and substrate negative bias (*i.e.* 50 V, 60 V, 75 V and 100 V). By investigation of composition, microstructure, mechanical and electrochemical corrosion properties, the best candidate was selected. Following that, four nanocomposite coatings were produced by adding nitrogen gas with different flow rates (*i.e.* 5 sccm, 10 sccm, 15 sccm and 20 sccm). The coatings were then characterised *via* wear and corrosion tests, to obtain information on the performance.

Stage 1: development of nanocrystalline/glassy base layer

Elemental composition:

- Both deposition position and applied substrate negative bias significantly impacted on the coating elemental compositions.
- The target element sputter yields and substrate resputtering effects for each coating element are important factors which impact on the coating composition and structure.

Phase composition:

- All the layers exhibited a large proportion of amorphous phase constituents.
- The substrate negative bias was observed to promote crystallisation of the layers between 50 V and 75 V; however, crystallisation appears to be suppressed when a substrate negative bias of 100 V was applied.
- P1 and P4 layers are less affected and retain strongly amorphous characteristics compared with P2 and P3 layers, where intermetallic phase peaks could also be observed.

Thickness and morphology:

- The SEM observation of fracture cross-sections and surface morphologies correlates to the XRD analysis, with respect to the applied substrate bias affecting the microstructural evolution.
- Dramatic microstructural evolution with increasing substrate bias was observed in P2 and P3 layers.
- The thickness of the deposited layers is strongly influenced by target element sputter yield, homologous temperatures of involved elements and/or resputtering effects.
- The topic of ion energy spectra of depositing species for each layer was discussed; energetic neutrals appear to play an important role in the microstructural evolution of each layer.

Mechanical properties:

- In general, H values, E values, and H/E ratios of the layers in each deposition run can be sorted by descending order of $P4 > P1 > P2 / P3$. This may be attributed both to their elemental compositions and to the coating microstructure caused by the energetic bombardment effects during the deposition process.

-
- H values, E values, and H/E ratios were found to decrease with increasing substrate negative bias. This is attributed to the increasing energetic bombardment which causes rough surfaces and coarser columnar growth (with the associated voids and defects).

Adhesive strength:

- The results of the scratch-adhesion test are, in general, consistent with those of nanoindentation.
- Good adhesion of the layer to a (compliant) Mg-alloy substrate requires not only a high H/E ratio, but also a low E value (as close as possible to that of the substrate) and a moderately high H value.
- P1-60 and P4-60 layers showed superior substrate adhesion, compared with other layers.
- In particular, the P1-60 layer exhibited a more ductile failure mode than the P4-60 layer, indicating a better performance in terms of withstanding plastic deformations in practical applications.

Electrochemical corrosion properties:

- The electrochemical corrosion properties of the layers P1-60 and P4-60 were evaluated in detail and compared with the WE43 Mg-alloy substrate.
- Both P1-60 and P4-60 layers, showed significantly more positive OCP values, but also much higher polarisation resistance and lower corrosion rates than the WE43 substrate.
- The P1-60 layer showed the superior performance in the tests.
- Therefore, the P1-60 layer was selected as the most suitable base layer for coupling to subsequent nanocomposite PVD hard coating.

TEM analysis:

- P1-60 layer was confirmed to possess a fully amorphous microstructure.

Stage 2: development of nanocomposite coating

- The introduction of nitrogen reactive gas led to the formation of crystalline nitrides and/or intermetallic phase for all coatings.

-
- With increasing nitrogen content, the growth of both nitrides and intermetallic phase were promoted in which the emergence of an MoN phase in the coatings with high nitrogen content may correlate with the corresponding net increase in coating Mo content with increasing nitrogen.
 - Increasing levels of nanocrystallite precipitation were observed with increasing nitrogen content.
 - All coatings displayed a columnar morphology in fracture cross-section and coarser, more open columnar features were observed to be promoted with increasing nitrogen content.
 - A coating surface roughening effect (and associated voids and porosity) was also found with increasing nitrogen content.
 - H and E values (and H/E ratios) were found to increase with increasing nitrogen content in which the P1-60-20sccm coating showed an H/E ratio approaching 0.1 (0.099), however the H/E values may be misleading – due to the development of coating porosity at higher nitrogen levels, which could distort the measured nanoindentation data (particularly the Elastic modulus values).
 - The results of both non-perforating and perforating micro-abrasion tests showed the superior performance of P1-60-15sccm coating. It indicates that although high H values can provide resistance to scratching and/or

ploughing, E values should also be low enough (preferentially close to the substrate value) to resist plastic deformation against a counterface.

- The electrochemical corrosion evaluations revealed an unexpected increase in coating electronegativity with increasing nitrogen content (which might reduce coating/substrate galvanic corrosion effects) – despite the tendency of the corrosion resistance of the coatings to also increase; *i.e.* corrosion current tends also to increase with nitrogen content (except in the 5sccm coating).

Amongst the four AlCuMoMgZrB(N) coatings, P1-60-15sccm seems likely to possess the best combination of wear and corrosion resistance in terms of the best and the second-best performance in micro-abrasion and corrosion tests, respectively.

8.2. Recommendations for future work

Corrosion resistance:

An increase in both base layer and nanocomposite coating thickness is a promising direction to improve the corrosion resistance of the coating system. A total coating thickness of around 7-8 μm or above (i.e. roughly double the thickness of the combined base layer + nanocomposite layer from this study) is probably a minimum requirement to provide full barrier protection – with negligible coating porosity – for the Mg-alloy substrate (based on recent work by Lawal et al. on amorphous Al-alloy PVD coatings for cadmium replacement). The P1-60 base layer is found to possess a good corrosion resistance. In addition, its mechanical properties are close to the underlying magnesium alloy substrate. Thus, the risk of excessive internal stress formed within the as-deposited coating is low. Therefore, the as-deposited coating can readily possess a high thickness, while achieving a dense microstructure.

Another direction is to deposit the AlCuMoMgZrB(N) nanocomposite coatings with lower nitrogen flow rates within the range of 0-10 sccm (ie. at the lower end of the range in this work). As the P1-60-5sccm coating shows a superior corrosion resistance compared with those deposited with

higher introduced nitrogen flow rates, there is a scope to explore a coating with further improved corrosion resistance if the introduced nitrogen flow rate is reduced.

Wear resistance:

Due to the load limitation in the laboratory (*i.e.* not possible to maintain stable push and pull forces if the applied load is lower than 5N), the sliding wear resistance of the AlCuMoMgZrB(N) coatings could not be evaluated reliably. The maximum load allowed to perform the test is approximately calculated as 1N if using an aluminium ball with a diameter of 10 mm against the coating surface. To evaluate the potential of coated magnesium alloys for tribological component applications, sliding wear tests (e.g. reciprocating-sliding or pin-on-disc wear tests) are necessary to be carried out.

Microstructural study:

The phase composition in the four AlCuMoMgZrB(N) nanocomposite coatings is complicated, involving a proportion of ultrafine nanocrystalline precipitates, whose precise composition and structure is difficult to

determine – even using SAED and HRTEM imaging. The majority of the nanocrystallites are expected to be intermetallic phases when the introduced nitrogen flow rate is low (*e.g.* 5 sccm), while gradually evolving to predominantly ceramic nitride phases with increasing nitrogen gas flow rate for coating deposition. This evolution is believed to lead to their different behaviours in electrochemical corrosion evaluations. An insightful microstructural investigation is required, to confirm the precipitates in each coating.

Thermal stability:

With the introduction of refractory elements (i.e. Zr, B and Mo, which possess high melting temperatures of 2125K, 2349K and 2883K, respectively), the AlCuMoMgZrB(N) nanocomposite coating structure can be expected to remain stable at a higher temperature than that at which uncoated WE43 magnesium alloys would typically be used (i.e. 250-300 °C maximum) due to the increase in homologous temperature. Therefore, the thermal stability of the AlCuMoMgZrB(N) nanocomposite coatings is a worthwhile research direction. Moreover, the homologous temperature will be further increased if the content of these elements was increased. That means, if the primary aim of the coating is to provide a

thermally stable barrier layer for the underlying magnesium alloys, the base (coupling) layer deposited at P4 position is promising due to its high content of Mo, Zr and Cu (with the latter, $T_m \sim 1356\text{K}$; still a considerably higher melting temperature than Mg).

Coating design:

The mixture of six elements (seven, if including N) in the present coating system is complicated (as required, to promote amorphisation). This however makes it very difficult to correlate wear and corrosion performance with the composition and microstructure (*i.e.* too many variables). So, if the number of added elements could be reduced, this would simplify the subsequent analysis and possibly improve the understanding (and the repeatability) of the coating process. Meanwhile, the basic design concept remains valid: firstly, to deposit a compliant base layer of moderate hardness – preferentially with amorphous microstructure – and, subsequently, to produce a nanocomposite coating on the top by introducing nitrogen reactive gas.

Amongst the six sputter target elements in the present coating system, Mg and Zr are found to not only possess low elastic modulus (44 GPa and 68 GPa, respectively), but also show a promising tendency to produce glassy

microstructure.

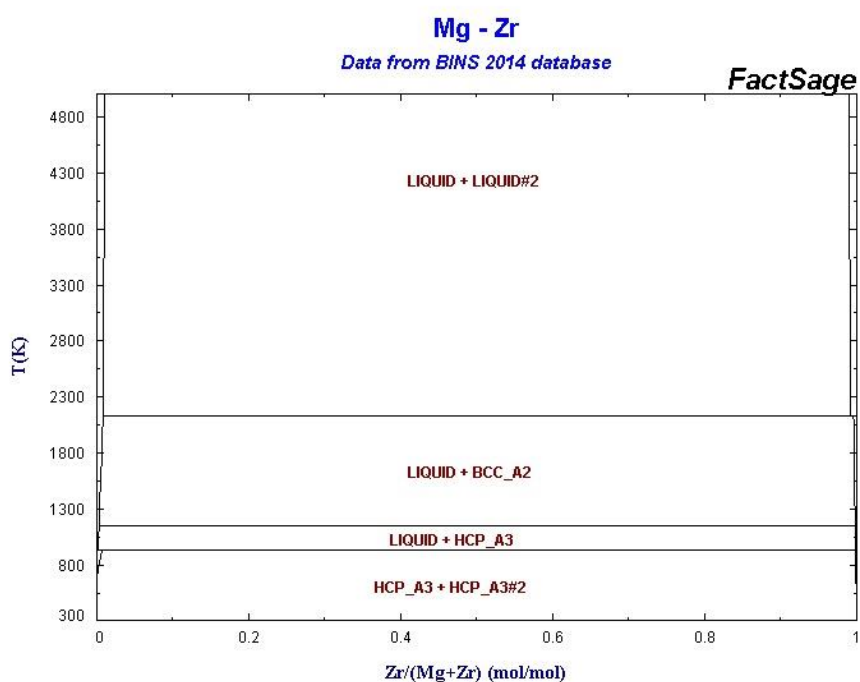


Figure 8.1 Mg-Zr binary phase diagram

As **Figure 8.1** shows, two types of hcp structure are observed to be present – without any (brittle) intermetallic phase formed (which is the current underlying problem that this work set out to address) – if mixing Mg and Zr at a temperature close to the depositing temperature in the chamber. The rapid cooling rate achieved in the PVD machine is very likely to lead to the mutual solid solution of the hcp structures and (particularly if a third, immiscible element, such as copper, is added) an overall amorphisation effect. As a result, two or three elements may be sufficient to achieve the amorphous metal base layer or ceramic nanocomposite top layer (due to the strong nitride-forming ability of Zr) coating architecture required to

functionalise Mg-alloy substrates for wear and corrosion applications on moving parts for applications in transport, energy and other industrial sectors. Further exploration of Mg-Zr-(Me) based ternary/quaternary nitride (and/or oxide) based PVD coating systems is therefore a topic worthy of future investigation.

CHAPTER 9: REFERENCES

1. Stephen Abela, *Protective coatings for magnesium alloys*. 2011: INTECH Open Access Publisher.
2. Jochen M Schneider, Suzanne Rohde, William D Sproul, and Allan Matthews, *Recent developments in plasma assisted physical vapour deposition*. Journal of Physics D: Applied Physics, 2000. **33**(18): p. R173.
3. Guosong Wu, Xiaoqin Zeng, and Guangyin Yuan, *Growth and corrosion of aluminum PVD-coating on AZ31 magnesium alloy*. Materials Letters, 2008. **62**(28): p. 4325-4327.
4. Guosong Wu, Xiaoqin Zeng, Geyang Li, Shoushan Yao, and Xuemin Wang, *Preparation and characterization of ceramic/metal duplex coatings deposited on AZ31 magnesium alloy by multi-magnetron sputtering*. Materials Letters, 2006. **60**(5): p. 674-678.
5. Guosong Wu, Wei Dai, He Zheng, and Aiyang Wang, *Improving wear resistance and corrosion resistance of AZ31 magnesium alloy by DLC/AlN/Al coating*. Surface and Coatings Technology, 2010. **205**(7): p. 2067-2073.
6. Liu Hongxi, Xu Qian, Xiong Damin, Lin Bo, and Meng Chunlei, *Microstructure and corrosion resistance of AZ91D magnesium alloy treated by hybrid ion implantation and heat treatment*. Vacuum, 2013. **89**: p. 233-237.
7. H Hoche, C Blawert, E Broszeit, and C Berger, *Galvanic corrosion properties of differently PVD-treated magnesium die cast alloy AZ91*. Surface and Coatings Technology, 2005. **193**(1): p. 223-229.
8. Holger Hoche, Stefan Groß, Torsten Troßmann, Juergen Schmidt, and Matthias Oechsner, *PVD coating and substrate pretreatment concepts for magnesium alloys by multinary coatings based on Ti (X) N*. Surface and Coatings Technology, 2013. **228**: p. S336-S341.
9. Hikmet Altun and Sadri Sen, *The effect of PVD coatings on the wear behaviour of magnesium alloys*. Materials Characterization, 2007. **58**(10): p. 917-921.
10. A. Leyland and A. Matthews, *On the significance of the H/E ratio in wear control: a nanocomposite coating approach to optimised tribological behaviour*. Wear, 2000. **246**(1-2): p. 1-11.
11. A. Leyland and A. Matthews, *Design criteria for wear-resistant nanostructured and glassy-metal coatings*. Surface and Coatings Technology, 2004. **177-178**(0): p. 317-324.
12. *State of the Climate: Global Analysis for Annual 2015*, in NOAA National Centers for Environmental Information. 2016.
13. *Status of Ratification of the Kyoto Protocol*. 2012: UNFCCC Homepage.
14. H. Friedrich and S. Schumann, *Research for a "new age of magnesium" in the automotive industry*. Journal of Materials Processing Technology, 2001. **117**(3): p. 276-281.
15. Jeremy J. Michalek, Panos Y. Papalambros, and Steven J. Skerlos, *A Study of Fuel Efficiency and Emission Policy Impact on Optimal Vehicle Design Decisions*. Journal of Mechanical Design, 2005. **126**(6): p. 1062-1070.
16. M Medraj and A Parvez, *Analyse the importance of Magnesium-aluminium-strontium alloys for more fuel-efficient automobiles*. 2007, Automotive.

-
17. G. L. Makar and J. Kruger, *Corrosion of magnesium*. International Materials Reviews, 1993. **38**(3): p. 138-153.
 18. Mustafa Kemal Kulekci, *Magnesium and its alloys applications in automotive industry*. The International Journal of Advanced Manufacturing Technology, 2008. **39**(9-10): p. 851-865.
 19. G Davies, *Magnesium. Materials for automotive bodies*. Elsevier, G. London, 2003. **91**: p. 158-159.
 20. Yo Kojima. *Platform science and technology for advanced magnesium alloys*. in *Materials Science Forum*. 2000. : Trans Tech Publ.
 21. Chao-Chi Jain and Chun-Hao Koo, *Creep and corrosion properties of the extruded magnesium alloy containing rare earth*. Materials transactions, 2007. **48**(2): p. 265-272.
 22. C Blawert, N Hort, and KU Kainer, *Automotive applications of magnesium and its alloys*. Trans. Indian Inst. Met, 2004. **57**(4): p. 397-408.
 23. D Eliezer, E Aghion, and FH Sam Froes, *Magnesium science, technology and applications*. Advanced Performance Materials, 1998. **5**(3): p. 201-212.
 24. *MatWeb, Your Source for Materials Information*. 2016 ; Available from: <http://www.matweb.com/index.aspx>.
 25. A. S. M. International Handbook Committee, *ASM Handbook, Volume 02 - Properties and Selection: Nonferrous Alloys and Special-Purpose Materials*. ASM International.
 26. S. Yu Kondrat'ev, G. Ya Yaroslavskii, and B. S. Chaikovskii, *Classification of high-damping metallic materials*. Strength of Materials, 1986. **18**(10): p. 1325-1329.
 27. A Froats, TK Aune, D Hawke, W Unsworth, and J Hillis, *Corrosion of magnesium and magnesium alloys*. ASM Handbook., 1987. **13**: p. 740-754.
 28. R. W. Schutz and L. C. Covington, *Effect of Oxide Films on the Corrosion Resistance of Titanium*. Corrosion, 1981. **37**(10): p. 585-591.
 29. G. Song and A. Atrens, *Recent Insights into the Mechanism of Magnesium Corrosion and Research Suggestions*. Advanced Engineering Materials, 2007. **9**(3): p. 177-183.
 30. I.J. Polmear, *Light alloys: metallurgy of the light metals*. 1995: J. Wiley & Sons.
 31. Nikon Danilovich Tomashov, *Theory of corrosion and protection of metals*. 1966, 672 P. THE MACMILLAN COMPANY, 60 FIFTH AVENUE, NEW YORK 10011, 1965.
 32. Mihriban O Pekguleryuz and A Arslan Kaya, *Creep resistant magnesium alloys for powertrain applications*. Advanced Engineering Materials, 2003. **5**(12): p. 866-878.
 33. Mihriban O Pekguleryuz, Eric Baril, Pierre Labelle, and Donald Argo, *Creep resistant Mg-Al-Sr alloys*. Journal of advanced materials, 2003. **35**(3): p. 32-38.
 34. E Aghion, B Bronfin, F Von Buch, S Schumann, and H Friedrich, *Newly developed magnesium alloys for powertrain applications*. The Journal of The Minerals, Metals & Materials Society, 2003. **55**(11): p. 30-33.
 35. Eric Baril, Pierre Labelle, and Mihriban Pekguleryuz, *Elevated temperature Mg-Al-Sr: creep resistance, mechanical properties, and microstructure*. The Journal of The Minerals, Metals & Materials Society, 2003. **55**(11): p. 34-39.
 36. H Dieringa and KU Kainer, *Magnesium—der Zukunftswerkstoff für die Automobilindustrie?* Materialwissenschaft und Werkstofftechnik, 2007. **38**(2): p. 91-96.
 37. S Schuman. *The paths and strategies for increased magnesium application in vehicles*. in *Mat Sci Forum*. 2005.

-
38. G Davies, *Magnesium. Materials for automotive bodies*. vol, 2003. **91**: p. 1327.
 39. GL Makar and J Kruger, *Corrosion studies of rapidly solidified magnesium alloys*. Journal of the Electrochemical Society, 1990. **137**(2): p. 414-421.
 40. G. L. Makar and J. Kruger, *Corrosion Studies of Rapidly Solidified Magnesium Alloys*. Journal of The Electrochemical Society, 1990. **137**(2): p. 414-421.
 41. JE Gray and Ben Luan, *Protective coatings on magnesium and its alloys—a critical review*. Journal of alloys and compounds, 2002. **336**(1): p. 88-113.
 42. JB Mohler, *High Speed Electroplating*. Metal Finishing, 1974. **72**(7): p. 29-33.
 43. Patrick L Hagans and CM Haas, *Chromate conversion coatings*. ASM International, Member/Customer Service Center, Materials Park, OH 44073-0002, USA, 1994., 1994: p. 405-411.
 44. CK Mittal, *Chemical conversion and anodized coatings*. 1995.
 45. A Simaranov, AI Marshakov, and Yu N Mikhailovskii, *The composition and protective properties of chromate conversion coatings on magnesium*. Protection of metals, 1992. **28**(5): p. 576-580.
 46. Carsten Blawert, Wolfgang Dietzel, Edward Ghali, and Guangling Song, *Anodizing treatments for magnesium alloys and their effect on corrosion resistance in various environments*. Advanced Engineering Materials, 2006. **8**(6): p. 511-533.
 47. AK Sharma, R Uma Rani, and K Giri, *Studies on anodization of magnesium alloy for thermal control applications*. Metal Finishing, 1997. **95**(3): p. 43-51.
 48. ASM International Handbook Committee, *ASM handbook: Surface engineering*. Vol. 5. 1994: ASM International.
 49. Clarence E Habermann and David S Garrett, *Anticorrosive coated rectifier metals and their alloys*. 1987, Google Patents.
 50. P Ross, J MacCulloch, C Clapp, and R Esdaile, *The mechanical properties of anodized magnesium die castings*. 1999, SAE Technical Paper.
 51. Sachiko Ono, *Surface phenomena and protective film growth on magnesium and magnesium alloys*. Metallurgical Science and Tecnology, 2013. **16**(2).
 52. H Umehara, M Takaya, and T Itoh, *Corrosion resistance of the die casting AZ91D magnesium alloys with paint finishing*. Aluminium, 1999. **75**(7-8): p. 634-641.
 53. James E Hillis, *Surface engineering of magnesium alloys*. ASM International, Member/Customer Service Center, Materials Park, OH 44073-0002, USA, 1994., 1994: p. 819-834.
 54. Gordon P Bierwagen, *Reflections on corrosion control by organic coatings*. Progress in organic coatings, 1996. **28**(1): p. 43-48.
 55. Guangling Song and Andrej Atrens, *Understanding magnesium corrosion—a framework for improved alloy performance*. Advanced engineering materials, 2003. **5**(12): p. 837-858.
 56. AK Sharma, *Electrodeposition of Gold on Magnesium--Lithium Alloys*. Met. Finish., 1988. **86**(12): p. 33-34.
 57. AK Sharma, *Gold plating on magnesium-lithium alloys*. Metal finishing, 1991. **89**(7): p. 16-17.
 58. I Rajagopal, KS Rajam, and SR Rajoagopalan, *Plating on magnesium alloy*. Metal finishing, 1990. **88**(12): p. 43-47.

-
59. John S. Colligon, *Chapter 9 Physical vapor deposition*, in *Pergamon Materials Series*, C. Suryanarayana, Editor. 1999, Pergamon. p. 225-253.
60. D. M. Mattox, *Handbook of physical vapor deposition (PVD) processing : film formation, adhesion, surface preparation and contamination control*. 1998, Park Ridge, N.J.: Noyes Publications. xxvii, 917 p.
61. Donald M. Mattox, *Physical vapor deposition (PVD) processes*. *Metal Finishing*, 2002. **100**, **Supplement 1(0)**: p. 394-408.
62. H. K. Pulker, *Coatings on glass substrates*. *Thin Solid Films*, 1981. **77**(1-3): p. 203-212.
63. J.R. Pierce, *Theory and design of electron beams*. 1954: Van Nostrand.
64. Von S. Schiller, U. Heisig, M. Neumann, and G. Beister, *Processing and instrumentation in PVD techniques*. *Vakuum-Technik*, 1986. **35**(2): p. 35-54.
65. R. L. Boxman, David M. Sanders, and Philip J. Martin. *Handbook of vacuum arc science and technology fundamentals and applications*. 1995 ; Available from:
<http://www.engineeringvillage.com/controller/servlet/OpenURL?genre=book&isbn=9780815513759>.
66. K. S. SreeHarsha. *Principles of physical vapor deposition of thin films*. 2006 ; Available from:
<http://www.engineeringvillage.com/controller/servlet/OpenURL?genre=book&isbn=9780080446998>.
67. Jiang Xu, ZheYuan Chen, Jie Tao, ShuYun Jiang, ZiLi Liu, and Zhong Xu, *Corrosion behavior of amorphous/nanocrystalline Al-Cr-Fe film deposited by double glow plasmas technique*. *Science in China Series E: Technological Sciences*, 2009. **52**(5): p. 1225-1233.
68. M Fenker, M Balzer, H Kappl, and O Banakh, *Some properties of (Ti, Mg) N thin films deposited by reactive dc magnetron sputtering*. *Surface and Coatings Technology*, 2005. **200**(1): p. 227-231.
69. Holger Hoche, Stefan Groß, and Matthias Oechsner, *Development of new PVD coatings for magnesium alloys with improved corrosion properties*. *Surface and Coatings Technology*, 2014. **259**: p. 102-108.
70. Holger Hoche, Juergen Schmidt, Stefan Groß, Torsten Troßmann, and Christina Berger, *PVD coating and substrate pretreatment concepts for corrosion and wear protection of magnesium alloys*. *Surface and Coatings Technology*, 2011. **205**: p. S145-S150.
71. H. Dong and T. Bell, *Designer surfaces for titanium components*. *Industrial Lubrication and Tribology*, 1998. **50**(6): p. 282-289.
72. H. Dong, A. Bloyce, P. H. Morton, and T. Bell, *Surface engineering to improve tribological performance of Ti-6Al-4V*. *Surface Engineering*, 1997. **13**(5): p. 402-406.
73. K. Marchev, C. V. Cooper, J. T. Blucher, and B. C. Giessen, *Conditions for the formation of a martensitic single-phase compound layer in ion-nitrided 316L austenitic stainless steel*. *Surface and Coatings Technology*, 1998. **99**(3): p. 225-228.
74. K. Ichii, K. Fujimura, and T. Takase, *Structure of the ion-nitrided layer of 18-8 stainless steel*. *Technol. Rep. Kansai Univ.*, 1986(27): p. 135-144.
75. C. Suman, in *Society of Automotive Engineers*. 1991, SAE Technical Paper: Warrendale, PA.
76. A. Matthews and D. G. Teer, *Deposition of Ti-N compounds by thermionically assisted triode reactive ion plating*. *Thin Solid Films*, 1980. **72**(3): p. 541-549.

-
77. K.L. Chopra, *Thin film phenomena*. 1969: McGraw-Hill.
 78. H. Randhawa, *Review of plasma-assisted deposition processes*. *Thin Solid Films*, 1991. **196**(2): p. 329-349.
 79. William D. Sproul, *New Routes in the Preparation of Mechanically Hard Films*. Science, 1996. **273**(5277): p. 889-892.
 80. J. Singh and D. E. Wolfe, *Review Nano and macro-structured component fabrication by electron beam-physical vapor deposition (EB-PVD)*. *Journal of Materials Science*, 2005. **40**(1): p. 1-26.
 81. J. T. Prater and E. L. Courtright, *Ceramic thermal barrier coatings with improved corrosion resistance*. *Surface and Coatings Technology*, 1987. **32**(1-4): p. 389-397.
 82. Curt H. Liebert and Francis S. Stepka, *CERAMIC THERMAL-BARRIER COATINGS FOR COOLED TURBINES*. *Journal of Aircraft*, 1977. **14**(5): p. 487-493.
 83. F. C. Toriz, A. B. Thakker, and S. K. Gupta, *Flight service evaluation of thermal barrier coatings by physical vapor deposition at 5200 H*. *Surface and Coatings Technology*, 1989. **39-40, Part 1**(0): p. 161-172.
 84. Thomas E. Strangman, *Thermal barrier coatings for turbine airfoils*. *Thin Solid Films*, 1985. **127**(1-2): p. 93-106.
 85. E. Lugscheider, C. Barimani, C. Wolff, S. Guerreiro, and G. Doepper, *Comparison of the structure of PVD-thin films deposited with different deposition energies*. *Surface and Coatings Technology*, 1996. **86-87, Part 1**(0): p. 177-183.
 86. James K. Hirvonen, *Ion beam assisted thin film deposition*. *Materials Science Reports*, 1991. **6**(6): p. 215-274.
 87. Harold R. Kaufman, *Broad-beam ion sources: Present status and future directions*. *Journal of Vacuum Science & Technology A: Vacuum, Surfaces, and Films*, 1986. **4**(3): p. 764-771.
 88. Burkhard Juttner, *Characterization of the Cathode Spot*. *Plasma Science, IEEE Transactions on*, 1987. **15**(5): p. 474-480.
 89. Ian G. Brown, *CATHODIC ARC DEPOSITION OF FILMS*. *Annual Review of Materials Science*, 1998. **28**(1): p. 243-269.
 90. David M. Sanders, *Review of ion-based coating processes derived from the cathodic arc*. *Journal of Vacuum Science & Technology A: Vacuum, Surfaces, and Films*, 1989. **7**(3): p. 2339-2345.
 91. H. Randhawa, *Cathodic arc plasma deposition technology*. *Thin Solid Films*, 1988. **167**(1-2): p. 175-186.
 92. P. D. Swift, *Macroparticles in films deposited by steered cathodic arc*. *J. Phys. D, Appl. Phys*, 1996. **29**(7): p. 2025.
 93. H. Takikawa R. Miyano, T. Sakakibara and Y. Suzuki, *Retrograde motion velocity of graphite cathode spot in vacuum arc deposition apparatus*. *Trans. Inst. Electr. Eng. Jpn.*, 1994. **A-114**: p. 117.
 94. R. L. Boxman and S. Goldsmith, *Principles and applications of vacuum arc coatings*. *Plasma Science, IEEE Transactions on*, 1989. **17**(5): p. 705-712.
 95. S. Anders, A. Anders, Yu Kin Man, X. Y. Yao, and I. G. Brown, *On the macroparticle flux from vacuum arc cathode spots*. *Plasma Science, IEEE Transactions on*, 1993. **21**(5): p. 440-446.

-
96. V. A. Belous, I. I. Aksenov, V. V. Vasil'ev, Y. Y. Volkov and V. E. Strel'nitskij, *A rectilinear plasma filtering system for vacuum-arc deposition of diamond-like carbon coatings*. *Diam. Relat. Mater.*, 1999. **8**: p. 468.
97. Hirofumi Takikawa, Nobuhide Miyakawa, and Tateki Sakakibara, *Development of shielded cathodic arc deposition with a superconductor shield*. *Surface and Coatings Technology*, 2002. **171**(1–3): p. 162-166.
98. I.I. Aksenov, V.A. Belous, V.G. Padalka, and V.M. Khoroshikh, *Transport of plasma streams in a curvilinear plasma-optics system*. *Journal Name: Sov. J. Plasma Phys. (Engl. Transl.); (United States); Journal Volume: 4:4, 1978: p. Medium: X; Size: Pages: 425-428.*
99. S. Fallabella D.A. Baldwin, *Deposition processes utilizing a new filtered cathodic arc source*, in *Proc. of the 38th Annual Techn. Conf.* 1995, Society of Vacuum Coaters: Chicago. p. PP. 309–316.
100. I. I. Aksenov, V. A. Belous, V. V. Vasil'ev, Yu Ya Volkov, and V. E. Strel'nitskij, *A rectilinear plasma filtering system for vacuum-arc deposition of diamond-like carbon coatings*. *Diamond and Related Materials*, 1999. **8**(2–5): p. 468-471.
101. J. Storer, J. E. Galvin, and I. G. Brown, *Transport of vacuum arc plasma through straight and curved magnetic ducts*. *Journal of Applied Physics*, 1989. **66**(11): p. 5245-5250.
102. M. M. Bilek Marcela and Anders André, *Designing advanced filters for macroparticle removal from cathodic arc plasmas*. *Plasma Sources Science and Technology*, 1999. **8**(3): p. 488.
103. Schülke Thomas and AndréAnders, *Velocity distribution of carbon macroparticles generated by pulsed vacuum arcs*. *Plasma Sources Science and Technology*, 1999. **8**(4): p. 567.
104. R. Behrisch and W. Eckstein, *Sputtering by Particle Bombardment: Experiments and Computer Calculations from Threshold to MeV Energies*. 2007: Springer.
105. W.D. Sproul and K.O. Legg, *Opportunities for Innovation: Advanced Surface Engineering*. 1994: Technomic.
106. P. J. Kelly and R. D. Arnell, *Magnetron sputtering: a review of recent developments and applications*. *Vacuum*, 2000. **56**(3): p. 159-172.
107. J. Musil and S. Kadlec, *Reactive sputtering of TiN films at large substrate to target distances*. *Vacuum*, 1990. **40**(5): p. 435-444.
108. N. Savvides and B. Window, *Unbalanced magnetron ion-assisted deposition and property modification of thin films*. *Journal of Vacuum Science & Technology A: Vacuum, Surfaces, and Films*, 1986. **4**(3): p. 504-508.
109. P. J. Kelly and R. D. Arnell, *The influence of magnetron configuration on ion current density and deposition rate in a dual unbalanced magnetron sputtering system*. *Surface and Coatings Technology*, 1998. **108–109**(0): p. 317-322.
110. William D. Sproul, Paul J. Rudnik, Michael E. Graham, and Suzanne L. Rohde, *High rate reactive sputtering in an opposed cathode closed-field unbalanced magnetron sputtering system*. *Surface and Coatings Technology*, 1990. **43–44, Part 1**(0): p. 270-278.
111. Kiyotaka Wasa, Hideaki Adachi, and Makoto Kitabatake, *Thin film materials technology : sputtering of compound materials*. 2004, Norwich, NY [u.a.]: William Andrew Pub [u.a.].
112. M. Scherer, J. Schmitt, R. Latz, and M. Schanz. *Reactive alternating current magnetron sputtering of dielectric layers*. 1992. Seattle, Washington (USA): AVS.

-
113. David A. Glocker, *Influence of the plasma on substrate heating during low-frequency reactive sputtering of AlN*. Journal of Vacuum Science & Technology A: Vacuum, Surfaces, and Films, 1993. **11**(6): p. 2989-2993.
114. P. J. Kelly, O. A. Abu-Zeid, R. D. Arnell, and J. Tong, *The deposition of aluminium oxide coatings by reactive unbalanced magnetron sputtering*. Surface and Coatings Technology, 1996. **86–87, Part 1**(0): p. 28-32.
115. W. D. Sproul, M. E. Graham, M. S. Wong, S. Lopez, D. Li, and R. A. Scholl. *Reactive direct current magnetron sputtering of aluminum oxide coatings*. 1995. Denver, Colorado (USA): AVS.
116. P. J. Kelly and R. D. Arnell, *Development of a novel structure zone model relating to the closed-field unbalanced magnetron sputtering system*. Journal of Vacuum Science & Technology A: Vacuum, Surfaces, and Films, 1998. **16**(5): p. 2858-2869.
117. Christian Mitterer, *Borides in Thin Film Technology*. Journal of Solid State Chemistry, 1997. **133**(1): p. 279-291.
118. Kenneth Holmberg and Allan Matthews, *COATINGS TRIBOLOGY Properties, Mechanisms*. Tribology and interface engineering series, 2009. **56**(1): p. ALL-ALL.
119. C. Donnet, *Recent progress on the tribology of doped diamond-like and carbon alloy coatings: a review*. Surface and Coatings Technology, 1998. **100**: p. 180-186.
120. C. Suryanarayana and C.C. Koch, *Nanocrystalline materials – Current research and future directions*. Hyperfine Interactions, 2000. **130**(1): p. 5-44.
121. Akihisa Inoue, *Bulk amorphous and nanocrystalline alloys with high functional properties*. Materials Science and Engineering: A, 2001. **304–306**(0): p. 1-10.
122. Akihisa Inoue, *Stabilization of metallic supercooled liquid and bulk amorphous alloys*. Acta Materialia, 2000. **48**(1): p. 279-306.
123. A. A. Voevodin, J. M. Schneider, C. Rebholz, and A. Matthews, *Multilayer composite ceramic-metal-DLC coatings for sliding wear applications*. Tribology International, 1996. **29**(7): p. 559-570.
124. S. Vepřek, *Conventional and new approaches towards the design of novel superhard materials*. Surface and Coatings Technology, 1997. **97**(1–3): p. 15-22.
125. D. Turnbull and J. C. Fisher, *Rate of nucleation in condensed systems*. The Journal of Chemical Physics, 1949. **17**(1): p. 71-73.
126. M. Audronis, O. Jimenez, A. Leyland, and A. Matthews, *The morphology and structure of PVD ZrN–Cu thin films*. Journal of Physics D: Applied Physics, 2009. **42**(8): p. 085308.
127. D. J. Li, M. X. Wang, and J. J. Zhang, *Structural and mechanical responses of (Zr,Al)N/ZrB₂ superlattice coatings to elevated-temperature annealing*. Materials Science and Engineering: A, 2006. **423**(1–2): p. 116-120.
128. R Khosrshahi. *The microstructure and creep of as-cast and extruded WE 54*. in *Proceedings of the Third International Magnesium Conference*. 1996.
129. GW Lorimer, *Structure-property relationships in cast magnesium alloys*. Magnesium technology, 1987: p. 47-53.
130. JF Nie, XL Xiao, CP Luo, and BC Muddle, *Characterisation of precipitate phases in magnesium alloys using electron microdiffraction*. Micron, 2001. **32**(8): p. 857-863.

-
131. T Rzychoń and A Kielbus, *Microstructure of WE43 casting magnesium alloys*. Journal of Achievements in Materials and Manufacturing Engineering, 2007. **21**(1): p. 31-34.
 132. Tapan Kumar Rout, *Nanolayered oxide on a steel surface reduces surface reactivity: Evaluation by glow discharge optical emission spectroscopy (GDOES)*. Scripta materialia, 2007. **56**(7): p. 573-576.
 133. Arne Bengtson, Anders Eklund, Martin Lundholm, and Ante Saric, *Further improvements in calibration techniques for depth profiling with glow discharge optical emission spectrometry*. Journal of Analytical Atomic Spectrometry, 1990. **5**(6): p. 563-567.
 134. Shuangbiao Liu and Q. Jane Wang, *Determination of Young's modulus and Poisson's ratio for coatings*. Surface and Coatings Technology, 2007. **201**(14): p. 6470-6477.
 135. T. Chudoba, N. Schwarzer, and F. Richter, *Steps towards a mechanical modeling of layered systems*. Surface and Coatings Technology, 2002. **154**(2-3): p. 140-151.
 136. MM Stack and Mathew Mathew, *Micro-abrasion transitions of metallic materials*. Wear, 2003. **255**(1): p. 14-22.
 137. KL Rutherford and IM Hutchings, *A micro-abrasive wear test, with particular application to coated systems*. Surface and Coatings Technology, 1996. **79**(1): p. 231-239.
 138. JCA Batista, MC Joseph, C Godoy, and A Matthews, *Micro-abrasion wear testing of PVD TiN coatings on untreated and plasma nitrided AISI H13 steel*. Wear, 2001. **249**(10): p. 971-979.
 139. V Imbeni, C Martini, E Lanzoni, G Poli, and IM Hutchings, *Tribological behaviour of multi-layered PVD nitride coatings*. Wear, 2001. **251**(1): p. 997-1002.
 140. A Dorner, C Schürer, G Reisel, G Irmer, O Seidel, and E Müller, *Diamond-like carbon-coated Ti6Al4V: influence of the coating thickness on the structure and the abrasive wear resistance*. Wear, 2001. **249**(5): p. 489-497.
 141. R. I. Trezona, D. N. Allsopp, and I. M. Hutchings, *Transitions between two-body and three-body abrasive wear: influence of test conditions in the microscale abrasive wear test*. Wear, 1999. **225-229, Part 1**: p. 205-214.
 142. K. Bose and R. J. K. Wood, *Optimum tests conditions for attaining uniform rolling abrasion in ball cratering tests on hard coatings*. Wear, 2005. **258**(1-4): p. 322-332.
 143. K. Adachi and I. M. Hutchings, *Sensitivity of wear rates in the micro-scale abrasion test to test conditions and material hardness*. Wear, 2005. **258**(1-4): p. 318-321.
 144. D. N. Allsopp, R. I. Trezona, and I. M. Hutchings, *The effects of ball surface condition in the micro - scale abrasive wear test*. Tribology Letters, 1998. **5**(4): p. 259-264.
 145. K. Adachi and I. M. Hutchings, *Wear-mode mapping for the micro-scale abrasion test*. Wear, 2003. **255**(1-6): p. 23-29.
 146. Y. Kusano, K. Van Acker, and I. M. Hutchings, *Methods of data analysis for the micro-scale abrasion test on coated substrates*. Surface and Coatings Technology, 2004. **183**(2-3): p. 312-327.
 147. K. L. Rutherford and I. M. Hutchings, *Theory and Application of a Micro-Scale Abrasive Wear Test*. Journal of Testing and Evaluation, 1997. **25**(2): p. 250-260.
 148. K. L. Rutherford and I. M. Hutchings, *A micro-abrasive wear test, with particular application to coated systems*. Surface and Coatings Technology, 1996. **79**(1): p. 231-239.

-
149. MP Seah, CA Clifford, FM Green, and IS Gilmore, *An accurate semi - empirical equation for sputtering yields I: for argon ions*. Surface and interface analysis, 2005. **37**(5): p. 444-458.
 150. YH Cheng, BK Tay, SP Lau, X Shi, and HS Tan, *Influence of substrate bias on the microstructure and internal stress in Cu films deposited by filtered cathodic vacuum arc*. Journal of Vacuum Science & Technology A, 2001. **19**(5): p. 2102-2108.
 151. J.E. Houston and J.E. Uhl, *Characterization of the ionic species incident on the cathode in a glow discharge* in *Other Information: UNCL. Orig. Receipt Date: 31-DEC-71*. 1971. p. Medium: X; Size: Pages: 36.
 152. ON Senkov and JM Scott, *Specific criteria for selection of alloy compositions for bulk metallic glasses*. Scripta materialia, 2004. **50**(4): p. 449-452.
 153. J Lawal, P Kiryukhantsev-Korneev, A Matthews, and A Leyland, *Mechanical properties and abrasive wear behaviour of Al-based PVD amorphous/nanostructured coatings*. Surface and Coatings Technology, 2017. **310**: p. 59-69.
 154. AG Dirks and HJ Leamy, *Columnar microstructure in vapor-deposited thin films*. Thin solid films, 1977. **47**(3): p. 219-233.
 155. J. A. Thornton, *High rate thick film growth*. Annual Review of Materials Science, 1977. **7**: p. 239-260.
 156. P. B. Barna and M. Adamik, *Fundamental structure forming phenomena of polycrystalline films and the structure zone models*. Thin Solid Films, 1998. **317**(1–2): p. 27-33.
 157. D. Henderson, M. H. Brodsky, and P. Chaudhari, *Simulation of structural anisotropy and void formation in amorphous thin films*. Applied Physics Letters, 1974. **25**(11): p. 641-643.
 158. I. Petrov, P. B. Barna, L. Hultman, and J. E. Greene, *Microstructural evolution during film growth*. Journal of Vacuum Science & Technology A, 2003. **21**(5): p. S117-S128.
 159. Y. T. Pei, D. Galvan, and J. Th M. De Hosson, *Nanostructure and properties of TiC/a-C:H composite coatings*. Acta Materialia, 2005. **53**(17): p. 4505-4521.
 160. Y. T. Pei, D. Galvan, J. Th M. De Hosson, and C. Strondl, *Advanced TiC/a-C:H nanocomposite coatings deposited by magnetron sputtering*. Journal of the European Ceramic Society, 2006. **26**(4–5): p. 565-570.
 161. A Bendavid, PJ Martin, RP Netterfield, and TJ Kinder, *The properties of TiN films deposited by filtered arc evaporation*. Surface and Coatings Technology, 1994. **70**(1): p. 97-106.
 162. Brian W. Dodson, *Atomic-Scale Modeling of Low-Energy Ion-Solid Processes*. MRS Online Proceedings Library, 1988. **128**: p. null-null.
 163. Jyh-Wei Lee, Shih-Kang Tien, and Yu-Chu Kuo, *The effects of pulse frequency and substrate bias to the mechanical properties of CrN coatings deposited by pulsed DC magnetron sputtering*. Thin Solid Films, 2006. **494**(1–2): p. 161-167.
 164. WD Davis and TA Vanderslice, *Ion energies at the cathode of a glow discharge*. Physical Review, 1963. **131**(1): p. 219.
 165. J. Richards, *Energies of particles at the cathode of a glow discharge*. Vacuum, 1984. **34**(5): p. 559-562.
 166. K. S. Fancey and A. Matthews, *Some fundamental aspects of glow discharges in plasma-assisted processes*. Surface and Coatings Technology, 1987. **33**: p. 17-29.
 167. Brian Chapman, *Glow discharge processes: sputtering and plasma etching*. 1980: Wiley-Interscience.

-
168. P Saulnier, A Debhi, and J Machet, *Ion energy distribution in triode ion plating*. Vacuum, 1984. **34**(8): p. 765-769.
169. H Ljungcrantz, M Odén, L Hultman, JE Greene, and J - E Sundgren, *Nanoindentation studies of single - crystal (001) -, (011) -, and (111) - oriented TiN layers on MgO*. Journal of applied physics, 1996. **80**(12): p. 6725-6733.
170. Magnus Odén, Claes Ericsson, Greger Håkansson, and Henrik Ljungcrantz, *Microstructure and mechanical behavior of arc-evaporated Cr-N coatings*. Surface and Coatings Technology, 1999. **114**(1): p. 39-51.
171. A. Kondo, T. Oogami, K. Sato, and Y. Tanaka, *Structure and properties of cathodic arc ion plated CrN coatings for copper machining cutting tools*. Surface and Coatings Technology, 2004. **177-178**: p. 238-244.
172. SJ Bull, DS Rickerby, A Matthews, A Leyland, AR Pace, and J Valli, *The use of scratch adhesion testing for the determination of interfacial adhesion: the importance of frictional drag*. Surface and Coatings technology, 1988. **36**(1-2): p. 503-517.
173. PJ Burnett and DS Rickerby, *The relationship between hardness and scratch adhesion*. Thin solid films, 1987. **154**(1-2): p. 403-416.
174. SJ Bull, *Failure modes in scratch adhesion testing*. Surface and Coatings Technology, 1991. **50**(1): p. 25-32.
175. Shize Jin, Sofiene Amira, and Edward Ghali, *Electrochemical impedance spectroscopy evaluation of the corrosion behavior of die cast and thixocast AXJ530 magnesium alloy in chloride solution*. Advanced Engineering Materials, 2007. **9**(1 - 2): p. 75-83.
176. J Ross Macdonald and E Barsoukov, *Impedance spectroscopy: theory, experiment, and applications*. History, 2005. **1**(8).
177. BT Mark and E Orazem, *Electrochemical impedance spectroscopy*. John Willey & Sons, Hoboken, New Jersey, 2008.
178. F-H Cao, V-H Len, Z Zhang, and J-Q Zhang, *Corrosion behavior of magnesium and its alloy in NaCl solution*. Russian journal of electrochemistry, 2007. **43**(7): p. 837-843.
179. AD King, N Birbilis, and JR Scully, *Accurate electrochemical measurement of magnesium corrosion rates; a combined impedance, mass-loss and hydrogen collection study*. Electrochimica Acta, 2014. **121**: p. 394-406.
180. Guangling Song, Andrej Atrens, D St John, Xianliang Wu, and Jason Nairn, *The anodic dissolution of magnesium in chloride and sulphate solutions*. Corrosion Science, 1997. **39**(10-11): p. 1981-2004.
181. Geneviève Baril, Gonzalo Galicia, Claude Deslouis, Nadine Pébère, Bernard Tribollet, and Vincent Vivier, *An impedance investigation of the mechanism of pure magnesium corrosion in sodium sulfate solutions*. Journal of The Electrochemical Society, 2007. **154**(2): p. C108-C113.
182. Digby D Macdonald, *Reflections on the history of electrochemical impedance spectroscopy*. Electrochimica Acta, 2006. **51**(8): p. 1376-1388.
183. FD Wall, MA Martinez, NA Missert, RG Copeland, and AC Kilgo, *Characterizing corrosion behavior under atmospheric conditions using electrochemical techniques*. Corrosion Science, 2005. **47**(1): p. 17-32.

-
184. Raman Vedarajan and Toshiyasu Nishimura, *Corrosion analysis and monitoring of the environmental factors for the deterioration of chromium-bearing reinforcing steel in mortar*. Journal of Solid State Electrochemistry, 2010. **14**(8): p. 1457-1464.
 185. KM Yin and LI Lu, *Parametric study on the electrochemical impedance spectroscopy of organic-coated steels in hydrochloric acid solutions*. Journal of Coatings Technology, 2003. **75**(941): p. 65-72.
 186. Milton Stern and Al L Geary, *Electrochemical polarization I. A theoretical analysis of the shape of polarization curves*. Journal of the electrochemical society, 1957. **104**(1): p. 56-63.
 187. E McCafferty, *Validation of corrosion rates measured by the Tafel extrapolation method*. Corrosion Science, 2005. **47**(12): p. 3202-3215.
 188. P Scherrer, *Bestimmung der Grosse und der inneren Struktur von Kolloidteilchen mittels Rontgenstrahlen (1918) in: X-ray Diffraction Methods in Polymer Science, Ed. LE Alexander*. 1969, Wiley-Interscience, New York.
 189. JM Walls, DD Hall, and DE Sykes, *Composition–Depth profiling and interface analysis of surface coatings using ball cratering and the scanning auger microprobe*. Surface and Interface Analysis, 1979. **1**(6): p. 204-210.
 190. JF Archard. *Elastic deformation and the laws of friction*. in *Proceedings of the Royal Society of London A: Mathematical, Physical and Engineering Sciences*. 1957. : The Royal Society.
 191. J Musil, *Hard and superhard nanocomposite coatings*. Surface and coatings technology, 2000. **125**(1): p. 322-330.
 192. MM Stack and MT Mathew, *Mapping the micro-abrasion resistance of WC/Co based coatings in aqueous conditions*. Surface and Coatings Technology, 2004. **183**(2): p. 337-346.